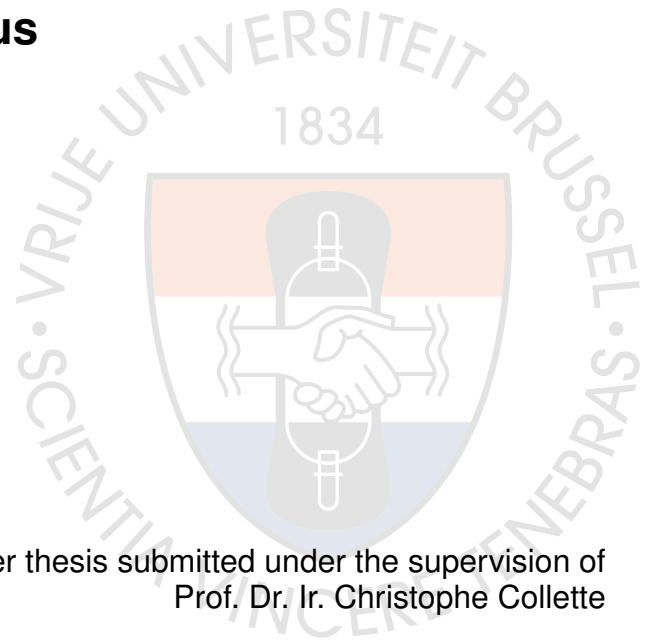


# Active Damping of Violin Modes in Quadruple Suspensions of Gravitational Wave Detectors

Master Thesis

**Alexandre La Grappe Dominicus**



Master thesis submitted under the supervision of  
Prof. Dr. Ir. Christophe Collette

the co-supervision of  
Prof. Dr. Ir. Arnaud Deraemaeker

in order to be awarded the Degree of

Master of Science in Electromechanical Engineering  
major in Mechatronics Construction

Academic year  
2018 – 2019

The author gives permission to make this master dissertation available for consultation and to copy parts of this master dissertation for personal use. In all cases of other use, the copyright terms have to be respected, in particular with regard to the obligation to state explicitly the source when quoting results from this master dissertation.

03/06/2019

---

**Title: Active damping of violin modes in quadruple suspensions of gravitational wave detectors**

Author: Alexandre La Grappe Dominicus

Master of Science in Electromechanical Engineering – major in Mechatronics Construction

Academic year: 2018 – 2019

---

## Abstract

Gravitational waves are distortions of space-time that have been predicted to exist by Einstein's General Theory of Relativity. On September 14, 2015, the era of gravitational-wave astronomy has been opened by the observation of a transient gravitational wave signal determined to be the coalescence of two black holes. To reach the required sensitivity, the Laser Interferometer Gravitational-Wave Observatory (LIGO) is equipped with a quadruple pendulum, which is a chain of four suspended masses used to provide seismic isolation.

The research discussed in this work is on the active damping of transverse eigenmode vibrations of the suspension fibres (also known as *Violin Modes*), which are standing wave modes that can be excited by seismic noise, thermal noise, sudden relaxations of mechanical stresses, etc. The vibrational energy from these high-Q modes is transferred to the suspended test masses along the line of the interferometric beam-axis, at frequencies lying within the gravitational wave detection bandwidth. The methods explored here are based on collocated control strategies using piezoelectric force actuation and sensing. The first approach consists of an axial parametric control that dynamically changes the tension in the fibre in a way that destructively interferes with the fibre's transverse vibrations. The second approach is based on a transverse boundary force control for which classical active damping schemes designed for linear systems like Integral Force Feedback (IFF) can be used. The suspension fibre dynamics are derived as well as the interactions with different sensor and actuator configurations and technologies using distinct formalisms. The proposed strategies are simulated numerically based on the latter mathematical representations and the damping performances are compared to the analytical predictions. The theoretical outcomes are then validated experimentally on a real plant and the results are discussed including the limitations of the recommended strategies.

**Keywords:** violin modes, active damping, collocated control, piezoelectric transducer, parametric control

---

## **Titre: Amortissement actif des modes violon dans les suspensions quadruples de détecteurs d'ondes gravitationnelles**

Auteur: Alexandre La Grappe Dominicus

Master Ingénieur civil électromécanicien – finalité Mécatronique

Année Académique: 2018 – 2019

---

### **Résumé**

Les ondes gravitationnelles sont des distorsions de l'espace-temps prédites par la théorie de la relativité générale d'Einstein. Le 14 septembre 2015, l'ère de l'astronomie des ondes gravitationnelles a été lancée par l'observation d'un signal d'onde gravitationnel transitoire provenant de la coalescence de deux trous noirs. Pour atteindre la sensibilité requise à la mesure d'ondes gravitationnelles, le Laser Interferometer Gravitational-Wave Observatory (LIGO) est équipé d'une chaîne de quatre masses suspendues servant à l'isolation sismique.

Les travaux abordés dans ce mémoire de fin d'études portent sur l'amortissement actif des vibrations transversales associées aux modes propres des fibres de suspension (également appelés *Violin Modes*). Ce sont des modes d'ondes stationnaires pouvant être excités par du bruit sismique, du bruit thermique, des relaxations mécaniques soudaines, etc. L'énergie vibrationnelle provenant de ces modes à facteur de qualité élevé est transférée aux miroirs suspendus, le long de l'axe du faisceau interférométrique, à des fréquences comprises dans la largeur de bande de détection des ondes gravitationnelles. Les méthodes explorées ici sont basées sur des stratégies de contrôle co-localisées utilisant un actionnement et une mesure de force piézoélectrique. La première approche consiste à effectuer un contrôle paramétrique axial qui modifie de façon dynamique la tension dans la fibre pour interférer de manière destructive avec les vibrations transversales de celle-ci. La seconde approche est basée sur un contrôle de force transversal pour lequel des techniques d'amortissement actif classiques conçues pour des systèmes linéaires tels que le Integral Force Feedback (IFF) peuvent être utilisées. Les équations décrivant la dynamique des fibres de suspension sont établies ainsi que les interactions avec différentes configurations de capteurs et d'actionneurs en utilisant des formalismes distincts. Les stratégies proposées sont simulées numériquement sur base de ces dernières représentations mathématiques et les performances d'amortissement sont comparées aux prévisions analytiques. Les résultats théoriques sont ensuite validés expérimentalement sur un système réel et les résultats sont discutés ainsi que les limites des stratégies proposées.

**Mots clés : violin modes, amortissement actif, contrôle co-localisé, transducteur piézoélectrique, contrôle paramétrique**

---

**Titel: Actieve demping van violin modes in viervoudige slingers in gravitatiegolf-detectoren**

Author: Alexandre La Grappe Dominicus

Master in de ingenieurswetenschappen werktuigkunde-elektrotechniek – Werktuigbouwkunde

Academisch jaar: 2018 – 2019

---

## Samenvatting

Gravitatiegolven of zwaartekrachtgolven zijn fluctuaties in de kromming van de ruimtetijd voorspeld door Einstein's Algemene Relativiteitstheorie. Op 14 september 2015 is het tijdperk van de zwaartekrachtgolf-astronomie gestart door de waarneming van een zwaartekrachtgolfsignaal dat afkomstig is van een coalescentie van twee zwarte gaten. Om de vereiste gevoeligheid te bereiken is de Laser Interferometer Gravitational-Wave Observatory (LIGO) uitgerust met een viervoudige slinger, waarin vier hangende massa's gebruikt worden om seismische isolatie te bieden.

Het onderzoek dat in dit werk wordt besproken betreft de actieve demping van transversale eigenmode-trillingen van de ophangingsvezels (ook bekend als *Violin Modes*), staande golf modi die gedreven kunnen worden door seismische ruis, thermische ruis, plotselinge relaxaties van mechanische spanningen, etc. De trillingsenergie van deze hoge Q-modi wordt overgebracht naar de opgehangen testmassa's in de richting van de interferometrische laser-as, bij frequenties die liggen binnen de bandbreedte die dient voor de zwaartekrachtgolfdetectie. De voorgestelde methoden zijn gebaseerd op colocated control met behulp van piëzo-elektrische krachtactuator en meting. De eerste methode bestaat uit een axiale parametrische controle die de spanning in de vezel dynamisch verandert zodanig dat die destructief interfereert met de transversale trillingen van de vezel. De tweede methode is gebaseerd op een transversale krachtregeling waarvoor klassieke actieve dempingsschema's ontworpen voor lineaire systemen zoals Integral Force Feedback (IFF) kunnen worden gebruikt. De dynamica van de ophangingsvezels is afgeleid, evenals de interacties met verschillende sensor- en actuatorconfiguraties en technologieën met behulp van verschillende formalismen. De voorgestelde strategieën worden numeriek gesimuleerd op basis van de wiskundige afleidingen en de demping wordt vergeleken met de analytische voorspellingen. De theoretische resultaten worden vervolgens experimenteel gevalideerd op een reëel systeem en de uitslagen worden besproken samen met de beperkingen van de aanbevolen strategieën.

**Kernwoorden:** violin modes, actieve demping, colocated control, piëzo-elektrische transducer, parametrische controle

# Acknowledgements

This work marks the beginning of my life as a mechanical engineering graduate student. I would like to thank all those who supported me during my whole academic experience at the VUB and the ULB, but also those who made this specific effort possible.

First, I must thank Professor Christophe Collette for allowing me to realize my master thesis in a field that is fascinating to me, for having dedicated his time and having constantly advised me in the completion of this work. I also thank Arnaud Deraemaeker, the co-supervisor on this project, for his support on theoretical considerations and for his careful reading and corrections. I warmly thank my advisor Binlei Ding and his colleague Guoying Zhao for their listening, their positive support and their instructive reflections. I also thank the entire team of the Precision Mechatronics Laboratory, who helped me for the realization of the required measurements.

My family, especially my parents, my step-parents, my brother and my grand-mother deserve recognition and acknowledgements that reflect the important role they played throughout my studies. I would like to thank all of them for their support and trust, their wise advice and their relevant critics. I also extend special thanks to André Nauts, the passionate physicist who succeeded in transmitting his adoration for science to me. Finally, I thank Camille for her love and unmeasurable support during the last five years.

# Table of Contents

Abstract . . . . .	I
Résumé . . . . .	II
Samenvatting . . . . .	III
<b>Table of Contents</b>	<b>V</b>
<b>List of Figures</b>	<b>VII</b>
<b>List of Abbreviations</b>	<b>XI</b>
<b>List of Symbols</b>	<b>XII</b>

<b>Active Damping of Violin Modes in Quadruple Suspensions of Gravitational Wave Detectors</b>	<b>1</b>
<b>1 Violin Modes in Gravitational Wave Detectors</b>	<b>1</b>
1.1 Introduction . . . . .	1
1.2 Laser Interferometers . . . . .	2
1.3 Quadruple suspension . . . . .	3
1.4 Thermal Noise and Violin Modes . . . . .	5
1.5 Motivation and goals . . . . .	8
1.6 Project outline . . . . .	8
<b>2 Dynamic modelling of a single fibre</b>	<b>9</b>
2.1 Introduction . . . . .	9
2.2 Linear models . . . . .	9
2.2.1 Analytical model . . . . .	9
2.2.2 Finite Elements State Space Representation . . . . .	12
2.3 Nonlinear model . . . . .	18
2.3.1 Single mode spring model . . . . .	18
2.3.2 Continuous fibre model . . . . .	19
2.4 Violin Mode excitation mechanisms . . . . .	21
2.4.1 Guitar plectrum . . . . .	21
2.4.2 Thermal noise . . . . .	22
2.4.3 Electromagnetic excitation . . . . .	23
2.4.4 Electrostatic excitation . . . . .	24
<b>3 Active damping of violin modes</b>	<b>25</b>
3.1 Introduction . . . . .	25
3.2 Sensing . . . . .	25
3.2.1 Vertical force sensor at the boundary . . . . .	25
3.2.2 Horizontal force sensor at the boundary . . . . .	27
3.2.3 Piezoelectric sensors . . . . .	27
3.2.4 Other sensors . . . . .	28
3.3 Actuation . . . . .	29
3.3.1 Vertical Force Actuator: Parametric Excitation . . . . .	29
3.3.2 Stability analysis of a parametrically excited fibre . . . . .	30

3.3.3	Horizontal Force Actuator . . . . .	33
3.3.4	Piezoelectric actuators . . . . .	33
3.4	Vibration Control Strategies . . . . .	34
3.4.1	Vertical collocated force actuator and sensor . . . . .	34
3.4.2	Horizontal collocated force actuator and sensor . . . . .	41
3.5	Conclusion . . . . .	44
<b>4</b>	<b>Experiments</b>	<b>45</b>
4.1	Introduction . . . . .	45
4.2	Experimental Setup . . . . .	45
4.2.1	Suspension arrangement . . . . .	45
4.2.2	Collocated Piezoelectric transducer . . . . .	46
4.2.3	Piezoelectric Transducer Control and Data Acquisition . . . . .	47
4.2.4	Violin Mode Excitation . . . . .	47
4.3	Test results . . . . .	48
4.3.1	Vertical collocated piezoelectric mount . . . . .	49
4.3.2	Horizontal collocated piezoelectric mount . . . . .	52
4.4	Discussion . . . . .	53
4.4.1	Measurement of violin modes . . . . .	53
4.4.2	Excitation of violin modes . . . . .	53
4.4.3	Active damping of violin modes . . . . .	54
<b>5</b>	<b>Main suspension chain vibration modes</b>	<b>55</b>
5.1	Introduction . . . . .	55
5.2	Pendulum, pitch and yaw motion . . . . .	55
5.2.1	Single suspended mass . . . . .	55
<b>6</b>	<b>Conclusions and Future Work</b>	<b>58</b>
	<b>Bibliography</b>	<b>64</b>
	<b>Appendices</b>	<b>65</b>
<b>A</b>	<b>Mathematical Developments</b>	<b>65</b>
A.1	Nonlinear single mode spring model . . . . .	65
A.2	Energy production . . . . .	66
A.3	Yaw motion geometric constant . . . . .	67
A.4	Complete suspension model with vibrating fibres . . . . .	68
A.5	Potential Multi-DOF Motion Damping . . . . .	70
<b>B</b>	<b>Additional Figures</b>	<b>73</b>
B.1	Simulink models . . . . .	73
B.2	Simulations . . . . .	79
B.3	Measurements . . . . .	80
<b>C</b>	<b>Matlab scripts</b>	<b>82</b>
C.1	Fibre parameters Matlab code . . . . .	82
C.2	FE simulations in the time domain . . . . .	85
C.3	Integral Force Feedback design . . . . .	89
C.4	Model including transmissibility . . . . .	91

# List of Figures

1.1	The gravitational-wave event GW150914 observed by the LIGO Hanford (H1, left column panels) and Livingston (L1, right column panels) detectors. The second row shows the projection of the observations in the 35-350 Hz band compared with a reconstructed model using binary black hole template waveforms (dark gray) and another one using a linear combination of sine-Gaussian wavelets (light gray). The third row shows the residuals after subtracting the filtered numerical relativity waveform from the filtered detector time series. The bottom row is a time-frequency representation of the strain data, showing the signal frequency increasing over time [1] . . . . .	2
1.2	A diagram of an Advanced LIGO (aLIGO) detector (not to scale)[1]. . . . .	3
1.3	A photograph of the LIGO Hanford Observatory in Washington State[2]. . . . .	4
1.4	Schematic diagram of quadruple pendulum suspension system for Advanced LIGO. The diagram above shows a face view of the main chain on the left, and on the right a side view with main and reaction chains is visible[3]. . . . .	4
1.5	The displacement sensitivity of the Advanced LIGO detector in Hanford; the Livingston detector has a similar sensitivity[4]. . . . .	5
1.6	The fundamental violin mode and the pendulum mode of a single suspension fibre pendulum, also showing the anelastic bending of the fibres near the attachment points. (figure from [5]) . . . . .	6
1.7	The H1 detector noise spectrum. The black curve is the measured strain noise (same spectrum as the red line in Figure 1.5). The labeled spectral peaks are identified as follows: c, calibration line; p, power line harmonic; s, suspension wire vibrational mode; m, mirror (test mass) vibrational mode. (figure from [6]) . . . . .	7
1.8	The standing wave modes of a taut fibre with the corresponding wavelengths (figure from [7]). . . . .	7
2.1	The stretched continuous fibre with fixed ends conditions (left) and a section $ds$ of a fibre in a deformed state (right). . . . .	10
2.2	The first mode shape with a flexure correction. . . . .	11
2.3	The spatial discretization of a fibre into $N$ lumped masses for a Finite Elements (FE) representation of its dynamics. . . . .	12
2.4	Upper fixed-end boundary condition of the fibre with a penalizing stiffness $k_p$ and a tip mass $M_{tm}$ . . . . .	14
2.5	(a) The power spectral density of the position of the middle of the fibre; (b) the shape of the fibre at consecutive time steps ( $t_i = 2.5 + i \cdot \Delta T$ sec). The input force has a white Gaussian spectral content, which is band-limited between $50Hz$ and $500Hz$ . The simulation time is 10s and the sampling frequency is $f_s = \frac{1}{\Delta T} = 2kHz$ . . . . .	15

2.6	The shape of the fibre at consecutive time steps ( $t_i = 2.5 + i \cdot \Delta T$ sec) for a sinusoidal excitation at the 2 <sup>nd</sup> Violin Mode (VM) frequency $f_2 = 155.6Hz$ . . . . .	16
2.7	Open Loop transfer function between a horizontal force actuator and sensor which are collocated at the fibre suspension point. The pendulum mode (PM) and the violin modes (VM) are clearly visible and their frequencies correspond to the expected ones. . . . .	17
2.8	The bode plot of the transfer function between the suspension motion and the test mass motion for a single degree of freedom pendulum and a multimode FE model, taking into account the Violin Modes (VMs). . . . .	17
2.9	The single mode model of a nonlinear fibre with one lumped mass and two identical springs. . . . .	19
2.10	The plucked fibre initial shape. . . . .	21
2.11	The ferromagnetic wire excited by an electromagnet. . . . .	23
3.1	The perfect vertical force sensor to measure the dynamic tension. . . . .	26
3.2	Time plot of the fibre's total tension $T(t) = T_s + T_d(t)$ . . . . .	26
3.3	A schematic representation of a discrete piezoelectric transducer (Figure from [8]). . . . .	27
3.4	The schematic of the VMs shadow sensor from [9]. The mirror-coated beam-splitting prism reflects the near infrared beam on the two reverse-biased photodiodes PDa and PDb. The beam splitting allows a factor $\sqrt{2}$ improvement in signal-to-noise ratio. . . . .	28
3.5	The optical sensor based on the optical-beam deflection technique [10]. . . . .	28
3.6	The perfect force actuator exerting a force along the axial direction of the fibre. . . . .	29
3.7	The different regions in the parameter space for the classification of steady-state solutions of the damped and parametrically excited Duffing equation. . . . .	31
3.8	The effect of viscous damping on the stability of the Mathieu equation around $\omega_u = 2\omega_n$ and $\omega_u = \omega_n$ (remembering Equation (3.11)). The shadowed regions define unstable solutions with unbounded amplitude growth. (Figure from [11]) . . . . .	32
3.9	The perfect horizontal force actuator $F_u$ . . . . .	33
3.10	The perfectly collocated vertical force actuator-sensor pair. . . . .	34
3.11	The quality factor of the first VM as a function of the actuation amplitude $A_u$ . . . . .	36
3.12	The first mode vibration amplitude envelope for a sinusoidal magnetic excitation with a frequency $f_1$ and a vertical sinusoidal force excitation at $2f_1$ activated after 10 sec. The phase delay of the vertical excitation with respect to the string's first mode motion is shifted over time, showing an optimal phase difference around $\frac{\pi}{2}$ . . . . .	40
3.13	A comparison between simple IFF ( $A_u = 10^6$ ) and derivative feedback with amplitude estimation ( $A_u = -0.5$ ). . . . .	40
3.14	The perfectly collocated horizontal force actuator-sensor pair. . . . .	41
3.15	The root-locus of the Integral Force Feedback (IFF), showing the migration of the poles towards the zeros for an increasing feedback gain. The units for both axes are in $\frac{rad}{s}$ . . . . .	42

3.16	Open Loop vs. Closed Loop transfer function between force actuator and sensor for a feedback gain of $10^6$ and an integrator $\frac{1}{s}$ . The pendulum mode (PM) and the VMs are all present in these transfer functions, clearly showing the corresponding poles and zeros. . . . .	43
3.17	The transmissibility transfer function from ground motion (at the suspension point) to test mass motion with and without IFF control. . .	43
4.1	A schematic drawing of the suspended mass and the collocated piezoelectric force sensor-actuator pair in the vertical configuration (left) and the horizontal configuration (right). . . . .	45
4.2	The suspended mass of 1.456kg coming from a machining lathe spindle. It is attached to the fibre with a screw clamp. . . . .	46
4.3	The vertically mounted <i>APA 100M</i> piezoelectric transducer from Cedrat Technologies. . . . .	46
4.4	The horizontally mounted <i>APA 100M</i> piezoelectric transducer with a clamping allowing no bending forces. . . . .	47
4.5	The magnetic coil, screwed on a metallic structure with a sliding slot, allowing to choose the position of the excitation. . . . .	48
4.6	The vertical piezoelectric sensor signal Amplitude Spectral Density (ASD) for a white noise magnetic excitation. The first peak corresponds to the vertical eigenmode of the string at the frequency $f_v = 27.5\text{Hz}$ . The following peaks are the VM harmonics, for which the fundamental frequency is $f_1 = 37.5\text{Hz}$ . . . . .	49
4.7	The vertical piezoelectric sensor signal filtered around $f_1 = 37.5\text{Hz}$ (to observe the string amplitude through the linear observability) for a sinusoidal magnetic excitation with a frequency $f_1$ and a vertical sinusoidal excitation at $2f_1$ by applying a voltage of $60V_{pp}$ . The phase delay of the piezo excitation with respect to the string's first mode motion is shifted over time, showing an optimal phase difference around $\frac{\pi}{2}$ . The vibration amplitudes shown on the pictures are approximately $\delta_a = 5.5\text{mm}$ , $\delta_d = 2.5$ , $\delta_c = 4\text{mm}$ . . . . .	50
4.8	Comparison between IFF and derivative control when activating the control approximately 1.5s after plucking the string. . . . .	51
4.9	The comparison between vertical piezoelectric sensor signal ASDs obtained with and without IFF control. . . . .	51
4.10	The estimated open loop transfer function between the actuator and the sensor and the associated coherence function. . . . .	52
5.1	The different degrees of freedom for a single suspension loop with different perspectives: (left) side view; (middle) front view; (right) top view. . . . .	55
5.2	The single suspended mass pitch and pendulum modes, with a moving suspension point. . . . .	56
5.3	The single suspended suspension loop yaw mode, with a rotating suspension base. . . . .	57

A.1	The restoring force - deflection characteristic of the spring system in Figure 2.9 for $k = 10\frac{kN}{m}$ $L = 0.1m$ and $L_0 = 0.08m$ given by Equation (A.2) (blue line) and the approximate expression defined by Equation (A.4) (red line). . . . .	66
A.2	The schematic diagram linking the forces on the test mass with geometric constants. . . . .	67
A.3	The different degrees of freedom for a two-stage isolation system and the definition of the attachment points of the fibres. . . . .	68
A.4	The directions of the forces exerted by the VMs at the attachment points for even and odd mode numbers. . . . .	69
A.5	Schematic diagram of a modal control loop from [2]. The state $\vec{x}$ is transformed into modal signals $\vec{q}$ and passed through the respective control filters. The resulting modal forces $\vec{P}_m$ are then transformed into real forces $\vec{P}$ that are applied to the real system. . . . .	71
B.1	The simulink fibre subsystem, taking the actuator force as input and both the dynamic tension and the modal amplitude as outputs. . . . .	73
B.2	The custom made amplitude estimator block diagram. . . . .	73
B.3	The tension amplitude estimator input (blue) and output (red). . . . .	73
B.4	The Simulink derivative control block diagram with amplitude estimation. . . . .	74
B.5	The Simulink IFF control block diagram. . . . .	74
B.6	Simulink model used with dSpace for electromagnet excitation and IFF control. . . . .	74
B.7	Simulink model used with dSpace for electromagnet excitation and derivative feedback control. . . . .	75
B.8	The Simulink model of the quadruple suspension, taking into account the dynamic tension and the forces exerted at the fibre boundaries due to VM vibrations. This model also includes the decentralized parametric control of VMs. . . . .	76
B.9	The Simulink model of the lower mass in the quadruple suspension shown in Figure B.8. . . . .	77
B.10	The Simulink model of the upper mass in the quadruple suspension shown in Figure B.8. . . . .	78
B.11	The upper mass (UM) and lower mass (LM) pendulum, pitch and yaw evolution with and without decentralized parametric control on each suspension fibre. . . . .	79
B.12	The recorded string position signal and vertical parametric control signal for a relative phase difference of (a) $\phi_u = \frac{\pi}{2}$ for a damping effect and (b) $\phi_u = -\frac{\pi}{2}$ for an amplifying effect. . . . .	80
B.13	The estimated transfer function between the electromagnet signal and the force sensor with and without IFF control. . . . .	81

# List of Abbreviations

aLIGO	Advanced LIGO
ASD	Amplitude Spectral Density
BBH	binary black holes
CL	Closed Loop
DOFs	Degrees Of Freedom
EOM	equations of motion
FE	Finite Elements
FEMM	Finite Element Method Magnetics
GW	gravitational waves
IFF	Integral Force Feedback
LIGO	Laser Interferometer Gravitational-Wave Observatory
LISA	Laser Interferometer Space Antenna
LQR	Linear-Quadratic Regulator
LSC	LIGO Scientific Collaboration
MIMO	Multiple-Input Multiple-Output
OL	Open Loop
OSEM	Optical Sensor Electro-Magnet
PML	Precision Mechatronics Laboratory
PSD	Power Spectral Density
PSD	Position Sensitive Detector
SISO	Single-Input Single-Output
U.S.	United States
ULB	Universite Libre de Bruxelles
VM	Violin Mode
VMs	Violin Modes
VUB	Vrije Universiteit Brussel

# List of Symbols

$\tilde{q}_n$	Dimensionless modal amplitude in the modified Mathieu equation	-
$\delta$	Dimensionless coefficient of the linear term in the modified Mathieu equation	-
$\epsilon$	Dimensionless coefficient of the parametric excitation term in the modified Mathieu equation	-
$\mu$	Dimensionless coefficient of the damping term in the modified Mathieu equation	-
$\tau$	Dimensionless time in the modified Mathieu equation	-
$A_u$	Actuator force amplitude	N
$A$	Cross section area of the fibre	m <sup>2</sup>
$E_{p,\xi_n}$	Work done by the viscous damping on the fibre during one oscillation period	J
$E_{p,u}$	Work done by the actuator on the fibre during one oscillation period	J
$E$	Young Modulus of the fibre	N / m <sup>2</sup>
$F_e$	Electrostatic force	N
$F_m$	Magnetic force	N
$F_u$	Actuator force	N
$F_{e,i}$	External force on degree of freedom i	N
$I$	Current injected in the electromagnet	A
$K_m$	Diagonal modal stiffness matrix	N / m
$K_n$	Kinetic energy associated to the transverse vibration mode $n$	J
$K$	Stiffness matrix	N / m
$L_0$	Initial length of the fibre in unstressed conditions	m
$L_f$	Inductance of the electromagnet	H
$L$	Static length of the fibre in suspension conditions	m
$M_m$	Diagonal modal mass matrix	kg
$M_{tm}$	Test mass	kg
$M$	Mass matrix	kg
$N$	Number of spatial discretisation points in the Finite Elements Model	-
$R$	Resistance of the electromagnet	$\Omega$
$T_d$	Dynamic tension of the fibre	N
$T_f$	Temperature of the fibre	K
$T_m$	The highpass-filtered tension of the fibre	N
$T_s$	Static tension of the fibre	N
$T_{d,n}$	Dynamic tension in the fibre caused by mode number $n$	N
$T$	Total tension of the fibre	N
$U$	Electrical tension over the electromagnet's solenoid	V
$\Delta$	Elastic distance	m
$\Phi$	Modal basis formed by the $N$ eigenvectors $\phi_n$	-
$\Theta_i$	Angle between the z-axis and the section formed by the two lumped masses $i$ and $i - 1$	rad

$\Theta$	Pitch degree of freedom	rad
$\vec{F}_m$	Vector of modal forces	N
$\alpha$	Dimensionless coefficient of the nonlinear term in the modified Mathieu equation	-
$\beta_d$	Linear viscous damping	N s /m <sup>2</sup>
$\epsilon_d$	Dynamic axial strain in the fibre	-
$\omega_\Theta$	Eigenfrequency of the pitch mode	rad /s
$\omega_\phi$	Eigenfrequency of the yaw mode	rad /s
$\omega_n$	Eigenfrequency of violin mode number $n$	rad /s
$\omega_u$	Frequency of the actuator signal	rad /s
$\omega_v$	Eigenfrequency of the axial vibration mode of the fibre	rad /s
$\omega_x$	Eigenfrequency of the pendulum mode	rad /s
$\phi_e$	Suspension yaw motion	m
$\phi_f$	Magnetic flux through the electromagnet	Wb
$\phi_n$	Rayleigh-Ritz mode shape of violin mode number $n$	-
$\phi_u$	Relative phase difference between the actuation signal and the considered modal fibre vibration	rad
$\phi$	Yaw degree of freedom	rad
$\pi$	Geometrical value $\approx 3.1416$	rad
$\rho$	Linear density of the fibre	kg/m <sup>2</sup>
$\xi_n$	Modal damping factor	-
$\xi_{a,n}$	Equivalent added modal damping factor	-
$\xi_{n,tot}$	Total modal damping factor	-
$d_g$	Separation gap between the electrode plates	C
$d$	Plucking distance along the fibre axial direction	m
$f_s$	Sampling frequency	1 /s
$g$	Gravitational acceleration on Earth $\approx 9.8107$	m/s <sup>2</sup>
$h$	Plucking deflection normal to the fibre axial direction	m
$k_B$	Boltzmann constant $\approx 1.38064852 \cdot 10^{-23}$	m <sup>2</sup> kg/(Ks <sup>2</sup> )
$k_p$	Stiffness of the APA100M piezoelectric transducer $\approx 1.857 \cdot 10^6$	N /m
$m$	Lumped mass	kg
$n$	Mode number	-
$q_e$	Electrical charge	C
$q_n$	Modal amplitude of violin mode number $n$	m
$t$	Time	s
$v$	Wave propagation speed in the fibre in its axial direction	m/s
$x_e$	Suspension displacement along the interferometric axis	m
$x$	Pendulum degree of freedom	m
$y_i$	Absolute transverse displacement of the $i$ 'th lumped mass	m
$y$	Absolute transverse displacement along the continuous fibre	m

## Chapter 1

# Violin Modes in Gravitational Wave Detectors

This introductory chapter provides a brief description of gravitational waves (GW) and how the LIGO succeeded in capturing the first direct observations of GW. It will then briefly describe the objective of this master thesis and why it is an important research question.

### 1.1 Introduction

The recent measurements of GW have significantly raised excitement and motivation amongst scientists about the quest for GW. The ability to identify gravitational radiation patterns enables the observation and analysis of astronomical coalescing binaries like merging black holes or neutron stars, supernovae and pulsars, launching a new era of gravitational-wave astronomy. According to some theories of quantum gravitational processes in the early Universe, it would also allow to collect valuable information about the early Universe just after the occurrence of the Big Bang and according to other theories, like the loop quantum cosmology, information about the Universe before the Big Bounce [12]. In 1916, Albert Einstein predicted the existence of GW using the General Theory of Relativity. These waves, being a solution to the linearized weak-field equations, can be portrayed as a space-time curvature propagating at the speed of light.[1] They are generated by time variations of the mass quadrupole moment of the source and can be represented by Equation (1.1).

$$\left(\nabla^2 - \frac{1}{c^2} \frac{\partial^2}{\partial t^2}\right) h_{\mu\nu} = 0 \quad (1.1)$$

where the constant  $c$  is the speed of light and the tensor  $h_{\mu\nu}$  represents the metric perturbation away from the so-called *flat* space-time [13]. The astronomical sources of GW strong enough to be detected by an observatory such as aLIGO include supernovae, coalescing compact binaries, pulsars, and a stochastic background of GW. While the existence of GW has been demonstrated earlier through the observations of the energy losses of the binary pulsar system PSR B1913p16 [14], the first direct observation of GW took place on September 14, 2015 at the LIGO Hanford and Livingston observatories in the United States (U.S.) and is referred as GW150914 (see Figure 1.1). The gravitational radiation transients seemed to match relativistic models of compact binary waveforms corresponding to binary black holes (BBH). This observation was made possible principally thanks to the significant increase in sensitivity brought by the upgrade of the LIGO detectors, known as aLIGO. At the time of GW150914, the LIGO detectors were the only ones in active observational mode being sufficiently sensitive. However, other GW detectors were completed at the time, including Virgo in Italy, TAMA 300 in Japan, and GEO 600 in Germany which evolved into a global network of significantly more sensitive and advanced detectors.[1, 15] Despite the very high performances reached in terms of sensitivity, ground-based detectors

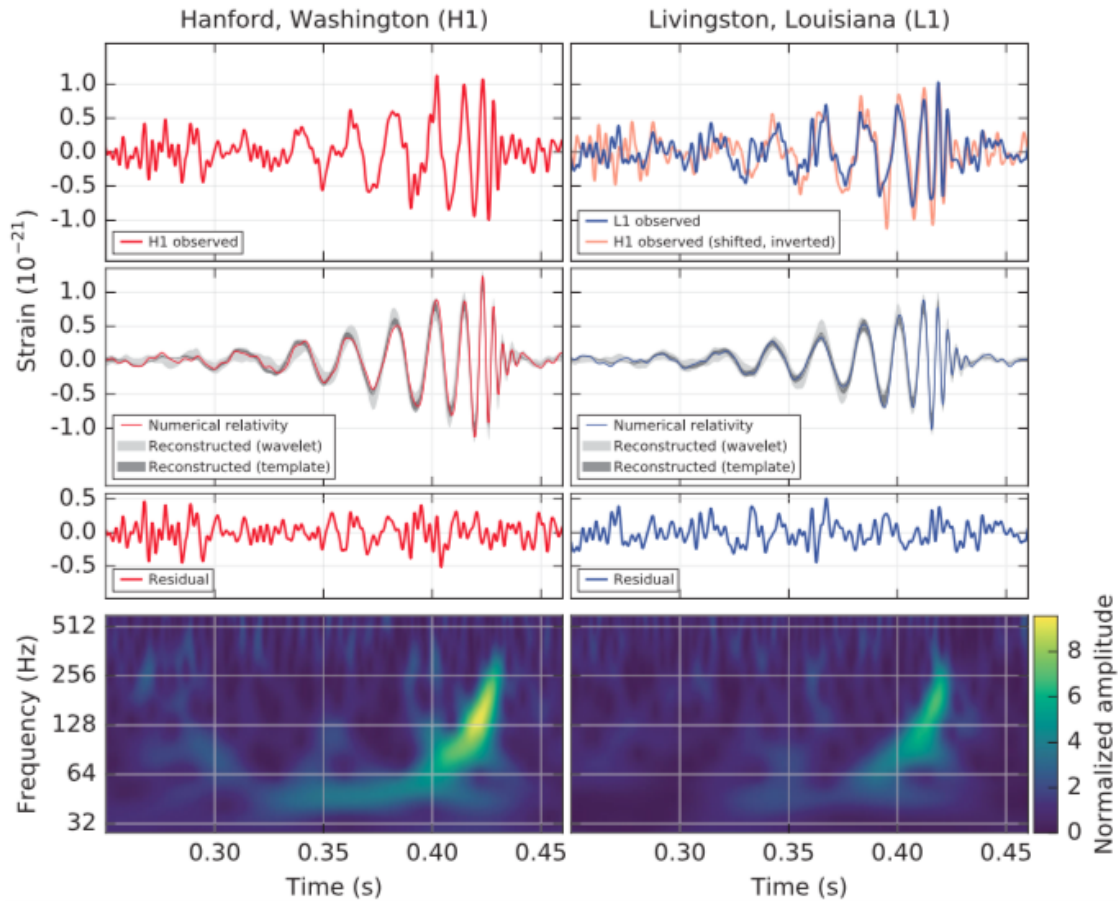


Figure 1.1 – The gravitational-wave event GW150914 observed by the LIGO Hanford (H1, left column panels) and Livingston (L1, right column panels) detectors. The second row shows the projection of the observations in the 35–350 Hz band compared with a reconstructed model using binary black hole template waveforms (dark gray) and another one using a linear combination of sine-Gaussian wavelets (light gray). The third row shows the residuals after subtracting the filtered numerical relativity waveform from the filtered detector time series. The bottom row is a time-frequency representation of the strain data, showing the signal frequency increasing over time [1]

can only observe astronomical sources of GW with short lifetimes which are characterised by short wavelengths ( $< 1$  sec). Some sources with longer characteristic time scales or very low amplitude could only be observed in space using satellites, free of the seismic disturbances present on earth. The planned Laser Interferometer Space Antenna (LISA) mission, with its baselines defined by satellites five million kilometers apart, should reach a sensitivity that allows to study the formation of galaxies and the formation of interactions of massive black holes through the observable universe [16, 17].

## 1.2 Laser Interferometers

The interferometers used to detect gravitational waves are a modified version of the classical Michelson type that has been used to look for the ether drift. The biggest differences are the size of the detector (the two interferometric arm lengths are  $L_x = L_y = 4$  km instead of a few meters) and the higher vibration isolation requirements [16]. The length of the

interferometer arms maximise the length change induced by the strain of the passing GW. A simplified diagram is shown in Figure 1.2, illustrating the basic working principle of such an instrument. An infrared laser beam is injected into a beam splitter that divides the light into the two Fabry-Perot cavities, being in the orthogonal arms. These cavities are equipped with an input test mass (ITM) and an end test mass (ETM) each, which are used as mirrors. Passing GW effectively change both arm lengths with  $\delta L_x$  and  $\delta L_y$  such that the measured difference is

$$\Delta L = \delta L_x - \delta L_y = h(t)L$$

where  $h(t)$  is the strain amplitude of the GW projected onto the detector (notice the analogy with mechanical strain). The phase difference between the two laser beams returning to the beam splitter changes with this differential length variation, enabling a photodetector to measure an optical signal proportional to the gravitational wave strain  $h(t)$  [1].

A picture of the LIGO Hanford Observatory in Washington State is shown in Figure 1.3, clearly illustrating the long interferometric arms.

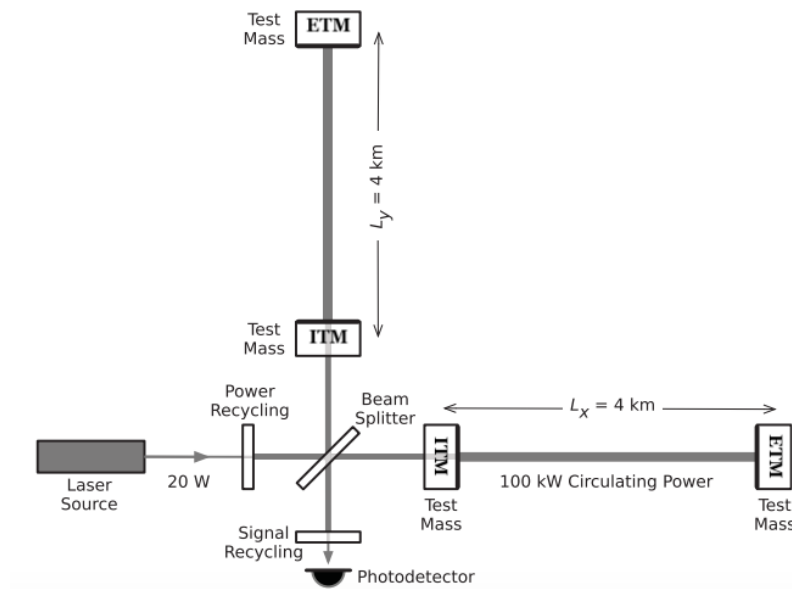


Figure 1.2 – A diagram of an aLIGO detector (not to scale)[1].

To reach the required sensitivity for measuring GW, one of the necessary adjustments, among several other enhancements to the basic Michelson interferometer, is to carefully isolate the test masses from external disturbances in such a way that they behave as ideal mirrors. This is performed by suspending each test mass as the final stage of a so-called *quadruple-pendulum* system, which is further detailed in Section 1.3.

### 1.3 Quadruple suspension

The working principle of the previously discussed laser devices require very good detection sensitivities and thus, very low noise levels. Therefore, besides a fastidious control of the large interferometer environment, a so-called *quadruple suspension* is used as a seismic isolation solution in the aLIGO detectors [6]. Actually, low-level earthquakes, human activity, ocean waves and wind drive the earth's surface motions. These motions are filtered



Figure 1.3 – A photograph of the LIGO Hanford Observatory in Washington State[2].

by the isolation stacks and pendulums of the quadruple suspension shown in Figure 1.4, enabling the required sensitivity. Each pendulum provides  $f^{-2}$  vibration isolation along

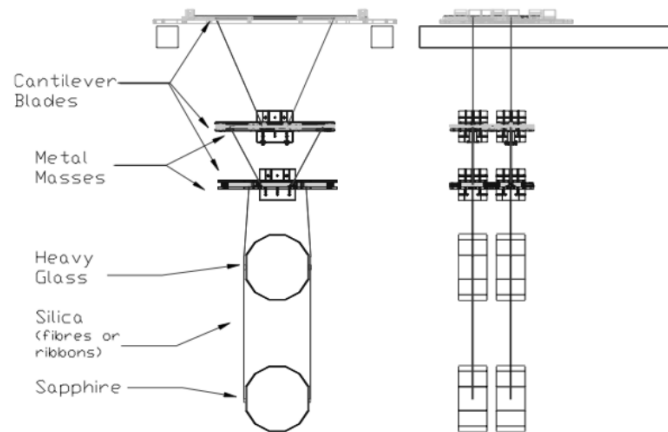


Figure 1.4 – Schematic diagram of quadruple pendulum suspension system for Advanced LIGO. The diagram above shows a face view of the main chain on the left, and on the right a side view with main and reaction chains is visible[3].

the beam direction above its eigenfrequency, so that the four stages combined provide approximately  $f^{-8}$  isolation above  $10Hz$ , giving an isolation factor of about  $10^8$  at  $100Hz$  [18]. The reaction chain shown in Figure 1.4 is used to provide a seismically isolated surface to actuate against when performing active damping of the different Degrees Of Freedom (DOFs) of the quadruple suspension [2].

## 1.4 Thermal Noise and Violin Modes

The sensitivity of the detectors is limited by the noise that is injected from various sources: quantum noise, seismic noise, gravity gradient that produces noise, suspension thermal noise and other sources, all contributing to the total sensitivity limit shown by the red line in Figure 1.5. The dominant broadband sensing noise source above 100 Hz is *shot noise* or *quantum noise*, which is caused by the fluctuation of the photon arrival rate (or, equivalently, of the power) [16] and is determined by the Poisson statistics of photon detection [4]. At the lowest frequencies (especially below 45Hz), the seismic noise is dominating

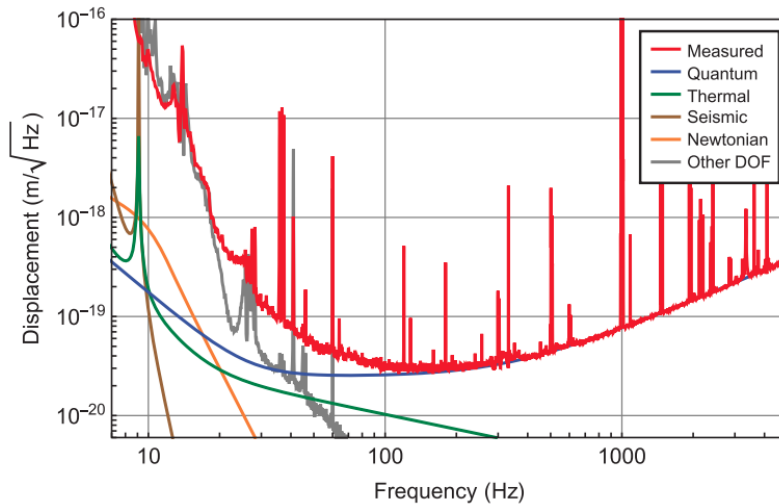


Figure 1.5 – The displacement sensitivity of the Advanced LIGO detector in Hanford; the Livingston detector has a similar sensitivity[4].

and is caused by motions of the earth's surface, filtered by the seismic isolation pendulums and stacks described in Section 1.3. The identification of the seismic contribution to the measurements is performed using accelerometers located at the quadruple suspension support points, whose signals are processed with transfer functions of the stacks and pendulums to estimate the resulting mirror motions [6]. The gravitational noise or *Newtonian* noise comes from sources of gravity perturbations, which are generally associated with fluctuating mass density in the vicinity of the test masses [19].

Mechanical thermal noise arises from the mechanical losses and is governed by the Fluctuation-Dissipation Theorem and also by the Equipartition Theorem [6, 20]. This thermal energy, combined with the fluctuating collision rate of the molecules of the surrounding dilute gas on the mirror surfaces, excite the pendulums' fibres and test mass, causing the so-called *suspension thermal noise* [21, 22]. From the Fluctuation-Dissipation Theorem, it is possible to prove that far from the resonant frequencies, the broadband thermal motion is proportional to the mechanical dissipation associated with the motion. The thermal energy is however highly concentrated at the system's resonant frequencies, which are designed to be as far as possible from the GW detection band. This can be seen from the green curve in Figure 1.5, where the narrow peak is located at the pendulum frequency. It can also be seen from the simple expression given in [16] for the power spectrum of the thermal motion of a 1 DOFs mass-spring-damper system based on the

Fluctuation-Dissipation Theorem:

$$x_{th}^2(f) = \frac{k_B T b}{\pi^2 f^2 (b^2 + (2\pi f m - \frac{k}{2\pi f})^2)} \quad (1.2)$$

in which  $T$  is the temperature,  $k_B \approx 1.38 \cdot 10^{23} JK^{-1}$  is the Boltzmann constant,  $k$  is the spring constant,  $m$  is the mass,  $f$  is the frequency and  $b$  is the damping coefficient reflecting the dissipation. This is why so much attention has been given the last decades to the reduction of damping in the suspension system, leading to a decreased level of thermal noise. This explains why a very low gas damping is necessary and why the design of suspension fibres has been a very critical research topic in order to reduce the losses associated with the anelastic bending of the fibres near the attachment points (*e.g.* design of very thin fibres to reduce these bending losses) [21]. However, the Equipartition Theorem states that each quadratic term in a system's Hamiltonian is excited by thermal noise to a mean energy of  $\frac{k_B T}{2}$ , and since for a multi-modal system every mode can be associated with quadratic kinetic and potential energy terms, their individual thermal noise spectra will contribute to the total noise [16]. Actually, besides the pendulum mode associated with the low-frequency peak in Figure 1.5, the pendulum system has an infinite number of modes associated to the suspension fibres (see Figure 1.6), causing additional spikes in the total thermal noise visible in Figure 1.7. This is why these suspensions fibres are made of fused

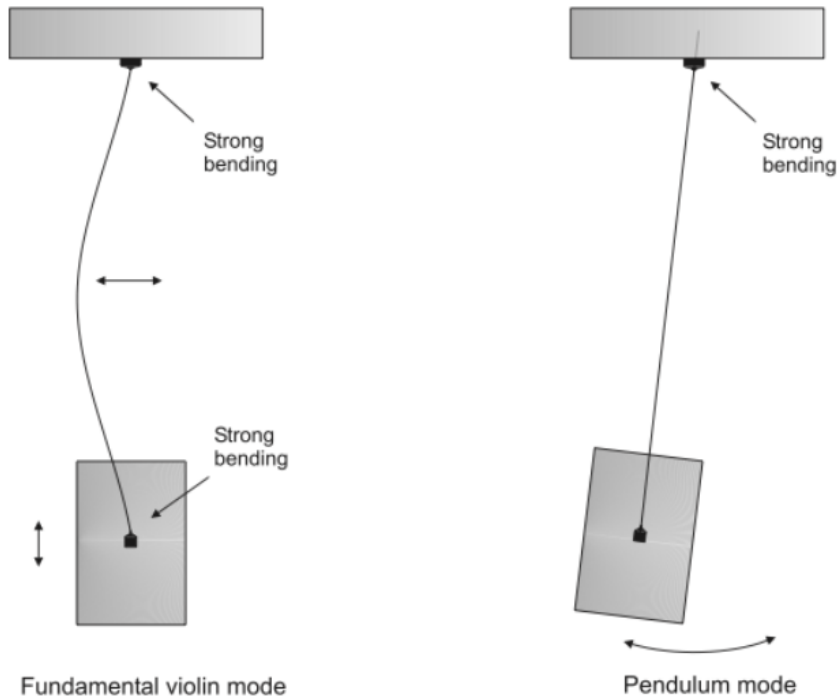


Figure 1.6 – The fundamental violin mode and the pendulum mode of a single suspension fibre pendulum, also showing the anelastic bending of the fibres near the attachment points. (figure from [5])

silica materials with very low loss angles  $\phi_w = \frac{1}{Q}$  where  $Q$  is the quality factor, thereby decoupling the fibre motions from the suspension's so-called *thermal reservoir*. [23, 4]. The majority of the high  $Q$  peaks in Figure 1.7 are due to power lines (60Hz, 120Hz, 180Hz, etc. from the 60Hz utility frequency in the U.S.), calibration lines (55Hz, 400Hz and 1100 Hz present due to calibration procedures) and fibre resonances (350Hz, 700 Hz, etc.) [6].

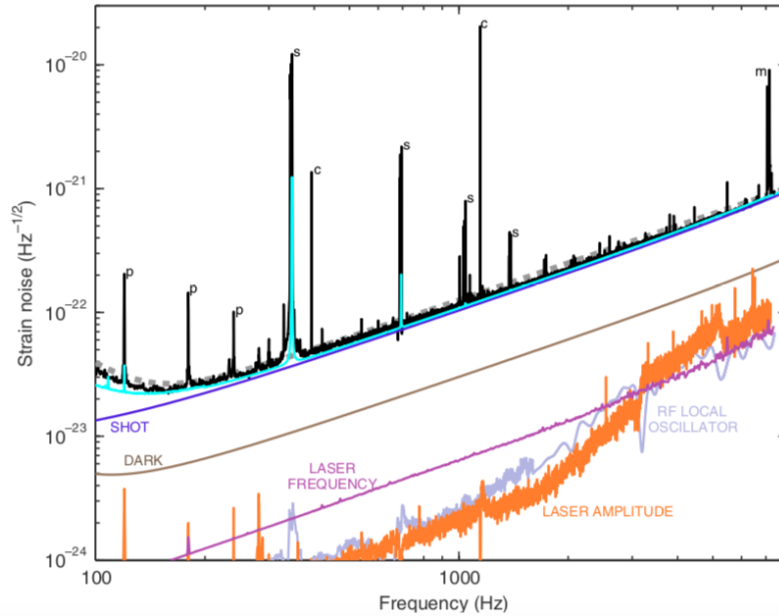


Figure 1.7 – The H1 detector noise spectrum. The black curve is the measured strain noise (same spectrum as the red line in Figure 1.5). The labeled spectral peaks are identified as follows: c, calibration line; p, power line harmonic; s, suspension wire vibrational mode; m, mirror (test mass) vibrational mode. (figure from [6])

The latter standing wave vibration modes are called violin modes due to the analogy with string instruments (see Figure 1.8). Indeed, to generate musical tones, the musician excites the standing wave vibrations of the strings generating sounds (through coupling with the acoustic field) that are amplified in a resonance chamber. Although these vibrations are treasured in the musical world, they are detrimental to the sensitivity of GW detectors. They may complicate the stable control of the interferometer and their very high quality factors ( $Q > 10^9$ ) [24] result in long ringdown times after any mechanical excitation, during which the detector output signal exceeds the acceptable dynamic range [10].

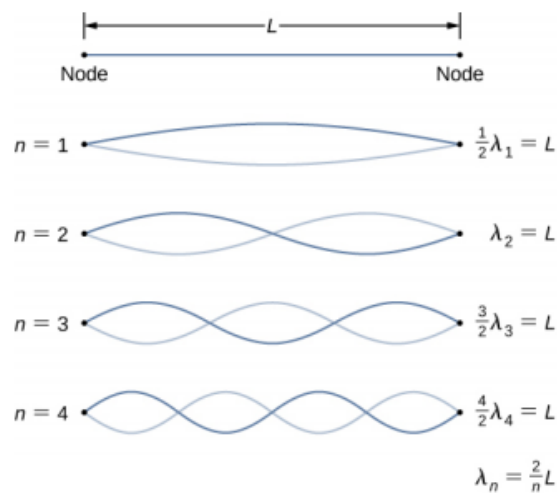


Figure 1.8 – The standing wave modes of a taut fibre with the corresponding wavelengths (figure from [7]).

Currently, high- $Q$  spikes are excluded from analysis by subtracting the recorded fibre motions from the measured motion of the test mass [23, 6, 25]. A possible solution is to use a Kalman filter based on the known dynamics of the fibres (with some uncertainties) to distinguish VMs signals from other contributions to the measured detector output [25]. Notch filters can also be used, simply suppressing all contributions to the noise within a narrow band [26]. However, this method does not distinguish VMs from other contributions like GW signals. The thermal noise excitation mechanisms will be further detailed in Section 2.4.

## 1.5 Motivation and goals

The aim of this work is to design an active solution for the vibration damping of VMs of the suspension fibres in GW detectors. At present, the only implemented solutions to reduce these vibrations involve mechanical design optimization for the suspension fibres, using high-purity materials and coatings. In fact, the measured VM signals still have to be suppressed at the signal processing level. Besides continuously seeking for the optimal material choice, ongoing research topics aim to damp these modes in a passive or in an active manner (see for example [10], [27], [28] and [29]). This would allow to avoid the signal post-processing steps which introduce a risk of altering GW signals.

The main objectives can be listed as follows

- Analyzing the nature of VM vibration dynamics
- Providing recommendations for active damping strategies
- Validating the theoretical outcomes experimentally
- Expanding to complex suspension structures

## 1.6 Project outline

From chapter 2, the reader can expect to learn about different mathematical formulations of the governing dynamics of a single suspension fibre. In Chapter 3, the latter mathematical outcomes are used to model the interactions with typical VM sensing and actuation devices and the different control strategies are developed accordingly. Chapter 3 also provides some numerical simulation results. The experimental results can be found in Chapter 4 along with a discussion of the validated theories and the limitations of the implemented control schemes. Finally, the dynamics of the main chain of the quadruple suspension are derived in Section 5.2.1, allowing to assess the influence of the active damping system on the rest of the suspension. A general conclusion and some suggestions for future research can be found in Chapter 6.

## Chapter 2

# Dynamic modelling of a single fibre

## 2.1 Introduction

Before thinking about strategies to actively reduce fibre vibrations, it is important to understand the dynamics of a single fibre, considered as an isolated system. Only then one can speak about control and active damping strategies, mainly based on the system dynamics. This chapter describes different ways to model a single suspension fibre. The equations remain linear in Section 2.2 and a somewhat different representation is developed in Section 2.3, introducing a nonlinear formulation that will be useful in Chapter 3. Normally, the vibration modes of the multiple silica fibres are also coupled with each other and with other parts of the suspension structure. There are some asymmetries and imperfections due to welding, silica evaporation from the fibres, etc. [29] and the fibre dynamics will be different from an identical but isolated fibre.

## 2.2 Linear models

This section justifies the use of linear dynamic expressions for the fibre motions in both a continuous and a discrete formalism, also showing the limitations of these representations for an extended model.

### 2.2.1 Analytical model

Consider a homogeneous fibre stretched between two clamps separated by a fixed distance  $L$  shown in Figure 2.1a and a differential element  $ds$  between  $z$  and  $z + dz$  presented in Figure 2.1b and let the externally applied transverse force be  $f(z, t)$  per unit length. The net transverse force is

$$(T \sin \alpha)_{z+dz} - (T \sin \alpha)_z \quad (2.1)$$

in which  $T$  is the tension in the fibre and  $\alpha$  is the angle between the section  $ds$  and the  $z$ -axis, as shown in Figure 2.1b. For small transverse displacements one can write

$$\sin \alpha = \frac{dy}{\sqrt{dz^2 + dy^2}} = \frac{\frac{dy}{dz}}{\sqrt{1 + \left(\frac{dy}{dz}\right)^2}} \approx \frac{dy}{dz} \quad \text{for } \frac{dy}{dz} \ll 1$$

Expanding 2.1 in a Taylor series yields

$$\left(T \frac{dy}{dz}\right)_{z+dz} - \left(T \frac{dy}{dz}\right)_z = \frac{\partial}{\partial z} \left(T \frac{dy}{dz}\right) dz + \mathcal{O}(dz)^2 + \dots$$

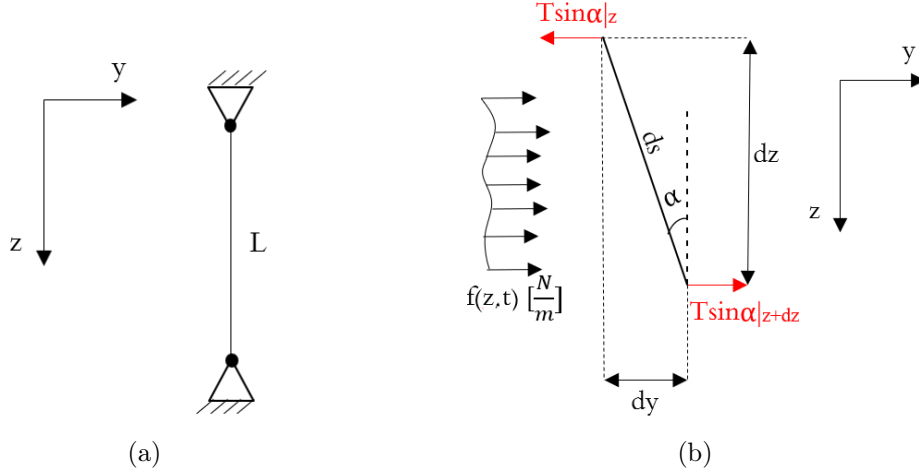


Figure 2.1 – The stretched continuous fibre with fixed ends conditions (left) and a section  $ds$  of a fibre in a deformed state (right).

from which only the first term will be used. Momentum conservation of the differential element requires that

$$\rho dz \ddot{y} = \frac{\partial}{\partial z} \left( T \frac{dy}{dz} \right) dz + f(z, t) dz \quad (2.2)$$

Taking  $dz \rightarrow 0$  the governing equation for the whole fibre becomes

$$\rho \ddot{y} = \frac{\partial}{\partial z} \left( T \frac{dy}{dz} \right) + f(z, t) \quad (2.3)$$

Assuming small planar transverse motions so that the tension can be considered as constant over the fibre length, the equations of motion (EOM) for the elastic fibre is nothing but a wave equation, which takes the same form as Equation (1.1).

$$\frac{\partial^2 y}{\partial z^2} - \frac{1}{v^2} \ddot{y} = -f(z, t) \quad (2.4)$$

where  $v = \sqrt{\frac{T}{\rho}}$  is the propagation velocity of transverse waves determined by the mass per unit length  $\rho$  and the tension  $T$  of the fibre [30]. The linearity of Equation (2.4) will be useful in further calculations. Searching for a solution of this wave equation arising in numerous contexts, one can suggest the readily adopted ansatz:

$$y(z, t) = A \sin(kz) \cos(\omega t - \psi) \quad (2.5)$$

with peak amplitude  $A$ , wavenumber  $k$ , wavelength  $\lambda = 2\pi/k$ , angular frequency  $\omega$ , and phase angle  $\psi$ . Substituting the latter equation into Equation (2.4) yields the so-called dispersion relation  $\omega = kv$ . Indeed, to force the fibre to be fixed by two clamps separated by a distance  $L$ , one can formulate the following conditions:

$$y(0, t) = 0 \quad y(L, t) = 0 \quad (2.6)$$

The second boundary condition is only satisfied when  $\sin(kL) = 0$ , which implies that  $k = n\frac{\pi}{L}$ , where the integer  $n$  represents the mode number. The trivial situation where

$n = 0$  describes the fibre at rest, while all other values of  $n$  are associated to the resonant transverse modes of the fibre with the following eigenfrequencies:

$$\omega_n = n\pi \frac{v}{L} \quad \text{for } n = 0, 1, 2, \dots \quad (2.7)$$

From this, one can see that an approximated solution can be found with a Rayleigh-Ritz discretization, which consists of approaching the solution of a variational problem by a finite sum of functions of forms:

$$y(z, t) = \lim_{N \rightarrow \infty} \sum_{n=1}^N q_n(t) \phi_n(z) \quad (2.8)$$

in which  $\phi_n(z)$  are the Rayleigh-Ritz mode shapes and  $q_n(t) = |q_n| \cos(\omega_n t)$  are the modal amplitudes, also called the generalized coordinates [31]. By neglecting the bending stiffness, the mode shapes can be approximated by simple sine functions (see Figure 1.8).

$$\phi_n(z) = \sin\left(\frac{n\pi z}{L}\right) \quad (2.9)$$

However, assuming the material to be a linear elastic solid, the finite cross-section of the fibres is responsible for a so-called *elastic distance*  $\Delta$ , which is the distance over the fibre bends near the clamps ( $\frac{\Delta}{L} \approx \mathcal{O}(10^{-3})$  for aLIGO). This elastic distance is approximately given by  $\Delta = \sqrt{\frac{EI}{T}}$ , where  $E$  is the Young modulus of the fibre material and  $I$  is the area moment of inertia around any direction normal to the  $z$ -axis [21]. This means that a more realistic mode shape would require a flexure correction (see Figure 2.2), which yields [32]

$$\phi_n(z) = \sin\left(\frac{2n\pi(z - \Delta)}{2(L - 2\Delta)}\right) + \frac{2n\pi\Delta}{2(L - 2\Delta)} \cdot \left(e^{\frac{z}{\Delta}} - (-1)^n e^{\frac{L-z}{\Delta}}\right) \quad (2.10)$$

This causes some small anharmonicity of the eigenfrequencies given by [33]

$$\omega_n = \sqrt{\frac{T}{L}} \frac{n\pi}{L} \left(1 + \frac{2\Delta}{L} + 4\left(\frac{\Delta}{L}\right)^2 + \left(\frac{n\pi\Delta}{L}\right)^2\right) \quad (2.11)$$

Also, despite the very high level of environmental control, these eigenfrequencies are not totally constant with time [29].

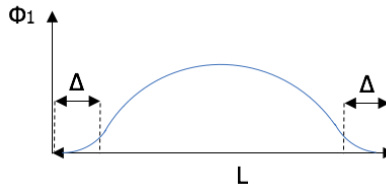


Figure 2.2 – The first mode shape with a flexure correction.

This linearized analytical model is unquestionably useful, since it allows to understand the basics of the fibre motions as well as the eigenfrequencies of the VMs. Nevertheless, one major limitation here is the fixed-ends condition, causing the model to be incompatible with boundary motions. Indeed, one should keep in mind that the quadruple pendulum is composed of fibres whose boundaries are moving and transmitting forces.

### 2.2.2 Finite Elements State Space Representation

In view of the linearity of Equation (2.4), which is the equation of motion governing the dynamics of a continuous fibre, one can think of a discretized model whose dynamics would be represented by a state space model. In order to do so, let's start from a fibre with rest length  $L$ , tension  $T$  and linear mass density  $\rho$ . A lumped mass representation is realized by concentrating the mass on  $N$  equally distanced points, whose individual masses are all identical and equal to  $m = \frac{\rho L}{N}$  (see Figure 2.3). The dynamics of the string are now described by a set of  $N$  equation of motion of the  $N$  lumped masses, which are derived as follows.

Consider the  $i$ 'th bead, attached to the beads  $i - 1$  and  $i + 1$  through weightless connections with equal lengths. If we consider no displacements in the longitudinal direction ( $z$ -direction), we get

$$\tan(\Theta_i) = \frac{y_i - y_{i-1}}{z_i - z_{i-1}} = (y_i - y_{i-1}) \frac{N}{L} \quad (2.12)$$

and for small transverse displacements

$$\Theta_i = (y_i - y_{i-1}) \frac{N}{L} \quad \text{for } \Theta_i \ll 1 \quad (2.13)$$

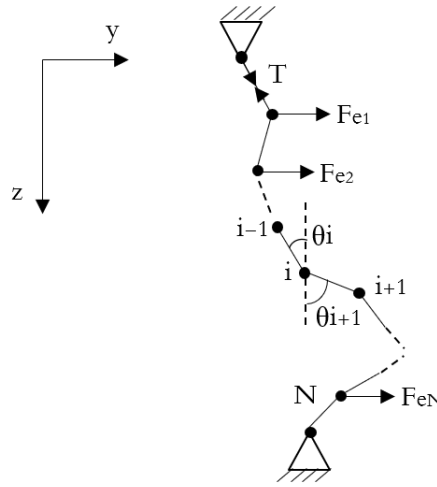


Figure 2.3 – The spatial discretization of a fibre into  $N$  lumped masses for a FE representation of its dynamics.

The EOM of the  $i$ 'th lumped mass is obtained by writing its force equilibrium

$$m\ddot{y}_i = -T \sin(\Theta_i) + T \sin(\Theta_{i+1}) \approx -T\Theta_i + T\Theta_{i+1} \quad \text{for } i = 2, 3, \dots, N - 1 \quad (2.14)$$

Using Equation (2.13), the latter equation yields

$$m\ddot{y}_i = \frac{TN}{L}(y_{i+1} - 2y_i + y_{i-1}) \quad \text{for } i = 2, 3, \dots, N - 1 \quad (2.15)$$

For  $i = 1$  and  $i = N$ , taking into account the external boundary forces  $Fe_1$  and  $Fe_N$  and

fixing the boundaries  $y_{N+1} = y_0 = 0$ , the EOM become

$$m\ddot{y}_1 = \frac{TN}{L}(y_2 - 2y_1) + Fe_1 \quad (2.16)$$

$$m\ddot{y}_N = \frac{TN}{L}(y_{N-1} - 2y_N) + Fe_N \quad (2.17)$$

Defining the vector of lumped mass positions as

$$\vec{y} = \begin{pmatrix} y_1 \\ y_2 \\ \vdots \\ y_N \end{pmatrix} \quad (2.18)$$

The system of equations of motion can be written in the following matrix form

$$M\ddot{\vec{y}} = -K\vec{y} + R\vec{F} \quad (2.19)$$

Where  $M = mI_{N \times N}$ ,  $\vec{F} = [Fe_1 \ Fee_2 \ \dots \ Fe_{N-1} \ Fe_N]^T$  is the vector of external transverse forces,  $R$  is a diagonal selection matrix allowing the activation of the individual external forces and

$$K = k \begin{pmatrix} 2 & -1 & 0 & 0 & 0 & \dots & 0 \\ -1 & 2 & -1 & 0 & 0 & \dots & 0 \\ 0 & -1 & 2 & -1 & 0 & \dots & 0 \\ \vdots & \vdots & \vdots & \vdots & \vdots & \ddots & \vdots \\ 0 & 0 & 0 & \dots & 0 & -1 & 2 \end{pmatrix}$$

where  $k = \frac{NT}{L}$ . Equation (2.19) can also be rewritten as

$$\ddot{\vec{y}} = -\Omega^2\vec{y} + \frac{1}{m}R\vec{F} \quad (2.20)$$

$$\text{with } -\Omega^2 = \begin{pmatrix} 2\omega_0^2 & -\omega_0^2 & 0 & 0 & 0 & \dots & 0 \\ -\omega_0^2 & 2\omega_0^2 & -\omega_0^2 & 0 & 0 & \dots & 0 \\ 0 & -\omega_0^2 & 2\omega_0^2 & -\omega_0^2 & 0 & \dots & 0 \\ \vdots & \vdots & \vdots & \vdots & \vdots & \ddots & \vdots \\ 0 & 0 & 0 & \dots & 0 & -\omega_0^2 & 2\omega_0^2 \end{pmatrix} \text{ and } \omega_0 = \sqrt{\frac{k}{m}} \quad (2.21)$$

Defining the state vector as

$$\vec{Y} = \begin{pmatrix} \dot{\vec{y}} \\ \vec{y} \end{pmatrix} \quad (2.22)$$

the state space representation becomes

$$\dot{\vec{Y}} = \begin{pmatrix} 0_{N \times N} & -\Omega^2 \\ I_{N \times N} & 0_{N \times N} \end{pmatrix} \vec{Y} + \frac{1}{m} \begin{pmatrix} R \\ 0_{N \times N} \end{pmatrix} \vec{F} = A\vec{Y} + B\vec{F} \quad (2.23)$$

clearly defining both the system matrix  $A$  and the input matrix  $B$ . If the output is chosen

to be the transverse reaction forces at the boundaries which are in local equilibrium with the internal forces of the fibre, one can derive the output matrix as follows:

$$fr_1 = -T \frac{\partial y}{\partial z} \approx -T \frac{y_2 - y_1}{z_2 - z_1} \approx -\frac{NT}{L}(y_2 - y_1) \quad \text{and} \quad fr_2 \approx -\frac{NT}{L}(y_N - y_{N-1}) \quad (2.24)$$

which yields

$$\begin{pmatrix} fr_1 \\ fr_2 \end{pmatrix} = C \vec{Y} \quad \text{with} \quad C = -\frac{NT}{L} \left( \mathbf{0}_{2 \times N} \mid \begin{array}{cccc} -1 & 1 & 0 & \dots & 0 \\ 0 & 0 & \dots & -1 & 1 \end{array} \right) \quad (2.25)$$

completing the state space representation of the fibre. One could also choose the position of any lumped mass to be the output by changing the matrix  $C$  correspondingly.

The latter model does not include the necessary boundary conditions. Adding a tip mass  $M_{tm}$  at  $i = N$  and a finite stiffness  $k_p$  (several orders of magnitude higher than  $k$ ) for  $i = 1$ , corresponding to the physical situation depicted in Figure 2.4, the EOM for  $i = 1$  and  $i = N$  become

$$m\ddot{y}_1 = -k_p y_1 + k(y_2 - y_1) + Fe_1 \quad (2.26)$$

$$M_{tm}\ddot{y}_N = k(y_{N-1} - y_N) + Fe_N \quad (2.27)$$

so that

$$K_{1,1} = k + k_p \quad K_{N,N} = k \quad \text{with} \quad k = \frac{M_{tm}gN}{L} \quad (2.28)$$

$$M_{N,N} = M_{tm} \quad (2.29)$$

where  $g \approx 9.81 \frac{m}{s^2}$  is the gravitational acceleration. Therefore, the system and input matrices turn into

$$A = \begin{pmatrix} 0_{N \times N} & -M^{-1}K \\ I_{N \times N} & 0_{N \times N} \end{pmatrix} \quad B = \begin{pmatrix} M^{-1}R \\ 0_{N \times N} \end{pmatrix} \quad (2.30)$$

The resulting system with  $N$  inputs and 2 outputs can now be used to simulate the response

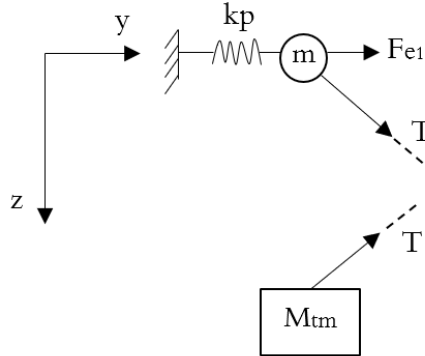
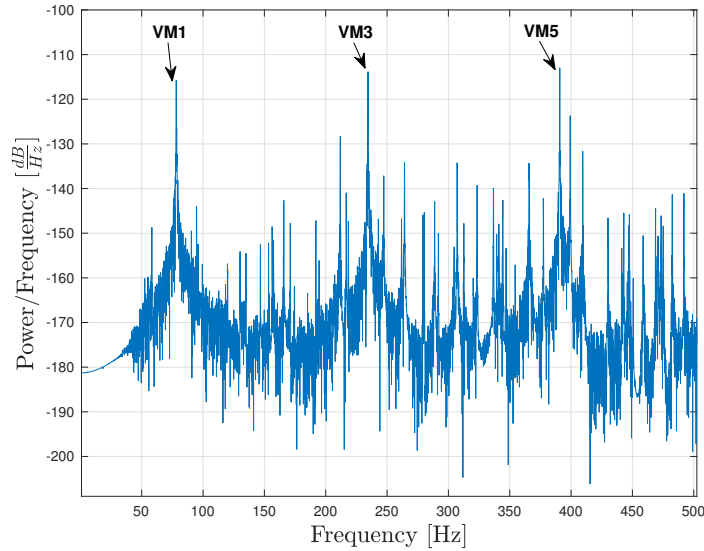


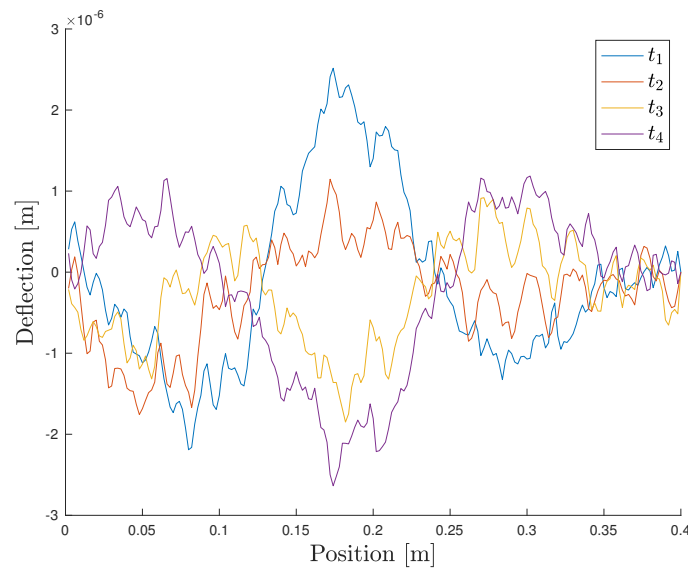
Figure 2.4 – Upper fixed-end boundary condition of the fibre with a penalizing stiffness  $k_p$  and a tip mass  $M_{tm}$ .

of the fibre to certain input forces. A Matlab script has been written (see Appendix C.2)

to evaluate the correctness of the model and to allow time domain simulations (using  $N = 200$ ,  $L = 0.4m$ ,  $M_{tm} = 1kg$ ,  $\rho = 2.5 \frac{g}{m}$  and  $k_p = 1.857 \cdot 10^6 \frac{N}{m}$ ). The expected VM frequencies are given by  $f_n = \frac{n}{2L} \sqrt{\frac{M_{tm}g}{\rho}}$ . Using a band-limited Gaussian white noise input at the upper fibre end, one can for example plot the power spectral density of the position of the middle of the fibre (see Figure 2.5a) and the shape of the fibres at specific times (see Figure 2.5b). The peaks in the power spectrum of the middle position correspond



(a)



(b)

Figure 2.5 – (a) The power spectral density of the position of the middle of the fibre; (b) the shape of the fibre at consecutive time steps ( $t_i = 2.5 + i \cdot \Delta T$  sec). The input force has a white Gaussian spectral content, which is band-limited between  $50Hz$  and  $500Hz$ . The simulation time is  $10s$  and the sampling frequency is  $f_s = \frac{1}{\Delta T} = 2kHz$ .

to the expected values of the frequency. Indeed, for the used parameter values, the VM frequencies are  $77.8Hz$ ,  $155.6Hz$ ,  $233.4Hz$ ,  $311.1Hz$ ,  $388.9Hz$ , etc. and since the middle of the fibre corresponds to a nodal point for even mode numbers, their frequencies are not

observed here. When the input force is sinusoidal with a frequency corresponding to one of the VMs, the obtained fibre shape takes the form of the corresponding mode shape (see Figure 2.6).

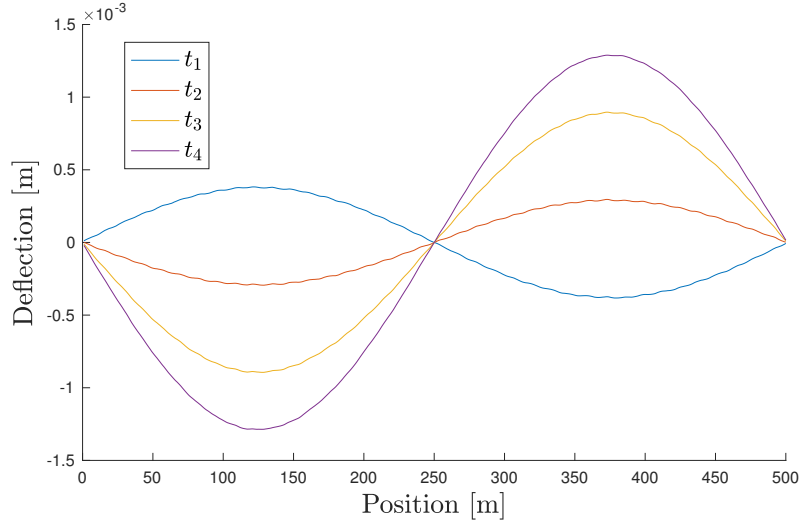


Figure 2.6 – The shape of the fibre at consecutive time steps ( $t_i = 2.5 + i \cdot \Delta T$  sec) for a sinusoidal excitation at the 2<sup>nd</sup> VM frequency  $f_2 = 155.6Hz$ .

Since the Multiple-Input Multiple-Output (MIMO) state space model obtained from the FE fibre representation is linear, it is possible to speak about transfer functions between different quantities, *e.g.* between force inputs and the horizontal force sensed by the suspended mass or at the suspension attachment. This will be useful to design a vibration controller in Chapter 3. In fact, one can already understand that looking at the transfer function between the force input  $F_{e1}$  and the force output  $fr_1$  would represent the open loop transfer function between the actuator and the sensor force for a horizontally mounted collocated pair (see Figure 2.7). Also, as expected, the pendulum mode of the suspension system appears in the open loop transfer function and its frequency is given by  $\omega_p = \sqrt{\frac{g}{L}}$ . By changing Equation (2.27), one can modify the model to have a suspension motion as input and the test mass displacement as output

$$m\ddot{y}_1 = k(y_e - 2y_1 + y_2) \quad (2.31)$$

where  $y_e$  is the motion of the suspension point. Knowing that the transfer function between the suspension motion and the test mass motion for a single DOF representation is given by

$$\frac{y_N(s)}{y_e(s)} = \frac{T}{LMs^2 + T} \quad (2.32)$$

one can compare this with the FE model, as in Figure 2.8, clearly showing the effect of the VMs on the motion transmission. From this figure, one can understand that high frequency seismic noise can contribute to the VMs spikes in the detector sensitivity.

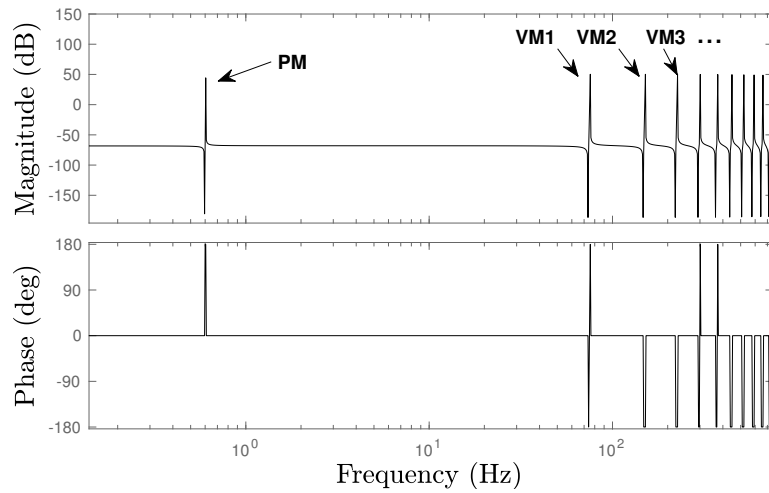


Figure 2.7 – Open Loop transfer function between a horizontal force actuator and sensor which are collocated at the fibre suspension point. The pendulum mode (PM) and the violin modes (VM) are clearly visible and their frequencies correspond to the expected ones.

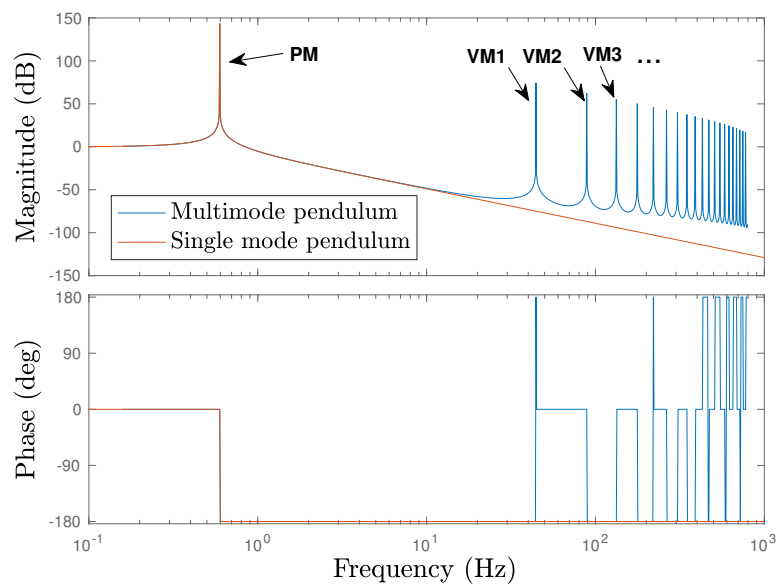


Figure 2.8 – The bode plot of the transfer function between the suspension motion and the test mass motion for a single degree of freedom pendulum and a multimode FE model, taking into account the VMs.

The FE model defined in spatial coordinates can also be projected on the modal basis by applying simple linear transformations. Defining  $\Phi$  as the basis of eigenvectors of the system containing the  $N$  mode shapes (see Figure 1.8)

$$\Phi = [\phi_1 \ \phi_2 \ \dots \ \phi_N] \quad \text{with} \quad \Phi_{j,k} = \sin(k\pi \frac{j}{N}) \quad (2.33)$$

one can then transform Equation (2.19) into a decoupled system of modal states  $\vec{r}$  by projecting the state vector  $\vec{y}$  into the eigenvector basis as follows:

$$\vec{y} = \Phi \vec{r} \quad (2.34)$$

so that

$$M\Phi\ddot{\vec{y}} = -K\Phi\vec{r} + R\vec{F} \quad (2.35)$$

Left multiplication of the latter equation by  $\Phi^T$  yields

$$M_m\ddot{\vec{r}} = -K_m\vec{r} + \vec{F}_m \quad (2.36)$$

where  $M_m$  is the diagonal modal mass matrix and  $K_m$  is the diagonal modal stiffness matrix and  $\vec{F}_m$  is the vector of modal forces. The resulting  $N$  equations are decoupled and, when converting Equation (2.36) to a state space representation, this discretization could be used to control the different VMs individually. Nevertheless, one major limitation of this projection is that input forces at the boundaries are cancelled by the zero amplitude of the mode shapes at these locations, since the boundaries are nodal points for any mode. Actually, an external force applied on a nodal point for a certain mode will be cancelled by its projection on the modal basis. On the contrary, if the external force is acting on an antinode of a certain mode, *i.e.* where the corresponding mode shape is maximum, the projection on  $\Phi$  maximizes the modal force for this mode. This is important to keep in mind, because it gives indications about the authority of an actuator on different modes, depending on where it is being placed.

## 2.3 Nonlinear model

In the linear model developed in Section 2.2.1, the tension was considered constant. This assumption disallows the modelling of the longitudinal dynamics, making its use irrelevant for the study of the interaction of the fibre with vertical forces. Indeed, a convenient model should include the coupling effects between transverse and longitudinal dynamics which is nonlinear, even for small oscillation amplitudes.

### 2.3.1 Single mode spring model

To account for the dynamic stretching causing a varying tension, a first approach is to consider a single mode model shown in Figure 2.9. The fibre is characterised by a weightless linear spring of length  $L_0$  with spring constant  $k$ , or 2 identical springs in series of length  $\frac{L_0}{2}$  and stiffness  $2k$ . A punctual mass is placed in the middle and its transverse displacement will be the considered degree of freedom. When both extremities are fixed, inducing a static tension in the fibre, the total length becomes  $\frac{L}{2}$ .

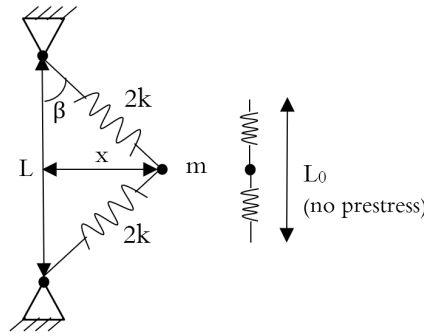


Figure 2.9 – The single mode model of a nonlinear fibre with one lumped mass and two identical springs.

The dynamics for the transverse lumped mass motion are derived in Appendix A.1 and after a series expansion one gets

$$\ddot{x} + \lambda \dot{x} + \omega_0^2 x (1 + \mathcal{K}x^2) = f(\omega t) \quad (2.37)$$

which takes the typical form of the well-known Duffing equation. The introduced constants have the following definitions

$$\omega_0^2 = 4 \frac{k}{m} \frac{L - L_0}{L} \quad \mathcal{K} = \frac{2L_0}{(L - L_0)L^2} > 0 \quad (2.38)$$

and  $f(\omega t)$  represents a harmonic forced acceleration while  $\lambda$  represents a linear viscous damping. This damped and forced oscillator equation has been studied extensively in the literature (see for example [34] or [11]) and is used in study of lateral vibrations of periodically loaded pin-ended columns for example. The stretching of the springs causes the restoring force to be a nonlinear function of the deflection, causing a hardening effect since  $\mathcal{K} > 0$  (for  $\mathcal{K} < 0$ , the non-linearity would lead to a softening effect). Despite the relatively simple form of this differential equation, the responses of such oscillators show some random phenomena like chaotic motions, bifurcations, shifting natural frequencies etc. . . [34, 35, 11]. A somewhat more detailed study of a modified duffing oscillator can be found in Section 3.3.2.

### 2.3.2 Continuous fibre model

Referring to the previously discussed continuous fibre with linear mass density  $\rho$  and length  $L$  shown in Figure 2.1a, consider the tension that has been employed until now as the sum of a static and a dynamic contribution

$$T = T_s + T_d$$

where the static tension  $T_s$  is constant over the length of the fibre and over time, while the dynamic tension  $T_d$  depends on the instantaneous strain in the following fashion

$$T_s = EA \left( \frac{L - L_0}{L} \right) \quad T_d = EA \epsilon_d(z, t) \quad (2.39)$$

where  $\epsilon_d(z, t)$  is the dynamic axial strain. This means that the tension in Equation (2.3) can not be considered as a constant over the fibre length anymore. Since a differential

element with a length  $dz$  is being deformed to  $ds$ , the axial strain can be obtained as

$$\epsilon_d(z, t) = \frac{ds - dz}{dz} = \frac{\sqrt{dz^2 + dy^2} - dz}{dz} \approx \frac{1}{2} \left( \frac{dy}{dz} \right)^2 \quad (2.40)$$

The latter equation shows that if at a given instant the fibre takes the shape of a perfect sine (*e.g.*  $\sin(2\pi \frac{z}{L})$ ), the dynamic tension along the fibre length will have the shape of a squared cosine, having a non-zero average value. By averaging the dynamic tension caused by the latter strain over the length of the fibre, causing it to be still a function of time, we get

$$T_d = \frac{EA}{L} \int_0^L \frac{1}{2} \left( \frac{dy}{dz} \right)^2 dz \quad (2.41)$$

Substitution of Equation (2.41) in Equation (2.3) yields

$$\rho \ddot{y} = T_s \frac{\partial^2 y}{\partial z^2} + \frac{EA}{2L} \frac{\partial^2 y}{\partial z^2} \int_0^L \left( \frac{dy}{dz} \right)^2 dz + f(z, t) \quad (2.42)$$

which takes the same form as the nonlinear transverse string EOM derived by Carrier *et al.* in [36], by Narasimha in [37] and by Gough *et al.* in [38]. It is important to notice the differences with Equation (2.4) which did not include the stretching effects. In order to compare these results with the single mode spring system described by Equation (2.37), consider first no external force  $f(z, t)$ . To adapt Equation (2.42) for a single vibration mode, one can write  $y_n(z, t)$  as the product of its mode shape function  $\phi_n(z)$  and its modal amplitude  $q_n(t)$ , which yields

$$\rho \phi_n \ddot{q}_n = T_s \frac{\partial^2 \phi_n}{\partial z^2} q_n + \frac{EA}{2L} \frac{\partial^2 \phi_n}{\partial z^2} \int_0^L \left( \frac{d\phi_n}{dz} \right)^2 dz q_n^3 \quad (2.43)$$

This is again a Duffing equation and can be compared with Equation (A.6) by evaluating it in  $z = \frac{L}{2}$  and for mode number  $n = 1$ . From Section 2.2.1, the mode shapes are known and the required derivatives become

$$\phi_n(z) = \sin\left(n\pi \frac{z}{L}\right) \quad \frac{\partial \phi_n}{\partial z} = \frac{n\pi}{L} \cos\left(n\pi \frac{z}{L}\right) \quad \frac{\partial^2 \phi_n}{\partial z^2} = -\left(\frac{n\pi}{L}\right)^2 \sin\left(n\pi \frac{z}{L}\right) \quad (2.44)$$

and the integral

$$\begin{aligned} \int_0^L \left( \frac{d\phi_n}{dz} \right)^2 dz &= \left( \frac{n\pi}{L} \right)^2 \int_0^L \frac{1}{2} \left( 1 + \cos\left(2n\pi \frac{z}{L}\right) \right) dz \\ &= \frac{1}{2} \left( \frac{n\pi}{L} \right)^2 \left( L + \underbrace{\int_0^L \cos\left(2n\pi \frac{z}{L}\right) dz}_{=0 \quad \forall n} \right) \\ &= \frac{(n\pi)^2}{2L} \end{aligned} \quad (2.45)$$

Substituting the latter results in Equation (2.43) for  $z = \frac{L}{2}$  and adding some distributed viscous damping  $\beta_d = 2\xi_n \omega_n \rho$ , the transverse equations of motion of the fibre for the  $n$ 'th

vibration mode turns into

$$\ddot{q}_n + 2\xi_n \frac{n\pi}{L} \sqrt{\frac{T_s}{\rho}} \dot{q}_n + \left(\frac{n\pi}{L}\right)^4 \frac{EA}{4\rho} q_n^3 + \left(\frac{n\pi}{L}\right)^2 \frac{T_s}{\rho} q_n = 0 \quad (2.46)$$

This allows to choose the parameters of the spring system in Figure 2.9 such that its behaviour is identical to that of the continuous fibre studied here above. Moreover, it is now possible to account for the nonlinear hardening effect in the continuous fibre, whose physical interpretation can be related to the one for the spring system. From Equation (2.46), one can see that the non-linearity of the EOM increases for higher axial stiffness  $EA$  and for higher mode number  $n$ . The latter can be understood from the higher number of consecutive bends along the fibre length, causing globally a higher hardening. Another important observation is that this equation allows no coupling between the different modes, while in general they are non-linearly coupled so that a mode with no initial energy will be excited by gaining energy from other modes [39]. However, it is much easier to study the behaviour of individual modes, assuming no inter-modal couplings. A first mode truncation (like in Section 2.3.1 for the first mode) can be studied by looking at  $y_n(z, t) = q_n(t)\phi_n(z)$ , while the real solution of the fibre dynamic response  $y(z, t)$  can be approximated with Equation (2.8). However, for modelling it is convenient (most of the time rather necessary) to truncate the high frequency dynamics (also called *residual dynamics*), leading to increased model uncertainties [8]. This is important to keep in mind when doing the control system design, especially when the controller can excite the residual modes, leading to the well known *spillover* phenomenon (see Chapter 3 for the control design).

## 2.4 Violin Mode excitation mechanisms

### 2.4.1 Guitar plectrum

To excite the fibre, one can think of pulling it in a lateral direction to give it an initial shape which is different from its equilibrium state. Releasing the fibre will cause it to vibrate in a way that depends on the location and the amplitude of the pulling force. This can be compared to a plucked guitar string (see Figure 2.10). The initial shape of the fibre

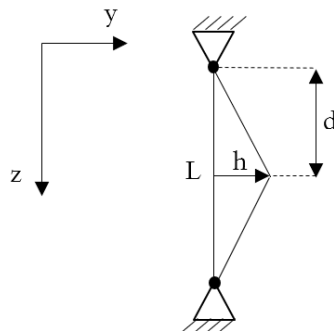


Figure 2.10 – The plucked fibre initial shape.

can be approximated by

$$y(z, 0) = \begin{cases} h \frac{z}{d} & \forall 0 \leq z < d \\ h \frac{L-z}{L-d} & \forall d < z \leq L \end{cases} \quad (2.47)$$

Remembering the Rayleigh-Ritz discretization from Section 2.2.1, one can compute the amplitude of  $q_n(t) = |q_n|e^{i\omega_n t}$  using the orthogonality of the mode shapes [40]

$$\begin{aligned} |q_n| &= \frac{2}{L} \int_0^L y(z, 0) \sin\left(\frac{n\pi z}{L}\right) dz \\ &= \frac{2h \sin\left(\frac{n\pi d}{L}\right)}{\frac{d}{L} \left(1 - \frac{d}{L}\right) \pi^2 n^2} \end{aligned} \quad (2.48)$$

The latter equation clearly shows that if the fibre is pulled exactly in a nodal point for a certain mode, the amplitude of that mode will be zero. However, in reality the couplings between the different modes cause energy transfers between these modes, making a zero modal amplitude impossible. Equation (2.48) also shows that for any value of  $d$  and  $h$ , the non-zero modal amplitudes decrease for increasing mode number.

### 2.4.2 Thermal noise

The previous calculations allow the modelling of the fibre response in the time domain from an initial condition. However, in the aLIGO suspensions, the VMs are excited continuously in the presence of thermal energy as seen in Section 1.4. It has been a very big challenge for the LIGO Scientific Collaboration (LSC) and the other members of the GW detectors community to identify the sources of dissipation and it seems that current research topics are still focused on correctly modelling these effects. However, some significant results emerged through the last decades. The thermal excitation of the VMs is mainly related to the sudden relaxation of mechanical stresses near the attachment points, and the thermal motion associated to the VM degrees of freedom, according to the Equipartition Theorem [41]. Actually, considering each VM with mode number  $n$  as a harmonic oscillator executing a one-dimensional motion, the average potential energy is equal to the average kinetic energy [42]. Using the Equipartition Theorem on the average kinetic energy of mode number  $n$  yields

$$\langle K_n \rangle = \frac{1}{2} \int_0^L \rho \langle \dot{y}_n^2(z, t) \rangle dz \quad (2.49)$$

$$= \frac{1}{2} k_B T_f \quad (2.50)$$

where  $\langle \dot{y}_n^2(z, t) \rangle$  is the time-averaged square velocity of mode  $n$  and  $T_f$  is the temperature of the fibre (see Section 1.4). Using again  $y_n(z, t) = q_n(t)\phi_n(z)$ , Equation (2.49) becomes

$$\langle K_n \rangle = \frac{\rho L \omega_n^2 |q_n|^2}{8} \quad (2.51)$$

Combining Equation (2.51) and Equation (2.49) gives the amplitude of the mode motions due to the thermal noise

$$|q_n|^2 = \frac{4k_B T}{\rho L \omega_n^2} \quad (2.52)$$

The latter equation shows that the thermal motion of the fibre increases linearly with the temperature as expected and that the modal amplitudes decrease quadratically with  $n$ , since  $\omega_n \propto n$ .

### 2.4.3 Electromagnetic excitation

Consider a ferromagnetic wire excited by an electromagnet, which consists of a wound copper coil placed at a short distance from the wire at a height  $z = p$  and perpendicular to it (see Figure 2.11). The wire can also be a non-ferromagnetic material on which a piece of ferromagnetic material is attached, near the electromagnet. To control the electromagnetic

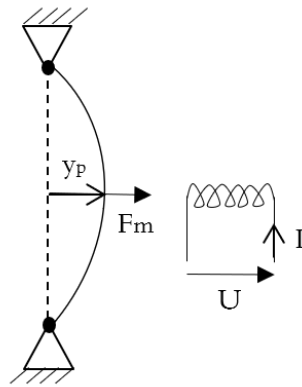


Figure 2.11 – The ferromagnetic wire excited by an electromagnet.

force acting on the wire, one should first understand the coupling between the electrical dynamics in the coil and the mechanical dynamics of the fibre. The electrical tension over the solenoid can be expressed as follows:

$$U = RI + \frac{d\phi_f}{dt} = RI + \frac{d\{L_f(y_p)I\}}{dt} \quad (2.53)$$

where  $R$  is the resistance,  $I$  is the current,  $\phi_f$  is the magnetic flux,  $L_f$  is the inductance and  $y_p = y(z, t)|_{z=p}$  is the vibration amplitude of the wire at the height of the coil. The flux passing through the coil is generated by the current and the relationship between both is assumed to be linear, with as proportionality factor the inductance  $L_f$ . Yet, this inductance is depending on the distance between the electromagnet and the wire. Assuming the electromagnet to be fixed, this distance is only dependent on the  $y_p$ . Further development of Equation (2.53) yield

$$U = RI + \frac{\partial L_f(y_p)}{\partial y_p} \frac{dy_p}{dt} I + L_f(y_p) \frac{dI}{dt} \quad (2.54)$$

The power is given by the product of the current and the tension

$$P = UI = RI^2 + \frac{\partial L_f(y_p)}{\partial y_p} \frac{dy_p}{dt} I^2 + L_f(y_p) \frac{dI}{dt} I \quad (2.55)$$

The mechanical part of this power can be expressed as the product of a force and a velocity:

$$F_m \frac{dy_p}{dt} = \frac{\partial L_f(y_p)}{\partial x} \frac{dy_p}{dt} I^2 \quad (2.56)$$

$$\Leftrightarrow F_m = \frac{\partial L_f(y_p)}{\partial y_p} I^2 \quad (2.57)$$

where  $F_m$  is the electromagnetic force, as shown in Figure 2.11. From Equation (2.57), one can see that  $\frac{\partial L_f(y_p)}{\partial y_p}$  is required to calculate the force acting on the wire. This could be obtained either using Finite Element Method Magnetics (FEMM) in a virtual environment or by measuring the inductance for several values of  $y_p$ , thereby constructing a lookup table that could be used for real-time control. More importantly, the magnetic force is proportional to the square of the current, meaning that for a given harmonic current injection  $I(t) = |I|\cos(\omega_I t)$ , the magnetic force becomes

$$F_m(t) = \frac{1}{2} \frac{\partial L_f(y_p)}{\partial y_p} |I|^2 (1 + \cos(2\omega_I t)) \quad (2.58)$$

which is always positive. Thus, the wire is excited at twice the current frequency by a continuously attractive magnetic force.

#### 2.4.4 Electrostatic excitation

An electrostatic actuation solution has been evaluated by Dmitriev *et al.* in [10] with two parallel electrodes installed near the fibre with a separation gap  $d_g$  and an electrical charge  $q_e$  deposited on the fibre between the electrodes.

Controlling the voltage difference  $U(t)$  between the two electrodes allows to generate a force on the fibre given by

$$F_e(t) = U(t) \frac{q_e}{d_g}$$

The main advantage of this solution is that the actuator can be placed anywhere along the fibre, with the electrostatic coupling between the plates and the fibre being the only source of interaction. Notice that this solution is similar to the electromagnetic actuator from Section 2.4.3, except that the generated force is a linear function of the input signal.

## Chapter 3

# Active damping of violin modes

### 3.1 Introduction

In this chapter, different types of sensors and actuators are discussed as well as the different ways to assess information about the state of the fibre (*i.e.* the vibration amplitude) and drive the actuator through a control filter in such a way that it will destructively interfere with the motions of a single fibre, extracting kinetic energy from it in a similar way as damping would do. In the case of linear systems, one can attempt to design a vibration control system whose primary objective is to increase the negative real part of the system poles, causing the resonance peaks to be attenuated in the dynamic amplification. Mounting a collocated actuator-sensor pair (meaning that the sensor and actuator are attached to the same degree of freedom) on a lightly damped flexible structures always leads to alternating poles and zeros near the imaginary axis. This property is useful for the design of active damping strategies with guaranteed stability [8].

In the nonlinear case, one can simply not speak of transfer functions and must rely on energy analysis or other methods.

A possible physical interpretation of an active damping system is that the actuator absorbs and dissipates mechanical modal energy by providing a force opposed to the modal velocity and therefore a negative mechanical power delivered to the vibrating fibre. Therefore, one can think of an open-loop system with no sensor where the actuator is exclusively powered by a negative active electrical power supply. This power supply dissipates the mechanical power from the fibre, previously converted by the actuator in active electrical power [43].

### 3.2 Sensing

Measuring VMs can be done in different ways. The choice of the sensor type mainly depends on the adopted active damping strategy and the required sensitivity. Some possible sensor configurations and technologies are discussed here, showing the different possibilities for sensing VMs.

#### 3.2.1 Vertical force sensor at the boundary

Consider a perfect vertical force sensor attached at the top end of the fibre (see Figure 3.1). In order to evaluate how the violin modes would be observed through such a sensor, reminding the expression for the dynamic tension  $T_d$  given by Equation (2.39) and Equation (2.40), one can compute the dynamic tension caused by mode number  $n$  as follows

$$T_{d,n}(z, t) = \frac{1}{2}EA \left( \frac{d\phi_n}{dz} \right)^2 q_n^2(t) \quad (3.1)$$

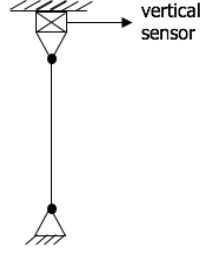


Figure 3.1 – The perfect vertical force sensor to measure the dynamic tension.

where  $\frac{d\phi_n}{dz} = \frac{n\pi}{L} \cos\left(n\pi\frac{z}{L}\right)$ . The dynamic force measured by the sensor at  $z = 0$  is thus given by

$$T_{d,n}(0, t) = \frac{EA}{2} \left(\frac{n\pi}{L}\right)^2 q_n^2(t) \quad (3.2)$$

If we write the modal amplitude as a harmonic function  $q_n(t) = |q_n|e^{i\omega_n t}$ , the latter equation becomes

$$T_{d,n}(0, t) = \frac{EA}{2} \left(\frac{n\pi}{L}\right)^2 |q_n|^2 e^{i2\omega_n t} \quad (3.3)$$

This shows that, due to the quadratic observability of any mode of number  $n$ , it is measured at twice its natural frequency  $\omega_n$ . For a physical interpretation of this phenomenon, one can think of pulling the centre of the fibre in one direction and then pushing it into the opposite direction. The effect of pulling or pushing on the measured vertical force is identical and when passing through the equilibrium position, a minimum tension  $T_s$  is reached. When one period is completed for the centre position, the measured vertical force has passed through two maxima and two minima, hence clarifying the doubled frequency. Moreover, it is important to note that despite the decreasing modal amplitude for increasing mode numbers (see Section 2.4), the factor  $n^2$  in Equation (3.3) compensates partially for that.

It is also important to notice that  $T(t) = T_s + T_d(t)$  is always positive (see Figure 3.2). Indeed, by performing a rough Order of Magnitude estimate for reasonable values of the

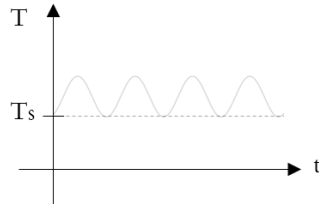


Figure 3.2 – Time plot of the fibre's total tension  $T(t) = T_s + T_d(t)$ .

parameters and assuming vibration amplitudes in the order of  $1mm$ , one can see that  $T_s \approx \mathcal{O}(10^1)N$  and  $|T_d(t)| \approx \mathcal{O}(10^{-1})N$  so that  $T(t) > 0 \forall t$ .

### 3.2.2 Horizontal force sensor at the boundary

Consider an ideal force sensor placed at the upper end of the fibre, sensing the transverse forces produced by the VM vibrations. The horizontal force at this location is given by

$$F_h = T \left( \frac{dy(z, t)}{dz} \right)_{z=0} \quad (3.4)$$

which yields for the linear FE model (see Section 2.2.2)

$$F_h = \frac{NT}{L}(y_2 - y_1) \quad (3.5)$$

and for the modal representation (see Section 2.3.2 and Section 2.2.1) the horizontal force caused by mode number  $n$  is given by

$$F_{h,n} = q_n(t)T \left( \frac{d\phi_n(z)}{dz} \right)_{z=0} = q_n(t) \frac{n\pi T}{L} \quad (3.6)$$

This shows that, in contrast with a vertical force sensor,  $q_n(t)$  is linearly observable and the measured frequencies will correspond to the ones of the VMs.

### 3.2.3 Piezoelectric sensors

The direct piezoelectric effect is the ability of certain crystalline materials to generate an electrical charge proportional to an externally applied force. This effect can be obtained below the *Curie temperature* after a poling process for some ceramics whose crystal structure have no center of symmetry [8]. The poling process enables to form an electric dipole on a macroscopic scale making the material permanently piezoelectric, so that it can convert mechanical energy into electrical energy and vice versa.

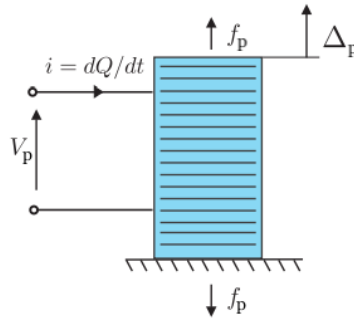


Figure 3.3 – A schematic representation of a discrete piezoelectric transducer (Figure from [8]).

Stacking multiple piezoelectric elements mechanically in series and electrically in parallel (see Figure 3.3) increases the charge output linearly for a given force input as shown in [8]

$$Q = C_c V_p + N_s d_{33} f_p \quad (3.7)$$

where  $Q$  is the total electric charge on the electrodes,  $f_p$  is the externally applied load,  $C_c$  is the capacitance of the transducer with no external load,  $N_s$  is the number of stacked elements,  $V_p$  is the applied voltage in Volts and  $d_{33}$  is the piezoelectric constant, expressed in  $\frac{m}{V}$ . By measuring the charge  $Q$ , one can linearly observe the force applied at the boundaries

of the transducer. Therefore, the previously mentioned force sensor arrangements (see Section 3.2.1 and Section 3.2.2) can be implemented with this type of sensors if the amount of stacked elements is sufficient to reach the required sensitivity for measuring VMs.

### 3.2.4 Other sensors

The shadow sensor designed by Lockerbie *et al.* [9] consists of a collimated near infrared beam illuminating the vibrating fibre whose oscillating shadow on the photodiode detector generates a modulated (differential) photocurrent at the VMs frequencies. This current

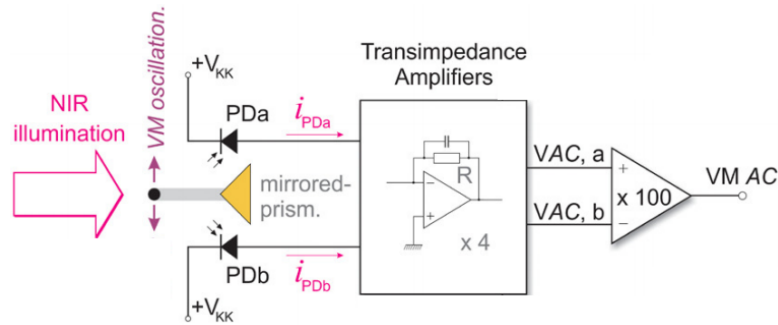


Figure 3.4 – The schematic of the VMs shadow sensor from [9]. The mirror-coated beam-splitting prism reflects the near infrared beam on the two reverse-biased photodiodes PDa and PDb. The beam splitting allows a factor  $\sqrt{2}$  improvement in signal-to-noise ratio.

is then converted into an oscillating voltage through a transimpedance amplifier (see Figure 3.4). This solution enables the detection of VMs of the silica suspension fibres at the  $10^{-10}\text{m}$  level.

Another sensing solution was developed by Dmitriev *et al.* based on the optical-beam deflection technique [10] (see Figure 3.5). A focused laser beam has an off-centered inci-

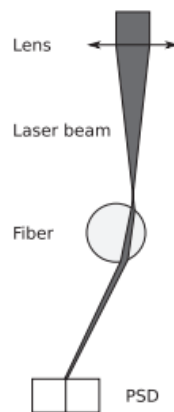


Figure 3.5 – The optical sensor based on the optical-beam deflection technique [10].

dence on the fibre, resulting in an angle deflection of the beam passing through the fibre, which acts as a cylindrical lens. Transverse displacements of the fibre cause the displacement of the laser spot on the Position Sensitive Detector (PSD). Analog PSDs produce output signals proportional to the true coordinates of the centre of the light spot on the detector using the lateral photoelectric effect [44].

The last VM sensor is also an optical device, consisting of a CCD camera, tracking the transverse motions of an optical target placed on the vibrating fibre [45]. However, since this sensor is used to measure vibrations of large cables (*e.g. in bridge structures*), the resolution is probably not high enough to measure VM vibrations in aLIGO (this could be investigated).

### 3.3 Actuation

Two actuation means are discussed here with their respective influences on the fibre dynamics. This is of critical importance to design controllers effectively and to better understand what is at stake when using them.

#### 3.3.1 Vertical Force Actuator: Parametric Excitation

In Equation (2.46), which is governing the nonlinear fibre dynamics, the coefficient for the linear restoring force is proportional to the fibre tension  $T_s$ . From this, one can imagine that this restoring force can be controlled by controlling the tension through a perfect vertical force actuator at one of the fibre ends (see Figure 3.6). This would regulate the total

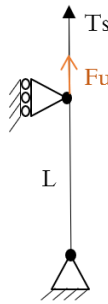


Figure 3.6 – The perfect force actuator exerting a force along the axial direction of the fibre.

tension to  $T(t) = T_s + T_d(t) + F_u(t)$  such that, assuming that the actuation force appears as a quasi-static axial loading superposed with the static tension (with  $|F_u(t)| < T_s$ ), Equation (2.46) turns into

$$\ddot{q}_n + 2\xi_n \frac{n\pi}{L} \sqrt{\frac{T_s}{\rho}} \dot{q}_n + \left(\frac{n\pi}{L}\right)^4 \frac{EA}{4\rho} q_n^3 + \left(\frac{n\pi}{L}\right)^2 \frac{T_s}{\rho} q_n + \frac{1}{\rho} \left(\frac{n\pi}{L}\right)^2 F_u(t) q_n = 0 \quad (3.8)$$

Thus mathematically one is led to a differential equation with an excitation appearing as a varying coefficient ( $F_u(t)$  in the last term of Equation (3.8)), which is therefore called a *parametric excitation* [11]. Furthermore, in contrast with small external excitations which can produce large responses near the natural frequencies of the system (called primary resonance), a small parametric excitation can produce a large response when its frequency is close to twice one of the natural frequencies of the system (called principal parametric resonance). Therefore, it is necessary to study the conditions for stability of such a parametrically excited system, especially if the objective is to damp the oscillations. This stability analysis can be found in Section 3.3.2. It is also very important to notice that this parametric excitation can only take place if there is an initial disturbance making  $q_n \neq 0$  in Equation (3.8). For example in cable-stayed bridges, parametric excitation of

the transverse vibration modes of the cables is possible through the presence of cable sag [46]. In our situation, since no sag is present, one can already foresee that the VMs will not appear in the open loop transfer function between the collocated vertical actuator and sensor.

### 3.3.2 Stability analysis of a parametrically excited fibre

The form of equations of motion for parametrically excited systems is given by Hill's equation in [11]

$$\ddot{\tilde{q}}_n + \left( \delta + \sum_{m=1}^{\infty} \epsilon^m f_m(t) \right) \tilde{q}_n = 0 \quad \text{with } f_m(t + \pi) = f_m(t) \quad (3.9)$$

However, this dimensionless equation is not general enough to include nonlinear and damping effects. To do so, one will need to deal with a parametrically excited Duffing equation with small damping, sometimes referred to as a *modified Mathieu equation* :

$$\ddot{\tilde{q}}_n + (\delta + 2\epsilon \cos(2\tau)) \tilde{q}_n = \epsilon g(\tilde{q}_n, \dot{\tilde{q}}_n) \quad \text{with } g(\tilde{q}_n, \dot{\tilde{q}}_n) = -\alpha \tilde{q}_n^3 - 2\mu \dot{\tilde{q}}_n \quad (3.10)$$

To relate the latter dimensionless equation to Equation (3.8), remembering that  $\omega_n = \frac{n\pi}{L} \sqrt{\frac{T_s}{\rho}}$  and writing  $F_u(t) = F_u \cos(\omega_u t)$ , the following transformations are necessary:

$$\begin{aligned} \tilde{q}_n &= \frac{q_n}{L} & \tau &= \frac{\omega_u t}{2} & \delta &= 4 \left( \frac{\omega_n}{\omega_u} \right)^2 \\ \epsilon &= 2 \frac{F_u}{T_s} \left( \frac{\omega_n}{\omega_u} \right)^2 & \hat{\mu} &= \epsilon \mu = 2 \xi_n \frac{\omega_n}{\omega_u} & \hat{\alpha} &= \epsilon \alpha = \frac{(n\pi)^4 EA}{L^2 \rho \omega_u^2} \end{aligned} \quad (3.11)$$

To study the combined effect of the nonlinear term and the parametric excitation on the amplitude and the phase of the lightly damped system, Nayfeh and Mook [11] used the method of multiple scales, enabling approximated stability conditions to be found. With this technique, one determines first the equations that describe the amplitudes and the phases, which are transformed into autonomous systems. Then, the singular points of these autonomous systems correspond to the steady state solutions of the considered system whose stability can be gathered from the stability of the singular points. Hence, the proposed ansatz for steady state motion is given by

$$\tilde{q}_n = a \cos \left( \tau - \frac{\psi}{2} \right) + \mathcal{O}(\epsilon) \quad (3.12)$$

where

$$\sin(\psi) = -8\xi_n \left( \frac{\omega_n}{\omega_u} \right)^2 \quad \cos(\psi) = 4 \frac{T_s}{F_u} \frac{\omega_u - \omega_n}{\omega_n} - \frac{3}{4} \alpha a^2 \quad (3.13)$$

and the approximated steady state amplitude  $a$  is given by

$$a^2 = \frac{8}{3} \frac{\left( 1 - 2 \frac{\omega_n}{\omega_u} \right)}{\hat{\alpha}} \pm \frac{4}{3} \frac{\sqrt{\epsilon^2 - 4(\hat{\mu})^2}}{\hat{\alpha}} \quad (3.14)$$

For a steady state solution to exist,  $a^2$  must be positive so that  $2\mu < 1$  or  $\epsilon > 2\hat{\mu}$  where  $\hat{\mu} = \xi_n$  for principal resonance ( $\delta \approx 1$  meaning  $\omega_u \approx 2\omega_n$ ). The physical interpretation of this

is that the amplitude of  $F_u$  must be great enough with respect to the damping coefficient to produce sustained motion. Regarding the influence of the excitation frequency  $\omega_u$ , the following results have been proved by Nayfeh and Mook ([11] Section 5.7.3) by determining the nature of the singular points associated to the different steady state solutions. The case in which  $|1 - 2\frac{\omega_n}{\omega_u}| < \frac{\sqrt{\epsilon^2 - 4\hat{\mu}^2}}{2}$  has one steady state solution and corresponds to a stable saddle point. The case in which  $2\frac{\omega_n}{\omega_u} < 1 - \frac{\sqrt{\epsilon^2 - 4\hat{\mu}^2}}{2}$  has two steady state solutions, where only the one with the higher amplitude is stable.

It is now possible to use these stability conditions to classify the solutions and to draw the associated transition curves defining boundaries between stable and unstable regions in the  $(\epsilon, \frac{\omega_u}{\omega_n})$ -plane (see Figure 3.7). Indeed, the three curves given by

$$\epsilon = 2\hat{\mu} \quad \text{and} \quad \frac{\omega_u}{\omega_n} = \left(1 \pm \frac{\sqrt{\epsilon^2 + 4\hat{\mu}^2}}{2}\right)^{-1} \quad (3.15)$$

separate 3 regions. It is important to keep in mind that even if these approximated boundaries are independent of  $\alpha$ , the behaviour of the solution is certainly affected by the nonlinearity in Equation (3.10). For a linearized system ( $\alpha = 0$ ), Region 2 would

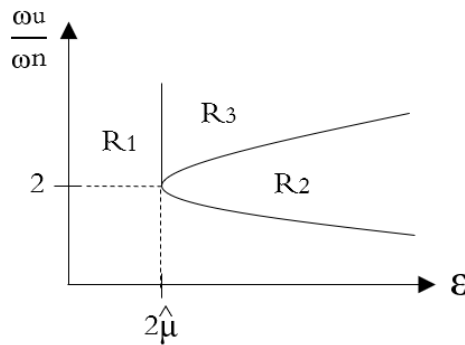


Figure 3.7 – The different regions in the parameter space for the classification of steady-state solutions of the damped and parametrically excited Duffing equation.

be characterised by responses with unbound growth for any initial disturbance while the nonlinear system seems to have a bounded solution. In Region 3 the response may either decay or converge to a sustained periodic motion, in contrast with the linearized system whose response could only decay. For Region 1, it appears that the responses decays for all initial disturbances. This can be explained by the fact that the phase is such that the parametric excitation force does negative work, thus contributing to the decay. For Region 2, the phase is such that the parametric excitation force injects more energy into the system than what is being dissipated, causing an unbounded response if  $\alpha = 0$ . However if  $\alpha > 0$ , nonlinear phase shifting effects will occur in the phasing (especially for large amplitudes), causing the response to be bounded and harmonic. For very large initial disturbances, the response decays until the steady-state solution is reached while for small initial amplitudes, the response grows until the nonlinearity is large enough to cause a phase-shifting. This means that all initial disturbances cause the same steady-state response, revealing the existence of a limit cycle (closed trajectory in the phase space). This phase shifting can be physically understood as a stiffening effect of the fibre at high vibration amplitudes, shifting its natural frequencies to higher values. In Region 3 the same reasoning can be

used to explain the decay mechanism as in Region 1 for some initial disturbances. However, for other disturbances the nonlinear term may have a large influence, inducing the same phase shifting effect as in Region 2. Both behaviours are thus possible, keeping in mind that only the largest of the two steady state solutions is stable. Even though the solutions are bounded in the whole parameter space, the steady state motions could be a potential danger for the considered fibre and its surroundings.

Another important observation is that in the vicinity of the parametric resonance, the inherent damping  $\xi_n$  determines the margin from falling into Region 2. Actually, the inequality  $\epsilon < 2\hat{\mu}$  that, if satisfied, locates the solution in Region 1 can be translated into

$$F_u < 4T_s\xi_n \quad (3.16)$$

giving a usable physical limit. Furthermore, one can extrapolate these results for a parametric excitation frequency that is close to the natural frequency by looking at the results for a linearized system described by the Mathieu equation:

$$\ddot{q}_n + 2\mu\dot{q}_n + (\delta + 2\epsilon \cos(2\tau))\tilde{q}_n = 0 \quad (3.17)$$

Even though the axes are a bit different, one can see that for  $\delta \approx 1$ , the transition curves are very similar (see Figure 3.8). When  $\omega_u \approx \omega_n$ , the damping has a highly stabilising effect,

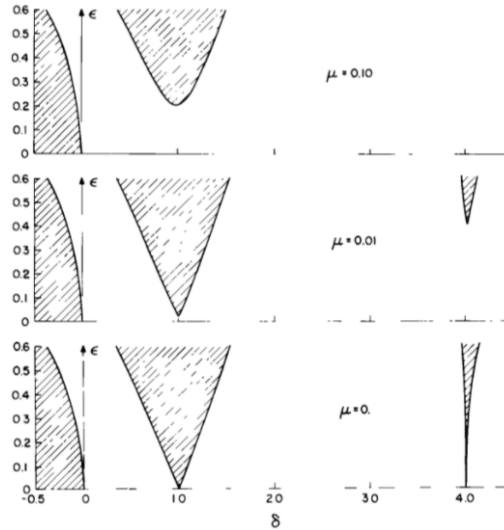


Figure 3.8 – The effect of viscous damping on the stability of the Mathieu equation around  $\omega_u = 2\omega_n$  and  $\omega_u = \omega_n$  (remembering Equation (3.11)). The shadowed regions define unstable solutions with unbounded amplitude growth. (Figure from [11])

making this region in the parameter space potentially less harmful than around parametric resonance. For a more detailed study of parametrically excited Duffing oscillators, one can look at [47] and for the bifurcation mechanisms [34].

### 3.3.3 Horizontal Force Actuator

The linear FE model from Section 2.2.2 allows to easily introduce a boundary horizontal actuation force in the fibre dynamics (see Figure 3.9). The EOM for the first element,

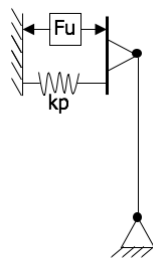


Figure 3.9 – The perfect horizontal force actuator  $F_u$ .

being attached to the actuator spring  $k_p$  becomes

$$m\ddot{y}_1 = k(y_2 - y_1) + F_u - k_p y_1 \quad (3.18)$$

so that the energy injected by  $F_u$  will propagate through the consecutive lumped masses. As already mentioned in Section 2.2.2, a projection on the modal basis does not allow energy injection at this boundary. In fact, the continuous linear model and the nonlinear model do not allow this neither. Therefore, simulations of such an actuator are only possible through the FE state space model.

### 3.3.4 Piezoelectric actuators

As seen in Section 3.2.3, the direct piezoelectric effect can be used for sensing forces applied on a piezoelectric transducer, converting mechanical energy into electrical energy. Actually, the opposite is also possible and is called the inverse piezoelectric effect. Indeed, applying an electric field in the polarization direction causes the piezoelectric material to expand. This can be seen in the following equation

$$\Delta_p = N_s d_{33} V_p + \frac{1}{k_p} f_p \quad (3.19)$$

in which  $\Delta_p$  is the total extension as shown in Figure 3.3 and  $k_p$  is the stiffness of the transducer with short-circuited electrodes ( $V_p = 0$ ). Equation (3.19) complements Equation (3.7) to form the piezoelectric transducer constitutive equations. Controlling the voltage allows to control the expansion of the piezoelectric material and this effect is again increased for a higher number of stacked elements, thereby reducing the required voltage levels [48]. This actuation mechanism can be used for the arrangements described in Section 3.3.3 and Section 3.3.1. In order to increase the actuation stroke, one can use *Amplified Piezo Actuator* (APA) systems, which use an external shell used both for the ceramic prestress and for the ceramic motion magnification [48].

The use of piezoelectric actuators in GW detectors is however questionable, mainly due to their heat generation caused by mechanical friction losses and dielectric losses (ferroelectric hysteresis being the major contribution) in the stacks [49, 50, 51]. Indeed, introducing a new source of thermal energy would increase the thermal noise level and thus

impair the sensitivity of the GW detector. Nevertheless, these heat generation effects are not covered by this work, which assumes perfect sensing and actuation devices.

### 3.4 Vibration Control Strategies

The latter actuation and measurement means could potentially be used to reduce the vibration amplitude of the VMs. The idea is to use information about the state of the fibre (*i.e.* the vibration amplitude) to drive the actuator in such a way that it will destructively interfere with the fibre motions. This section covers some proposals based on a vertical or a horizontal collocated sensor-actuator pair.

#### 3.4.1 Vertical collocated force actuator and sensor

Consider a stretched fibre with a perfectly collocated vertical force actuator-sensor pair at one of the boundaries (see Figure 3.14). The quadratic observability of the VMs has

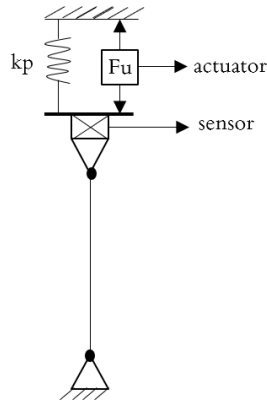


Figure 3.10 – The perfectly collocated vertical force actuator-sensor pair.

been proved in Section 3.2.1, demonstrating that they are measured at twice their natural frequencies. The actuation force, treated in Section 3.3.1, appearing as a parametric excitation term in the fibre dynamics will be used as the control input to actively damp the VMs. The non-linearity of the system with a collocated vertical pair disallows the computation of the transfer functions between the useful quantities, *e.g.* the modal displacement  $q_n$  and the actuation force  $F_u$ . Even if one neglects the cubic stretching term in Equation (3.8), the system remains non-linear in control. Therefore, classical active damping methods designed for linear systems cannot be used, *a priori*. However, they can be inspiring for the design of nonlinear active damping strategies based on energy analysis. The following sections describe some approaches, whose as primary objective is to extract kinetic energy from the fibre.

#### Active control based on energy analysis

With the objective of minimizing the total energy of the fibre, it is convenient to define a measure that quantifies the energy flow from the outer world to the fibre and vice-versa. This can be done by writing the energy production  $E_p$  as the integral of the product of a generalized force and the velocity  $\dot{q}_n$  over one period of oscillation of  $q_n$  [52]. Assuming a

harmonic oscillation for the  $n$ 'th mode

$$q_n(t) = |q_n| \cos(\omega_{d,n}t) \quad (3.20)$$

where  $\omega_{d,n} = \omega_n \sqrt{1 - \xi_n^2}$  and  $|q_n|$  is constant, one can propose the following ansatz for the vibration control

$$F_u(t) = A_u \cos(2\omega_{d,n}t + \phi_u) \quad (3.21)$$

where  $\phi_u$  is the phase shift between  $F_u$  and  $q_n$ . The energy flow into the fibre due to  $F_u$  is

$$\begin{aligned} E_{p,u} &= \int_0^{\frac{2\pi}{\omega_{d,n}}} \left( -\frac{1}{\rho} \left( \frac{n\pi}{L} \right)^2 F_u q_n \right) \dot{q}_n dt \\ &= -\frac{\pi}{2\rho} \left( \frac{n\pi}{L} \right)^2 A_u |q_n|^2 \sin(\phi_u) \end{aligned} \quad (3.22)$$

The detailed calculations for this can be found in Appendix A.2. The latter equation shows that this force input extracts energy from the fibre optimally when  $\phi_u = \frac{\pi}{2}$  and  $A_u > 0$ . Based on this, one can establish the following feedback control law

$$\begin{aligned} F_u(t) &= A_u \cos(2\omega_{d,n}t + \frac{\pi}{2}) = A_u \sin(2\omega_{d,n}t) \\ &= 2A_u \sin(\omega_{d,n}t) \cos(\omega_{d,n}t) = \frac{2A_u}{|q_n|^2 \omega_{d,n}} q_n \dot{q}_n \end{aligned} \quad (3.23)$$

During real-time measurements, there is no direct access to the vibration amplitude  $|q_n|^2$ . However, if one neglects this factor, the vibration damping will be much smaller for small oscillations, as the controllability decreases with a decreasing vibration amplitude (see Equation (3.8)). Theoretically,  $|q_n|^2$  can be measured as

$$|q_n|^2 = (|q_n| \cos(\omega_{d,n}t))^2 + (|q_n| \sin(\omega_{d,n}t))^2 = q_n^2 + \frac{1}{\omega_{d,n}^2} \dot{q}_n^2 \quad (3.24)$$

Given the previously stated assumptions and a perfect control of  $\phi_u$  such that no delay caused by finite sampling frequencies is introduced, the control law given by Equation (3.23) allows pure energy extraction from the fibre with an efficiency that can be evaluated by introducing an equivalent added damping. Indeed, the energy flow due to the viscous damping in Equation (3.8) can be expressed as

$$\begin{aligned} E_{p,\xi_n} &= \int_0^{\frac{2\pi}{\omega_{d,n}}} \left( -2\xi_n \frac{n\pi}{L} \sqrt{\frac{T_s}{\rho}} \right) \dot{q}_n^2 dt \\ &= -2\xi_n \frac{n\pi^2}{L} \sqrt{\frac{T_s}{\rho}} \omega_{d,n} |q_n|^2 \end{aligned} \quad (3.25)$$

The equivalent added damping due to  $F_u$  can be obtained by equating Equation (3.22) and Equation (3.25) where  $\xi_n$  is replaced by  $\xi_{a,n}$ , which yields

$$\xi_{a,n} = \frac{n\pi}{4\omega_{d,n}L\sqrt{\rho T_s}} A_u \quad (3.26)$$

In case there is some time delay so that  $\phi_u = \frac{\pi}{2} + \Delta\phi_u$ , the latter equation expression for  $\xi_{a,n}$  is multiplied with  $\sin(\frac{\pi}{2} + \Delta\phi_u) = \cos(\Delta\phi_u)$ , showing that delay effects are detrimental to the performance of this control law. Applying Equation (3.23) to the system described by Equation (3.8) results in an equivalent system with no feedback and a total damping factor  $\xi_{n,tot} = \xi_n + \xi_{a,n}$ . To measure the damping factor  $\xi_{n,tot}$  from a decaying oscillation measurement, one can use the logarithmic decrement method. With this method, one looks at the amplitude of two peaks  $q_n(t_0)$  and  $q_n(t_1)$ , where the second one takes place  $k_q$  oscillations after the first one ( $k_q = \frac{\omega_{d,n}}{2\pi}(t_1 - t_0)$ ). The damping factor is computed as

$$\xi_{n,tot} = \frac{1}{\sqrt{1 + \left(\frac{2\pi k_q}{\ln f_q}\right)^2}} \quad \text{with} \quad f_q = \frac{q_n(t_0)}{q_n(t_1)} \quad (3.27)$$

The effect of the active damping on the quality factor for a given VM can be computed from the equivalent added damping and the original quality factor  $Q_{or}$  of that specific mode

$$Q_{new} = \frac{1}{2\xi_{n,tot}} = \frac{1}{Q_{or}^{-1} + 2\xi_{a,n}} \quad (3.28)$$

where  $\xi_{a,n}$  is a linear function of the actuation amplitude  $A_u$ , as shown by Equation (3.29). Using the silica fibre parameters of aLIGO (see Appendix C.1), assuming  $Q_{or} = 10^9$  for the first VM, the new quality factor is shown as a function of the actuation amplitude in Figure 3.11. So, for  $A_u = 0.1N$  the quality factor of the first mode can be reduced by a factor  $10^5$  or 100 dB.

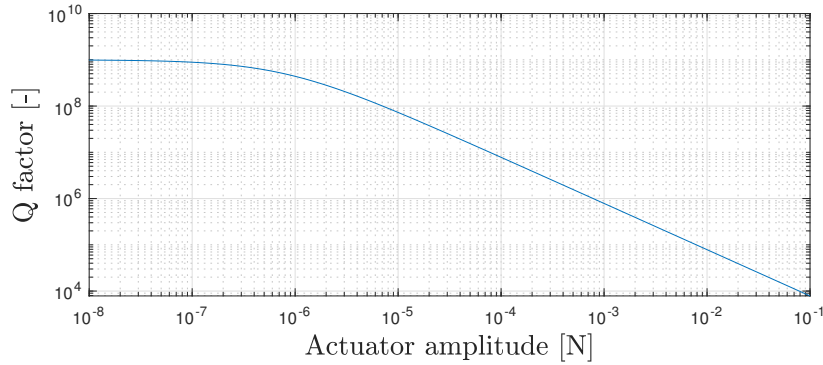


Figure 3.11 – The quality factor of the first VM as a function of the actuation amplitude  $A_u$ .

If the fibre vibration is only measurable through a vertical force sensor as described in Section 3.2.1, the latter control law can't be used directly. Assuming a perfect force sensor without any high-pass filtering, the measured quantity is  $T_{m,n} = T_s + T_{d,n}$ , from which  $T_{d,n}$  can be computed assuming  $T_s$  is known. To simplify notations,  $T_{d,n}$  will now be used instead of the previously used notation  $T_{d,n}(0, t)$ . From Equation (3.2), one can write

$$|q_n(t)| = \frac{\sqrt{2}L}{n\pi\sqrt{EA}}\sqrt{T_{m,n} - T_s} \quad (3.29)$$

Assuming again a harmonic oscillation  $q_n = |q_n| \cos(\omega_{d,n}t)$ , one can write

$$T_{d,n} = \frac{EA}{2} \left( \frac{n\pi}{L} \right)^2 |q_n|^2 \cos(\omega_{d,n}t)^2 = \frac{EA}{2} \left( \frac{n\pi}{L} \right)^2 \frac{|q_n|^2}{2} (1 + \cos(2\omega_{d,n}t)) \quad (3.30)$$

and its time derivative

$$\dot{T}_{d,n} = -\frac{EA}{2} \left( \frac{n\pi}{L} \right)^2 |q_n|^2 \omega_{d,n} \sin(2\omega_{d,n}t) \quad (3.31)$$

Using the latter equations, it is possible to see that the force sensor measurement can be used to apply the a nonlinear feedback law as follows

$$\begin{aligned} F_u(t) &= A_u \sin(2\omega_{d,n}t) \\ &= A_u \frac{-\dot{T}_{d,n}}{\frac{EA}{2} \left( \frac{n\pi}{L} \right)^2 |q_n|^2 \omega_{d,n}} \end{aligned} \quad (3.32)$$

in which, in a similar way as for Equation (3.24)

$$\frac{EA}{2} \left( \frac{n\pi}{L} \right)^2 |q_n|^2 = \frac{EA}{2} |q_n|^2 \left( \frac{n\pi}{L} \right)^2 (\cos^2(\omega_{d,n}t) + \sin^2(\omega_{d,n}t)) = T_{d,n} + \frac{\dot{T}_{d,n}^2}{4T_{d,n}} \quad (3.33)$$

from which one can finally write

$$F_u(t) = -\frac{A_u}{\omega_{d,n}} \frac{T_{d,n} \dot{T}_{d,n}}{T_{d,n}^2 + \frac{1}{4} \dot{T}_{d,n}^2} \quad (3.34)$$

If the DC component of the signal from the force sensor is suppressed (e.g. through high-pass filtering), the latter feedback law can't be used. In fact, from Equation (3.30) it is possible to prove that the measured quantity becomes

$$T_m = \frac{EA}{2} \left( \frac{n\pi}{L} \right)^2 \frac{|q_n|^2}{2} \cos(2\omega_{d,n}t) \quad \text{and} \quad \dot{T}_m = -\frac{EA}{2} \left( \frac{n\pi}{L} \right)^2 |q_n|^2 \omega_{d,n} \sin(2\omega_{d,n}t) \quad (3.35)$$

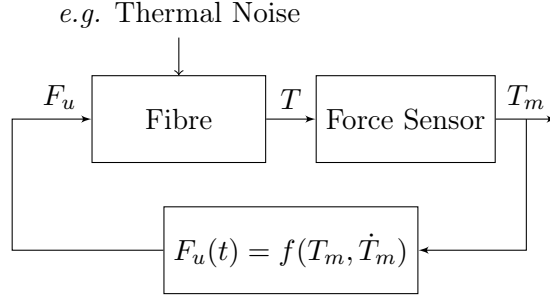
Thus, the optimal control turns into

$$F_u(t) = -A_u \frac{\dot{T}_m}{\frac{EA}{2} \left( \frac{n\pi}{L} \right)^2 |q_n|^2 \omega_{d,n}} \quad (3.36)$$

in which  $\frac{EA}{2} \left( \frac{n\pi}{L} \right)^2 |q_n|^2$  can be replaced by  $\sqrt{4T_m^2 + \left( \frac{\dot{T}_m}{\omega_{d,n}} \right)^2}$  so that

$$F_u(t) = -A_u \frac{\dot{T}_m}{\sqrt{(2\omega_{d,n}T_m)^2 + \dot{T}_m^2}} \quad (3.37)$$

This nonlinear feedback control can be represented by the following control scheme, assuming thermal noise to be the only disturbance source exciting the violin modes.



Since the measured quantity is now  $T_m(t)$  and not  $q_n(t)$ , one can not directly apply Equation (3.27) to compute the damping factor from the measurements. However, since  $T_m(t)$  oscillates at twice the frequency of  $q_n(t)$ , the interval  $[t_1 - t_0]$  contains  $k_T = 2k_q$  oscillations of  $T_m(t)$ . Moreover, since  $|q_n(t)| \propto \sqrt{|T_m(t)|}$ , one can write

$$\ln f_q = \frac{1}{2} \ln f_T \quad \text{with} \quad f_T = \frac{T_m(t_0)}{T_m(t_1)} \quad (3.38)$$

so that the same formula can be used as before (the factor of 2 cancels out) but with the tension measurement:

$$\xi_{n,tot} = \frac{1}{\sqrt{1 + \left(\frac{2\pi k_T}{\ln f_T}\right)^2}} \quad (3.39)$$

### Modified Integral Force Feedback

Because of the non-linearity of the control term in the plant dynamics, it is not possible to directly apply all the theoretical concepts of IFF, which is originally designed for linear systems (see Section 3.4.2). Nevertheless, one can imagine that this approach could potentially damp the vibrations in a similar way as the nonlinear derivative feedback from Section 3.4.1 does, since the measured vertical force at the top of the fibre is used to drive the vertical force actuator with a phase shift of  $\frac{\pi}{2}$ , leading to negative work. Writing again  $q_n(t) = |q_n| \cos(\omega_{d,n}t)$ , the IFF control signal can be written as

$$F_u(t) = |F_u| \int_0^t T_m(t) dt = |F_u| \frac{EA}{2} \left(\frac{n\pi}{L}\right)^2 |q_n|^2 \frac{1}{4\omega_{d,n}} \sin(2\omega_{d,n}t) \quad (3.40)$$

The latter equation shows that, in a similar way as for the derivative control feedback given by Equation (3.37), the IFF control will reduce the vibration energy of the fibre (this can be proved by looking again at the sign of the energy production calculated over one oscillation period). However, this control law does not damp small vibrations as good as large vibrations, so that its performance can be increased by dividing the feedback gain by  $|q_n|^2$ . In order to get the same equivalent added damping factor  $\xi_{a,n}$  (see Equation (3.29)) as with derivative feedback for the same value of  $A_u$ , the control law becomes

$$F_u(t) = A_u 4\omega_{d,n} \frac{\int_0^t T_m(t) dt}{|T_m|^2} \quad (3.41)$$

where, in contrast with the derivative control,  $A_u > 0$ .

Notice that the proposed nonlinear feedback laws do not show any optimal gain like classical IFF would do. In fact, the higher the gain, the more the vibration will be reduced,

at the expense of large required input forces and potentially high excitation of the system on which the actuator is mounted. Thus, the maximum damping will depend on the actuator specifications and on the rest of the system (see Section 5.2.1). Furthermore, a perfect integrator introduces a phase lag ( $-\frac{\pi}{2}$ ) and a  $-20dB$  per decade magnification while a perfect differentiator introduces a phase lead ( $+\frac{\pi}{2}$ ) and a  $+20dB$  per decade magnification. This means that applying these control laws on a real plant should be done carefully because high frequency noise could be problematic for a derivative control and low frequency noise would lead to saturation for the integrator (this is further detailed in Chapter 4).

### Other controllers

Fujino and Chen studied and implemented a system that is very similar to the derivative control discussed previously, with as main difference that a non-collocated Direct Velocity Feedback (DVF) controller is used with a CCD camera tracking the modal velocity  $\dot{q}_n(t)$  [52, 53]. Strategies based on the parametric excitation term in the nonlinear cable or string dynamics can be categorized as *active stiffness control*, where the output of the controller is a quadratic function of the target mode, so that the actuator signal fluctuates at a frequency that is twice that of the controlled mode [46].

The control law developed by Onoda *et al.* is based on a nonlinear saturation controller (sometimes called *bang-bang* control), which can be written as

$$F_u(t) = \begin{cases} -A_u & \text{for } q_n \dot{q}_n < 0 \\ A_u & \text{for } q_n \dot{q}_n > 0 \end{cases} \quad (3.42)$$

However, applying this to a taut string leads to spillover instability [54].

Notice that the strategies of Fujino, Chen and Onoda are all likely to be affected by spillover, occurring when non-modelled high-frequency modes are measured by the sensor (*observation spillover*) and are excited by the actuators (*control spillover*) [46]. Indeed, the advantage of using a collocated pair is that the dynamics of the structure do not need to be known, which allows to implement unconditionally stable control laws [8].

### Simulink models for vertical control

In order to understand how the relative phase of the vertical actuation signal with respect to the modal amplitude influences the damping effect, a simulation is performed using Simulink where an external sinusoidal modal force (*e.g.* thermal noise) of frequency  $f_1$  is applied on the fibre and a sinusoidal parametric excitation is applied at twice that frequency. This is done using a nonlinear fibre block in Simulink (see Figure B.1 in Appendix B) that takes the vertical control force and an external modal force as input and the dynamic tension as output. It also allows for an easy visualisation of the modal vibrations. The relative phase between the parametric excitation and the modal force is shifted over time, resulting in an evolution of the modal amplitude envelope as shown in Figure 3.12. The numerical integration is performed using a fixed-step 4th order Runge-Kutta algorithm. The parametric actuation is applied after 10 seconds to allow the motion to be in a steady state regime (due to the external sinusoidal force). The phase is shifted slowly to make the envelope correspond to the modal amplitude in steady state conditions. The figure clearly shows that a relative phase difference of  $\frac{\pi}{2}$  results in a positive energy injection while a phase difference of  $-\frac{\pi}{2}$  results in a negative energy injection. The slope of

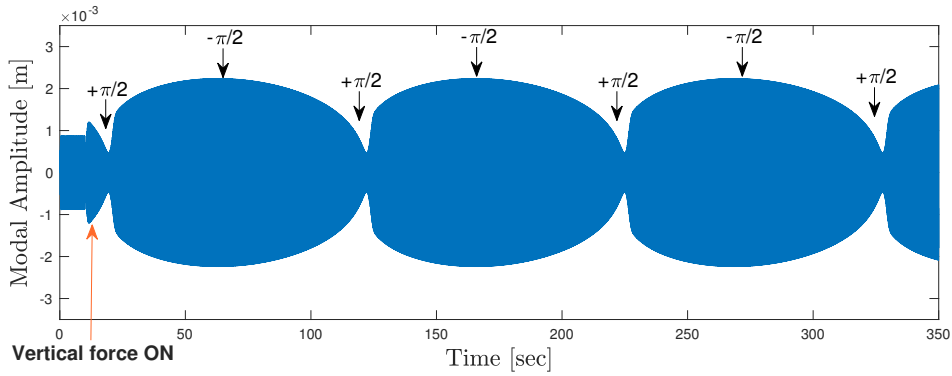


Figure 3.12 – The first mode vibration amplitude envelope for a sinusoidal magnetic excitation with a frequency  $f_1$  and a vertical sinusoidal force excitation at  $2f_1$  activated after 10 sec. The phase delay of the vertical excitation with respect to the string’s first mode motion is shifted over time, showing an optimal phase difference around  $\frac{\pi}{2}$ .

the envelope just after reaching a minimum is high because of the nonlinear phase shifting effect discussed in Section 3.3.1. In Chapter 4, it will be shown that this behaviour is also observed in the experimental results for the real plant.

For a vertically mounted collocated force actuator-sensor pair, both IFF and derivative control have been implemented in Simulink. The quadratic modal amplitude has to be estimated through the tension measurement to increase the control efficiency at low vibration amplitudes (see *e.g.* Equation (3.37)). However, due to finite time steps in numerical simulations, the numerator causes some problems caused by discontinuities. This can be solved by using an amplitude estimator, allowing to rewrite Equation (3.37) as

$$F_u(t) = A_u \frac{\dot{T}_m}{|\dot{T}_m|} \quad (3.43)$$

A custom made Simulink block has been made using a *sample and hold*, triggered by a decrease detector and filtered by a first order low-pass filter to avoid discontinuities (see Figure B.2 and Figure B.3 in Appendix B). The two control schemes are shown in Figure B.4 and Figure B.5. By simulating with the parameters given in the Matlab script in Appendix C.1, one can analyze the obtained modal dynamics with both control methods (see Figure 3.13). In this simulation there is no external force, but only an initial position

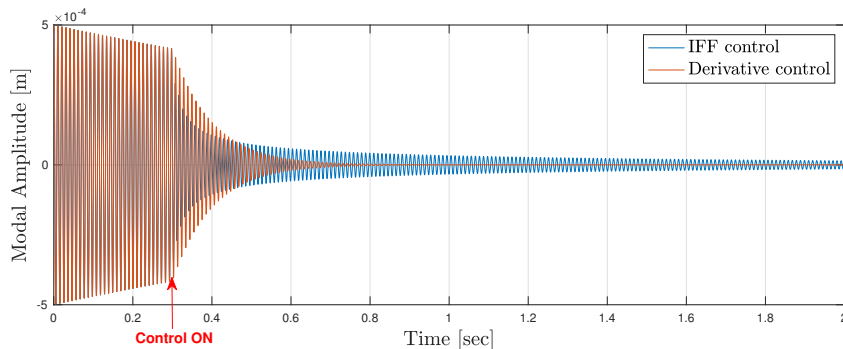


Figure 3.13 – A comparison between simple IFF ( $A_u = 10^6$ ) and derivative feedback with amplitude estimation ( $A_u = -0.5$ ).

for the modal amplitude. This clearly shows the effect of dividing the control signal by the estimated amplitude. The effect of viscous damping is visible through the decay when the control is not yet activated. The equivalent added damping for the derivative feedback computed by applying the logarithmic decrement on the modal amplitude signal corresponds to its expression given by Equation (3.29).

### 3.4.2 Horizontal collocated force actuator and sensor

Assuming only horizontal forces, the EOM for the first element in the FE model from Section 2.2.2 with a perfectly collocated horizontal force actuator-sensor pair becomes

$$m\ddot{y}_1 = k(y_2 - y_1) + F_s \quad F_s = F_u - k_p y_1 \quad (3.44)$$

where  $F_s$  is the force measured by the sensor. Defining the system output as  $F_s$ , the output state space matrices ( $C_{1 \times 2N}$  and  $D_{1 \times N}$ ) become

$$F_s = C\vec{Y} + D\vec{F} \quad \text{with} \quad \begin{cases} C = (\mathbf{0}_{1 \times N} \mid -k_p \ 0 \ 0 \ \dots \ 0) \\ D = (1 \ 0 \ 0 \ \dots \ 0) \end{cases} \quad (3.45)$$

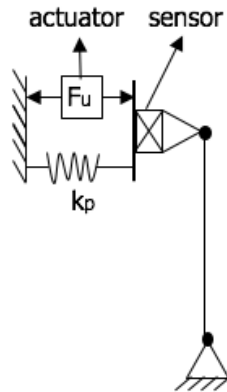
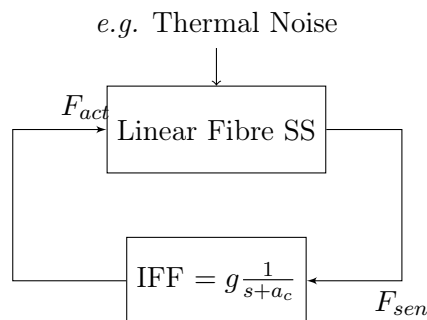


Figure 3.14 – The perfectly collocated horizontal force actuator-sensor pair.

The resulting state space representation of the suspension fibre allows to study the response of the system to different disturbances in the controlled and uncontrolled case. Closing the loop can be done as in the following block diagram. The transfer function  $\frac{g}{s+a_c}$  acts as an integrator from a certain frequency  $a_c$ , which allows to avoid saturation generally associated with integral control.



It is important to remember that the FE model represents planar motion only, while a real fibre has two orthogonal transverse vibration directions. These two directions are coupled, so that energy transfer between both is undeniable [37]. As a consequence, active damping on one of the two directions will also damp the vibrations in the other direction, which is desirable.

### Numerical simulations for horizontal control

With the latter control law, one can look at the root locus of the control (see Figure 3.15 obtained using the Matlab script in Appendix C.3). The open-loop poles are the natural

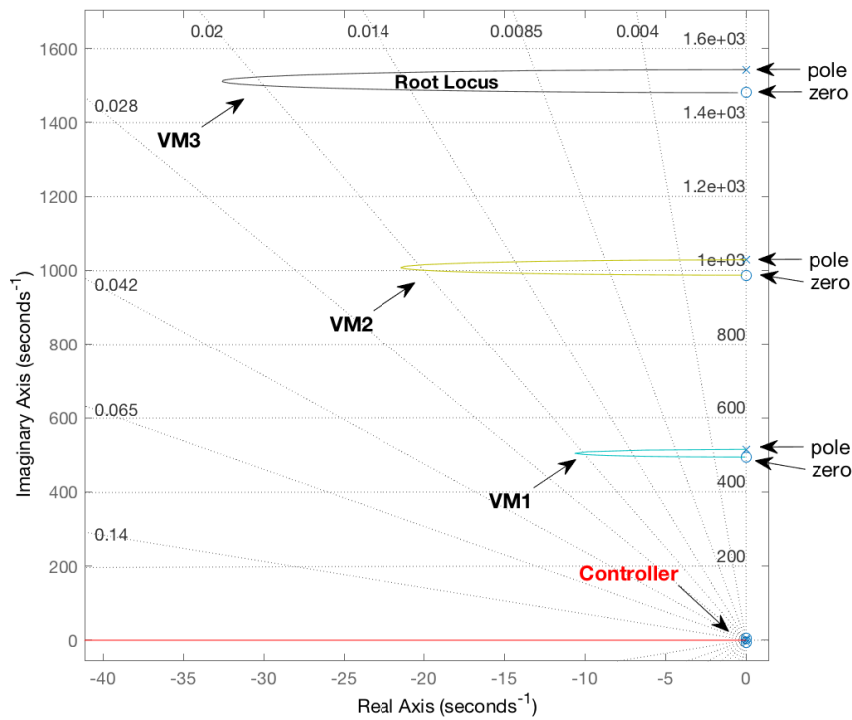


Figure 3.15 – The root-locus of the IFF, showing the migration of the poles towards the zeros for an increasing feedback gain. The units for both axes are in  $\frac{rad}{s}$ .

frequencies of the structure with the active element working passively (contributing with its own stiffness  $k_p$ ). The open-loop zeros are the natural frequencies of the system when the active element is removed [8]. As there is no damping introduced in the dynamics, the poles and zeros of the VMs are on the imaginary axis (or very close to it, due to numerical errors). Figure 3.15 shows that an increased feedback gain  $g$  causes the poles to migrate towards the zeros. Defining the optimal gain as the one that maximizes the negative real part of the pole associated to the mode of interest (and so, the modal damping), one can analyse the root locus to find it. In fact, since the different loops are travelled at different 'speeds' and  $g$  is the only decision variable, the optimal value of  $g$  for one mode will not necessarily be optimal for another one. This way, one mode can be selected to be damped the most. Furthermore, the higher the distance between the poles and their associated zeros, the better the corresponding modes can be damped because the root loci go further into the left complex half plane.

Using the fibre parameters defined in Appendix C.1, with the collocated pair placed 2cm below the attachment point, the optimal gain for the first mode is around  $10^6$ , causing an equivalent damping of  $\xi_1 = 0.014$ ,  $\xi_2 = 0.010$  and  $\xi_3 = 0.007$  for the first, second and third VM respectively. This result can be illustrated with the comparison between the open loop and closed loop transfer function of the collocated pair. The open loop transfer function was shown in Figure 2.7 and is now compared with the closed loop transfer function in Figure 3.16. Moving the latter to 4cm below the attachment point and using the same

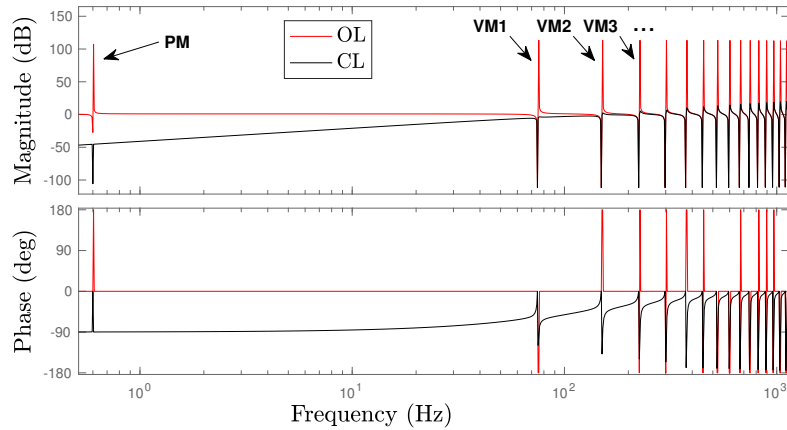


Figure 3.16 – Open Loop vs. Closed Loop transfer function between force actuator and sensor for a feedback gain of  $10^6$  and an integrator  $\frac{1}{s}$ . The pendulum mode (PM) and the VMs are all present in these transfer functions, clearly showing the corresponding poles and zeros.

feedback gain, a damping  $\xi_1 = 0.020$  can be obtained, showing again the low authority on these modes near the attachment points.

The effect of applying this control on the transmissibility from suspension point motion to test mass motion is shown in Figure 3.17.

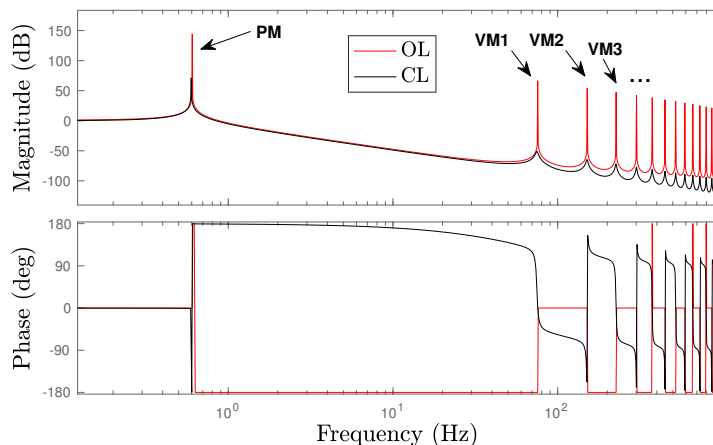


Figure 3.17 – The transmissibility transfer function from ground motion (at the suspension point) to test mass motion with and without IFF control.

### 3.5 Conclusion

Different control strategies have been developed in this chapter with two collocated actuator-sensor pair configurations. The first one, being a vertical mount, allows to damp the VMs through a parametric control, using a derivative or an integrating feedback law. For the horizontal mount, where the equations remain linear, an IFF control has been proposed. All of these have been simulated with the adequate fibre models (Simulink for parametric control and state space for horizontal control) allowing to understand how the proposed strategies perform. For a vertical mount, classical IFF control originally designed for linear systems has been proven to have very low performances at low vibration amplitudes. Therefore, a modified solution has been proposed. For the horizontal mount, the classical IFF is applied successfully, which can be expected from the linearity of this configuration. However, the small distances between the poles and zeros reduce the authority on the corresponding modes a lot. One could think of moving the collocated pair down to increase this authority but this can be detrimental to the seismic isolation performances of the pendulum.

The main advantage of IFF is that all the observable and controllable modes are damped and stability is in principle guaranteed regardless of the value of the gain and the structure on which it is acting (linear or not) [8]. Another important comment is that a vertical mount allows to damp vibrations in both transverse directions, while a horizontal mount only acts in one direction. However, the nonlinear couplings allow to damp the vibrations in the other direction, as mentioned before.

The designed Single-Input Single-Output (SISO) control laws constitute decentralized feedback loops in each active mount. Indeed, the quadruple pendulum has multiple fibres which all need to be controlled. As will be seen in Section 5.2.1, there might be some stability issues due to the other DOFs of the quadruple suspension, so that a centralized control architecture could be required.

## Chapter 4

# Experiments

### 4.1 Introduction

The different control strategies proposed in Chapter 3 based on the fibre dynamics derived in Chapter 2 are tested on a real plant in the Precision Mechatronics Laboratory (PML). A single fibre suspended mass setup has been built by Universite Libre de Bruxelles (ULB) students, in a way that allows a fast and easy replacement of the different components. This setup as well as the main equipment used for experiments are described in Section 4.2. The test results are given in Section 4.3, and a detailed interpretation of these results is discussed in Section 4.4. An important remark is that the experiments performed for this work are conducted on a system at much higher dynamic and kinematic scales than in GW detectors. Indeed, the VM vibration amplitudes in the lab are of order  $10^{-3}$  m while in aLIGO they are of order  $10^{-16}$  m [42].

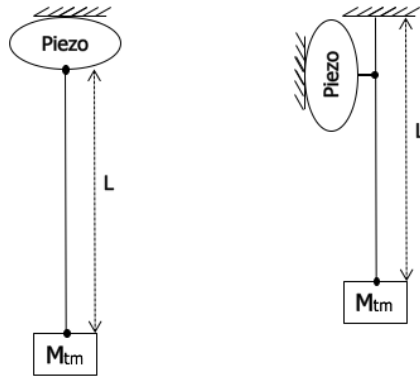


Figure 4.1 – A schematic drawing of the suspended mass and the collocated piezoelectric force sensor-actuator pair in the vertical configuration (left) and the horizontal configuration (right).

### 4.2 Experimental Setup

#### 4.2.1 Suspension arrangement

A guitar string is used (nylon or low carbon steel) as a suspension fibre, because of its elastic behaviour and relatively long ring-down times [55]. The suspended cylindrical mass of 1.456kg coming from a machining lathe is clamped to the string using a screw clamp (see Figure 4.2). The other side of the string is attached to a connecting block (clamping the fibre between two diametrically opposed screws) which on its turn is screwed on a support structure. This structure can be the vertically mounted piezoelectric transducer (see Section 4.2.2) in the case of a vertical control, or it can be another support structure in the case of a horizontal control.

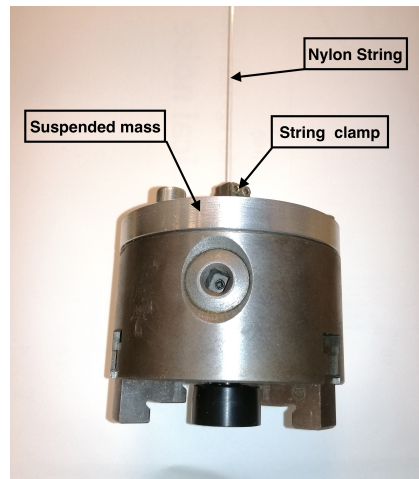


Figure 4.2 – The suspended mass of 1.456kg coming from a machining lathe spindle. It is attached to the fibre with a screw clamp.

#### 4.2.2 Collocated Piezoelectric transducer

For both the force sensor and actuator, preloaded piezoelectric stacks are used, which are integrated along the horizontal axis of a compliant elliptic stainless steel shell (see Figure 4.3), constituting an almost perfectly collocated pair. This transducer is the *APA100M* from Cedrat Technologies, being the smallest stroke and highest force version of their Amplified Piezo Actuator M series. The elliptical structure is working as a stroke amplifier (through mechanical amplification), as a pre-stressing frame and as a suspension spring (in the case of vertical control), with a resulting stroke of  $126\mu\text{m}$  and a stiffness of  $1.859\frac{\text{N}}{\mu\text{m}}$  under quasistatic excitation (from datasheet [56]). Actually, the deformation of the low voltage piezoelectric ceramics, typically MLA, along the horizontal axis (or *main* axis) can be in compression or in extension and, since the ceramics do not withstand large tensile stresses, the elliptical structure provides a preload to ensure a longer life time. In the case

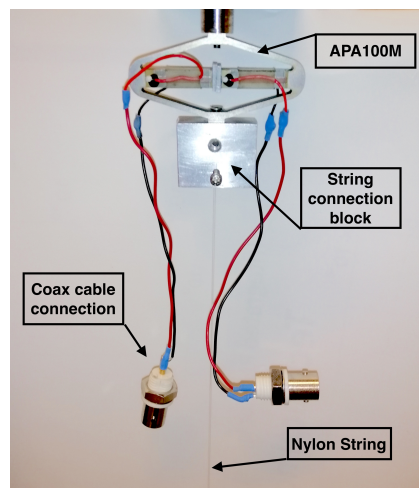


Figure 4.3 – The vertically mounted *APA 100M* piezoelectric transducer from Cedrat Technologies.

of a horizontal vibration control, the piezo is rotated  $90^\circ$  around the axis perpendicular to the main axis and the vertical axis to protect the transducer from bending loads. Moreover, the fibre is not attached directly to the transducer, but to another support structure

through the string connection block. The transducer is then attached to the string near its suspension point by clamping it between metallic washers, tightened with nuts on a screw (see Figure 4.4).

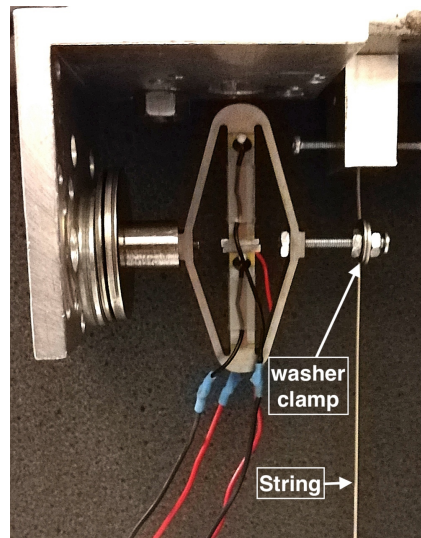


Figure 4.4 – The horizontally mounted *APA 100M* piezoelectric transducer with a clamping allowing no bending forces.

### 4.2.3 Piezoelectric Transducer Control and Data Acquisition

The *APA100M* is equipped with two coax cable connectors. Because of the symmetry of this transducer, the user can choose which side is for actuation and which side is for the measurements. The sensor side is connected to a sensor signal conditioner from *PCB Piezotronics*, which is set to voltage mode. The filtered output from this signal conditioner goes to the *MicroLabBox* prototyping unit from *dSpace*, which has ADC and a DAC modules enabling the connection with the dSpace computer software. The latter software allows to use compiled Simulink models in real time with the operating MicroLabBox. One can thus send signals in real time to the DAC and actuate the other side of the piezoelectric transducer through a voltage amplifier (piezo controller from *Thorlabs*). Using the dSpace software, it is possible to visualise different signals simultaneously (*e.g.* sensor or actuator signal) and modify some of the model parameters of the Simulink model (*e.g.* gains, constants, etc.). Consequently, the computer can also be used to generate digital controllers and apply them on the plant, thereby closing the loop. Remembering the nonlinear feedback laws, the high-pass filtering of the sensor measurements by the signal conditioner is necessary to eliminate the static tension.

### 4.2.4 Violin Mode Excitation

Guitar strings are generally excited with plectrums or fingertips (using the skin or the finger nail) and the location of the plucking force will determine the modal amplitudes (in the middle: mainly 1st mode, at 1/4th: mainly 2nd mode). An approximated solution of the fibre motion with this kind of excitation is derived in Section 2.4. These different means of excitation have a non-zero touching width, which creates a low-pass filtering effect. It may also cause the excitation to be a nonlinear and time-varying operation [55].

For steel strings, which are ferromagnetic materials, it is possible to use a magnetic coil excitation as in Section 2.4.3. In Figure 4.5, one can see a copper solenoid coming from a *AKRIBIS Voice Coil Motor AVM24-10-0.5*. A current is injected into the coil through a power amplifier (from *Micromega*) which takes as input one of the analog outputs of the Microlabbox DAC. This way, the string can be excited by a magnetic field which oscillates at twice the frequency of the injected current (see Section 2.4.3). To increase

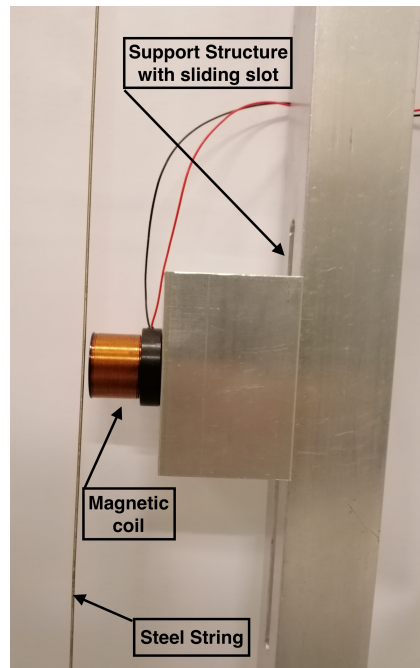


Figure 4.5 – The magnetic coil, screwed on a metallic structure with a sliding slot, allowing to choose the position of the excitation.

the magnetic flux reaching the string, a steel core is placed inside the coil. The metallic structure to which the electromagnet is attached works both as a rigid support and as a heat sink. Indeed, the resistive losses generate heat in the copper and the maximum nominal temperature is  $100^{\circ}\text{C}$  with maximum peak currents of  $3.8\text{A}$ , so that one should control the temperature. It is important to know that besides the doubled frequency and the varying inductance non-linearity predicted by the magnetic force model in Section 2.4.3, there are some additional nonlinear effects that have to be taken into account. Indeed, the magnetic flux-current characteristics of the electromagnet show some hysteresis and, more importantly, a saturation limit introducing a significant non-linearity in the relation between the input signal and the magnetic force. This effect is reduced by keeping the current in the linear range of the electromagnet.

### 4.3 Test results

The control strategies that have been detailed in Section 3.4.1 and in Section 3.4.2 for a collocated force sensor-actuator pair (vertical and horizontal mount, respectively) are tested on the real plant using the equipment described here above. Nonetheless, both approaches are implemented without dividing the control signal by the modal amplitude like in the former Section. This part describes the experiments and their results, while Section 4.4 provides a more detailed discussion.

### 4.3.1 Vertical collocated piezoelectric mount

When the string is excited by the electromagnet, one can observe the ASD shown in Figure 4.6. The first peak corresponds to the vertical (also called axial) vibrations of the string whereas the other successive peaks are associated to the VMs. The eigenfrequency of the vertical mode is given by the following formula [37]

$$\omega_v = \sqrt{\frac{EA}{ML}} \quad (4.1)$$

where  $A$  is the cross section area of the string,  $M$  is the suspension mass,  $L$  is the string length and  $E$  is the young modulus, which can be calculated from the latter expression. With regard to the open loop transfer function between the sensor and the actuator, the VMs are not visible, as expected from Chapter 3.

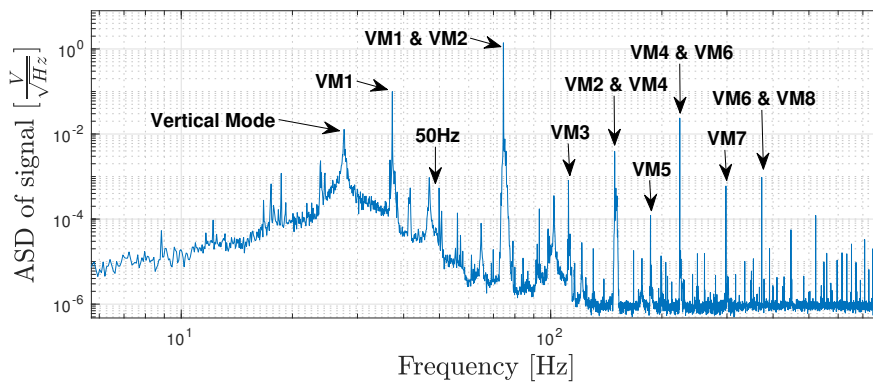


Figure 4.6 – The vertical piezoelectric sensor signal ASD for a white noise magnetic excitation. The first peak corresponds to the vertical eigenmode of the string at the frequency  $f_v = 27.5\text{Hz}$ . The following peaks are the VM harmonics, for which the fundamental frequency is  $f_1 = 37.5\text{Hz}$ .

An experiment is conducted to evaluate the effect of the phase of the stiffness control on the string vibration amplitude, like in Section 3.4.1. To do so, the electromagnet is exciting the string at its first VM frequency and the piezoelectric actuator is driven at twice that frequency, but with a relative difference of 1.11%. This difference causes a relative phase shifting over time between the two actuation signals. The sensor signal is then passed through a high order bandpass filter (whose frequency response is quasi-rectangular) to access the string amplitude through the linear observability (see Figure 4.7). On the other hand, a video camera has been placed in front of the string to record these vibrations and compare them with the piezo sensor measurements. The obtained signal coincides with the visual observations, namely a slow periodic variation of the amplitude (each period being repeated every 89sec). Looking at the relative phase difference between the modal amplitude and the piezo actuation and remembering Equations 3.20 and 3.21, one can see that the experiment agrees with the predicted optimal relative phase of  $\frac{\pi}{2}$  and  $A_u < 0$ . The word *optimal* is used to designate the situation where the vibration amplitude is minimised. On the contrary, a relative phase of  $-\frac{\pi}{2}$  causes the piezo to inject energy into the string vibrations as predicted by Equation (3.22), so that it is in fact contributing to the excitation through the parametric resonance (see Section 3.3.2). An important comment on Figure 4.7 is that after reaching the optimal relative phase, causing the vibration to be much smaller, there is a sudden increase in the vibration amplitude. This is due to the nonlinear phase

shifting effect described in Section 3.3.2, and it corresponds to the simulation results (see Figure 3.12). In Appendix B, Figure B.12a and b show the actuation and string vibration signals at a much smaller time-scale, allowing to visualise the relative phase difference and the damping effect.

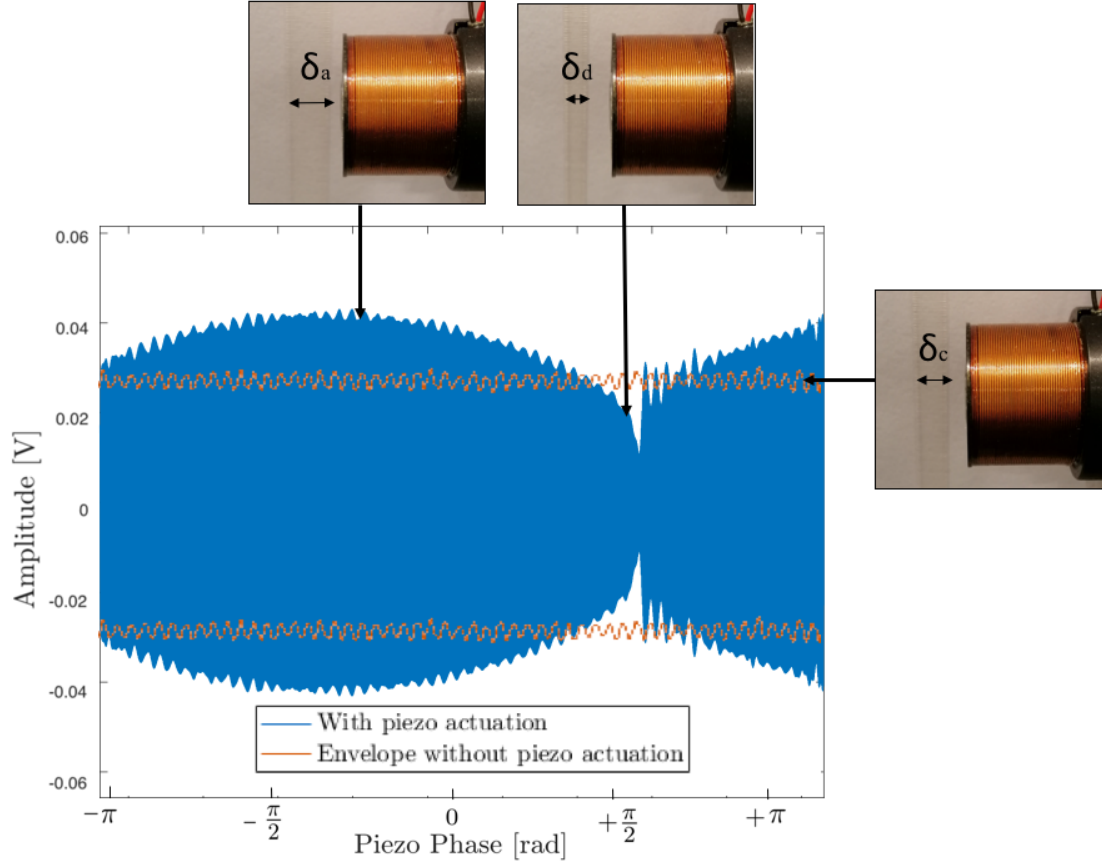


Figure 4.7 – The vertical piezoelectric sensor signal filtered around  $f_1 = 37.5\text{Hz}$  (to observe the string amplitude through the linear observability) for a sinusoidal magnetic excitation with a frequency  $f_1$  and a vertical sinusoidal excitation at  $2f_1$  by applying a voltage of  $60V_{pp}$ . The phase delay of the piezo excitation with respect to the string’s first mode motion is shifted over time, showing an optimal phase difference around  $\frac{\pi}{2}$ . The vibration amplitudes shown on the pictures are approximately  $\delta_a = 5.5\text{mm}$ ,  $\delta_d = 2.5$ ,  $\delta_c = 4\text{mm}$ .

Both IFF and derivative feedback have been implemented and a comparison can be found in Figure 4.8a and b. The string is plucked with a plectrum and the control is activated 1.5s later. The feedback gains that have been used are 0.035 and  $-19000$  for derivative feedback and IFF control respectively, which are the maximum attainable gains before reaching instability due to other modes, which will be discussed later.

A comparison between the sensor ASD with and without IFF control is depicted in Figure 4.9 and clearly shows that the vertical bouncing mode of the string is significantly attenuated, while the VMs are not, except for the first mode and the peak at the second mode frequency as a result. The next modes however do not seem to be damped.

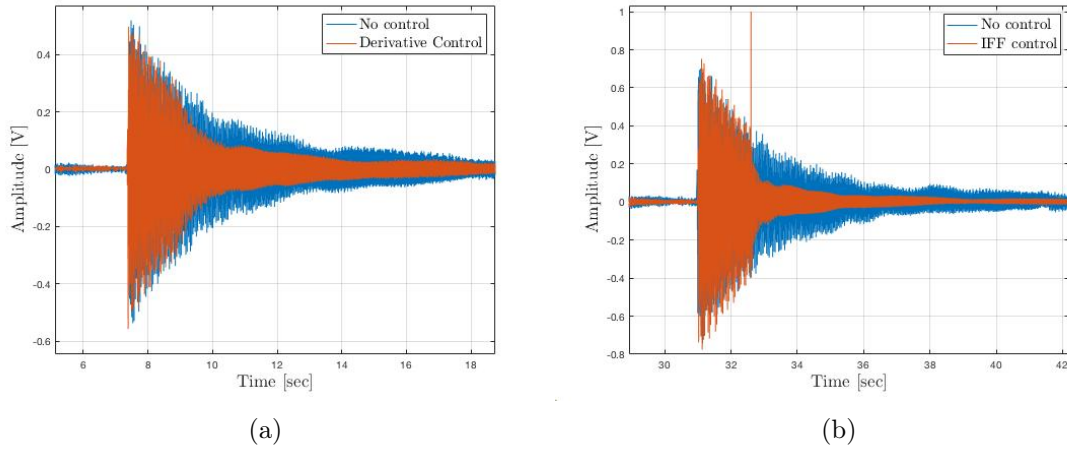


Figure 4.8 – Comparison between IFF and derivative control when activating the control approximately 1.5s after plucking the string.

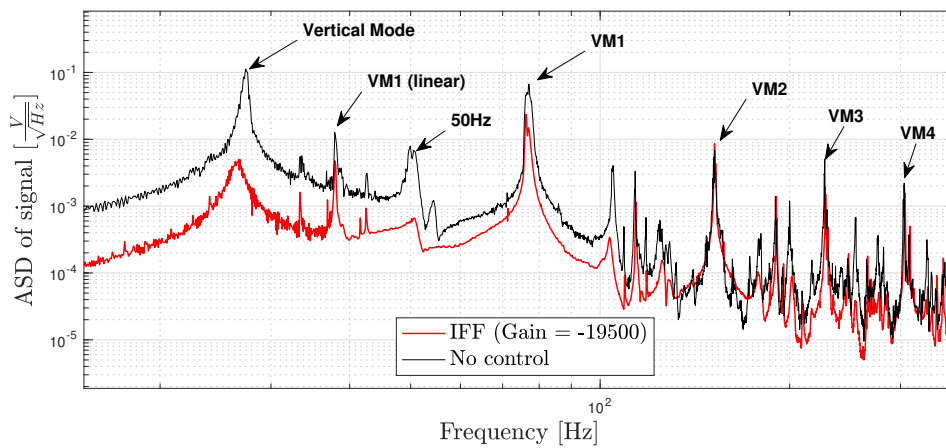


Figure 4.9 – The comparison between vertical piezoelectric sensor signal ASDs obtained with and without IFF control.

### 4.3.2 Horizontal collocated piezoelectric mount

By injecting a white noise signal in the piezoelectric actuator and simultaneously recording the sensor signal, the open loop transfer function between those two quantities can be estimated using the acquired spectral power densities. The result is shown in Figure 4.10. The increasing phase lag for higher frequencies is due to the finite sampling frequency.

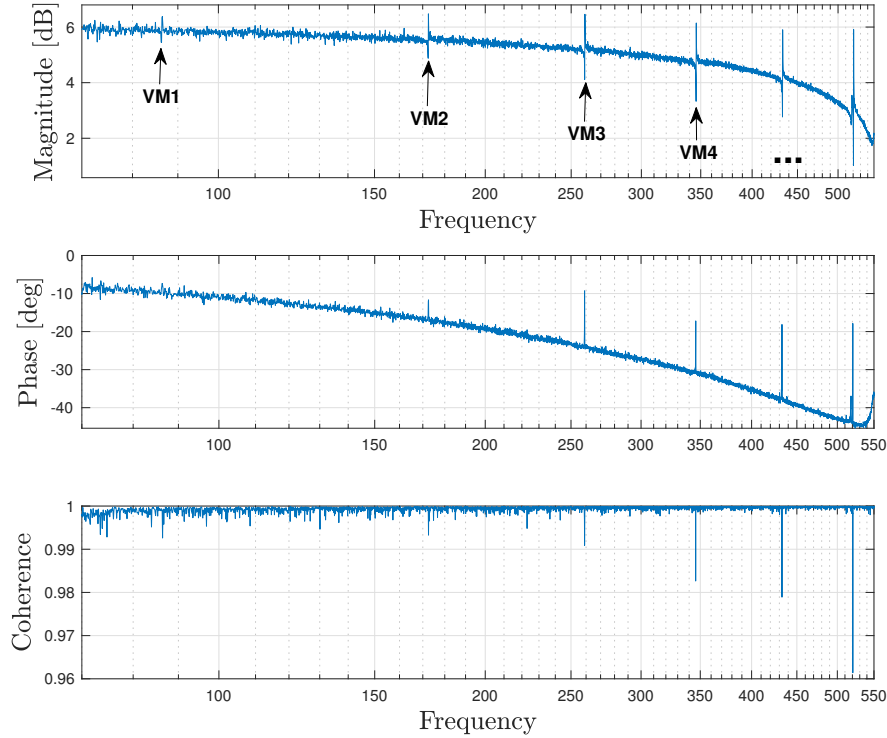


Figure 4.10 – The estimated open loop transfer function between the actuator and the sensor and the associated coherence function.

Actually, due to the ADC conversion a one to one transfer function can be written as  $H(s) = e^{-\frac{s}{f_s}}$  where  $f_s$  is the sampling frequency, so that a phase lag is introduced at higher frequencies. The decreasing amplitude is due to a vibration mode of the structure to which the collocated pair is attached. The alternating poles and zeros are associated to the VMs of the string. This specific pattern has been predicted in Section 2.2.2 from the state space representation of the string dynamics. However, the distances between the poles and their associated zeros are even smaller ( $\pm 0.2\text{Hz}$  for each mode), which indicates a very low authority on these specific modes. Another difference is the increasing response for higher mode numbers, which is due to the higher slopes of the mode shapes at the boundaries. The transfer function between the electromagnet signal and the force sensor is estimated and shown in Appendix B Figure B.13, showing a reduction of a factor 5 in the magnification of the first mode when using IFF control. For increasing mode numbers however, the reduction of the VM peaks in this transfer function is lower, as the IFF principally acts at low frequencies. The feedback gain that has been used for this experiment is  $-28000$ , which is the maximum attainable one before reaching instability due to other modes, as will be discussed later.

## 4.4 Discussion

The experimental results allow to put the mathematical representation of the fibre's physics in contrast with the reality. The similarities and the differences are discussed here in order to evaluate the relevance of the proposed solutions.

### 4.4.1 Measurement of violin modes

A first observation is that the VM vibrations can be measured by a vertically mounted force sensor, at twice their natural frequencies due to the quadratic observability. This was predicted in Section 3.2.1, thereby illustrating the significance of the dynamic tension. Nevertheless, the mathematical model assumed an ideal vertical force sensor, which is not the case in the real plant. The piezoelectric sensor has a finite sensitivity to forces in other directions (*e.g.* the vertical one), so that the transverse forces caused by VM vibrations are also measured through the bending of the transducer. Thus, the measurements show that the VMs are both observed quadratically and linearly, causing their spectral peaks to be larger at the frequencies corresponding to even mode numbers (where quadratically observed VMs are superposed with the linearly observed ones). Still, this non-ideal behaviour is useful to analyze the modal amplitudes of VMs with odd mode numbers.

With the force sensor mounted horizontally, the VM vibrations are observed linearly, as predicted in Section 3.2.2. However, in a similar way as for the vertically mounted sensor, the horizontal configuration allows to measure vertical forces through the bending of the transducer. Therefore, the vertical vibration mode of the string is measured as well.

A more direct observation of the VMs is performed by simply looking at the fibre vibrations or recording it with a camera. Even with a video camera recording only 30 frames per second, the visual data can be used to gather an approximate vibration amplitude. Actually, since the string motion has its smallest velocity when it reaches the maximal deflection (at both sides of the equilibrium position), an optical illusion is formed during steady state vibrations, as if there were two nearly parallel strings separated by a distance that is equal to twice the vibration amplitude. Using this technique, one can verify the measurements of other sensors.

By using the logarithmic decrement method as discussed in Section 3.4.1 (see Equation (3.39)), the quality factors of the string VMs have been measured to be in the range  $10^2 - 10^3$  depending on the string. This corresponds to the experiments of Carla Marcello *et al.* in [57] and is much lower than the quality factors for the silica fibres in the aLIGO suspensions ( $10^8 - 10^9$ , see Chapter 1). Nevertheless, it is still sufficient to be able to analyze the effects of the active damping strategies.

### 4.4.2 Excitation of violin modes

By exciting the string with a plectrum having a smooth surface finish, one can observe all the VM harmonics with the different sensor configurations. As discussed in Section 2.4, the response of the fibre depends on the location and the amplitude of the plucking force. However, when choosing the plucking location in the nodal point of a certain mode, that mode is observed in the ASD of the sensors. This is due to the non-zero touching width of the plectrum and the imperfection of the plucking location [55], as well as the inter-modal energy transfers, especially for large vibration amplitudes [37].

Using an electromagnet, the excitation is made nearly time invariant and its spectral content can be chosen using the convenient filtering and remembering that the injected current should have half the frequency of the desired excitation frequency. By injecting white noise into the electromagnet and recording the piezoelectric sensor signal, the transfer function between both quantities can be estimated, showing peaks at the VM frequencies. This frequency response allows to visualise the effect of an active damping strategy.

### 4.4.3 Active damping of violin modes

For the vertical mount, the experiment that shows the effect of the relative phase difference between the string vibrations and the parametric control coincides with the numerical simulations and the analytical predictions. For a harmonic oscillation of a certain VM, the optimal (read *most dissipative*) actuation for a given gain is at twice that frequency with a phase lead of  $\frac{\pi}{2}$ , while the principal parametric resonance phenomenon described in Section 3.3.1 occurs for a phase lag of  $\frac{\pi}{2}$ . This important result validates the simulations and thus the nonlinear mathematical model for the string dynamics.

However, when closing the loop using either a derivative feedback or an IFF controller, the system becomes unstable for a given feedback gain, thereby limiting the damping performances to a very low level. Actually, while the single frequency phase-shifting experiment discussed previously allowed to apply a voltage signal of  $100V_{pp}$ , the limited feedback gain causes the applied voltage to be restricted to levels generally below  $5V_{pp}$ . The reason for this is probably the phase lag induced by the ADC at high frequencies as discussed in Section 4.3.2, so that high frequency modes of the system (*e.g.* the eigenmode of the piezoelectric transducer) are excited. In fact, the bandwidth of the control system is limited since there is always some destabilization of the flexible residual modes. This phenomenon, where the total damping of the residual modes decreases when the bandwidth increases is known as spillover [8]. Despite this lack of stability, the proposed strategies are able to actively damp the string vibrations, as shown by Figure 4.8a and Figure 4.8b. It goes without saying that the string's vertical mode vibrations are strongly coupled with the vertical piezoelectric actuator and sensor, so that they are effectively damped by the implemented vibration controls. Furthermore, the nonlinear couplings between the latter vertical mode and the transverse modes of the string cause the reduction in the vertical vibrations to be reflected as a reduction in the VM vibrations, which can be understood from the string theories of Narasimha in [37]. For a material whose axial stiffness is such that the vertical mode eigenfrequency is close to one of the VMs, which is the case in the experiments for a steel wire, the latter coupling is even bigger for that distinct mode. This is why the first VM is damped much more than its harmonics in the experiments.

For the horizontal mount, the alternating pole-zero pattern in the open loop transfer function of the collocated pair that was predicted in Section 3.4.2 has been validated experimentally. Therefore, the VMs are observable and controllable in this configuration. However, the very small distance between the corresponding poles and zeros is indicative of the low active damping potential, according to [8]. Moving the collocated pair further from the attachment point could be a solution to increase these distances, but at the expense of reduced seismic isolation performances in aLIGO. Indeed, the natural frequency of the pendulum mode would be shifted to a higher value (see Figure 3.17) because of the reduced effective fibre length, so that the overall seismic noise contribution would be increased in the sensitivity of the GW detector.

## Chapter 5

# Main suspension chain vibration modes

### 5.1 Introduction

In this chapter, the main chain in the lower stages of the quadruple suspension system is modelled in order to assess the effects of violin modes on other vibration modes. Indeed, the suspended masses are rigidly attached to the fibres, causing the VMs to be observed in GW measurements. The vibration control strategies described in Chapter 3 also affects the rest of the system, enforcing the need for a model reflecting those interactions. The terminology for the different degrees of freedom can be found in Figure 5.1. For the sake

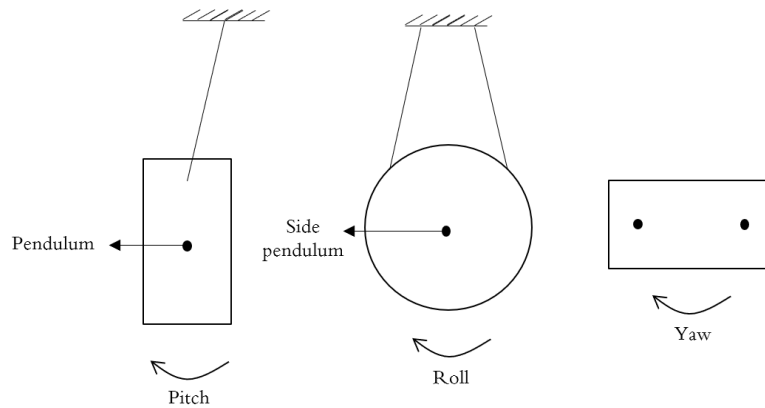


Figure 5.1 – The different degrees of freedom for a single suspension loop with different perspectives: (left) side view; (middle) front view; (right) top view.

of simplicity, this representation considers only the two lower suspension stages and only one suspension loop for the lower mass. Seismic noise and vibrations of the upper stages are not modelled here, but it can be injected through the motion of the suspension base, which would normally be one of the leaf springs.

### 5.2 Pendulum, pitch and yaw motion

The most important vibration modes in the quadruple suspensions are associated to the pendulum, pitch and yaw degrees of freedom of both masses. One can also model the roll and side pendulum motions, but even supposing they are present, their influence along the beam axes of the detector is very limited and only caused by misalignments.[33]

#### 5.2.1 Single suspended mass

The lower stage of the isolation system is simpler to model because there are less coupling terms between different DOFs. Furthermore, this part does not include fibre vibrations for the sake of simplicity. These will be included in Appendix A.4.

For the pendulum and pitch motions, consider a single suspended mass with a moving suspension point (which will later be replaced by the motion of the upper stage) a moment

of inertia  $I$  (for pitch and yaw motion) and a mass  $M$  causing a constant tension  $\frac{Mg}{2}$  in both fibres due to gravity. Omitting yaw motion, the two fibres of length  $l$  can be replaced by a single fibre of length  $L$  with a tension  $T_s = Mg$  (see Figure 5.2). The attachment point

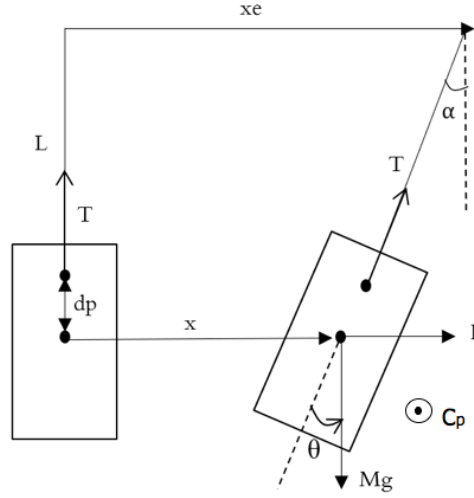


Figure 5.2 – The single suspended mass pitch and pendulum modes, with a moving suspension point.

is located at a vertical distance  $d_p$  from the centre of mass. The pendulum displacement and pitch degrees of freedom are denoted  $x$  and  $\Theta$  respectively. These motions are coupled through the following equations of motion

$$M\ddot{x} = F + T_s \sin(\alpha) \approx F + T_s \frac{x_e - x - d_p \Theta}{L} \quad (5.1)$$

$$I\ddot{\Theta} = C_p + T_s d_p \sin(\alpha - \Theta) \approx C_p + T_s d_p \frac{x_e - x - (d_p + L)\Theta}{L} \quad (5.2)$$

where  $x_e$  is the suspension displacement,  $F$  is an external horizontal force,  $C_p$  is a pitch torque and  $\alpha$  is the angle between the fibre and the vertical axis. From these differential equations, which are typical harmonic oscillators, one can derive the natural frequency for both motions by  $\omega_x = \sqrt{\frac{G_x}{M}}$  and  $\omega_\Theta = \sqrt{\frac{G_\Theta}{I}}$  where  $G_x$  and  $G_\Theta$  are the coefficients responsible for the restoring forces associated to motions  $x$  and  $\Theta$  respectively. Thus, the eigenfrequencies are given by

$$\omega_x = \sqrt{\frac{g}{L}} \quad \text{and} \quad \omega_\Theta = \sqrt{\frac{T_s d_p \frac{d_p + L}{L}}{I}} \quad (5.3)$$

For the yaw motion  $\phi$ , one has to deal with both fibres whose four attachment points are given by the distances  $d_y$  and  $db$  (see Figure 5.3) and the rotation of the suspension base is given by the angle  $\phi_e$ . This motion is decoupled from the other DOFs and is described by the following equation of motion:

$$I\ddot{\phi} = C_y + \frac{d_b}{2} \sin(\phi'_e)(F_{y1} + F_{y2}) = C_y + G_\phi(T_1 + T_2)(\phi_e - \phi) \quad (5.4)$$

where  $C_y$  is an external yaw torque,  $T_1$  and  $T_2$  are the tensions of the two fibres and the

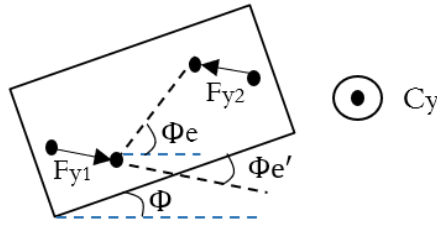


Figure 5.3 – The single suspended suspension loop yaw mode, with a rotating suspension base.

geometric constant  $G_\phi$  can be found using the triangle proportionality theorem and the Pythagorean theorem, which yield

$$G_\phi = \left(\frac{d_b}{2}\right)^2 \cdot \frac{\frac{d_y}{d_b - d_y}}{l + l \frac{d_y}{d_b - d_y}} = \frac{1}{4} \frac{d_b d_y}{l} \quad \text{where } l = \sqrt{\frac{1}{4}(d_b - d_y)^2 + L^2} \quad (5.5)$$

The proof for this can be found in Appendix A.3. In a similar manner as for Equation (5.3), the eigenfrequency for yaw is given by

$$\omega_\phi = \sqrt{\frac{G_\phi(T_1 + T_2)}{I}} \quad (5.6)$$

An extended model of the two lower stages of the suspension chain taking into account the effects of VMs and the decentralized control actuation is derived in Appendix A.4. The differential equations are translated to rather complex Simulink block diagrams, which are shown in Figure B.8, Figure B.10 and Figure B.9 (in Appendix B). The numerical simulations can be performed using the Matlab script in Appendix C.1. From this, one can analyze the effects of the parametric control on the pendulum, pitch and yaw of the two suspended masses (see for example Figure B.11 in Appendix B). Overall, the effect of the decentralized parametric control of each individual fibre on the other DOFs is desirable.

The EOM governing the dynamics of the different DOFs of the two masses have restoring force coefficients proportional to the tension. This means that there might be an opportunity for an active damping strategy using the same kind of actuators as in Chapter 3. This is discussed in Appendix A.5. Indeed, by dynamically varying the restoring force coefficients, one is again led to perform parametric control. As the eigenfrequencies of for example the pendulum motions are much lower than the VM frequencies, the control signals can *a priori* be computed separately by the respective filters and superposed to generate a single control signal for each active mount. See Appendix A.4 and Appendix A.5 for more details.

## Chapter 6

# Conclusions and Future Work

Different representations of the fibre dynamics have been discussed in this work. A linear modal model assuming fixed-end boundary conditions allows a rather simple formulation and the derivation of the eigenfrequencies of the VMs. An extended model that takes into account the dynamic tension allows to account for nonlinear hardening effects and axial force interactions at the fibre boundaries. Finally, a FE state space model of the linear transverse dynamics of the fibre has been derived, which allows to simulate a suspension fibre with a tip mass and a finite boundary stiffness.

The recommended active damping approaches are based on collocated control strategies using piezoelectric force actuation and sensing. The first method consists of an axial parametric control that dynamically changes the tension in the fibre in a way that destructively interferes with the transverse fibre vibrations. With this type of actuation, mathematically, one is led to study a damped parametrically driven Duffing oscillator. The optimal actuation force is proven to have twice the frequency of the controlled VM, with a relative phase lead of  $\frac{\pi}{2}$  with respect to the modal vibration. This is achieved using a nonlinear feedback digital controller, delivering either a negative derivative feedback or a modified IFF control. The hardening effect is included to understand the physics of the strings that are used in the lab, which are driven to vibration amplitudes of order  $10^{-3}$  m. However, the average amplitudes of the VM vibrations at aLIGO are of order  $10^{-16}$  m, so that *a priori* the cubic stretching effects can be neglected. Moreover, the non-linearity of the parametric control term in the fibre dynamics indicates a very low control authority at the aforementioned modal amplitudes for a parametric control strategy. Still, applying one of the the proposed nonlinear feedback laws allows to generate a synthetic damping that is proportional to the actuation force amplitude. The VM quality factors are estimated to be reduced from  $10^9$  to  $10^4$  for a constant actuation force with amplitude 0.1 N. Some experimental results coincide with the numerical simulations, thereby validating the optimal relative phase for the actuation signal and thus the nonlinear mathematical model for the string dynamics. The feedback gain is however limited by the finite control bandwidth on the real plant, thereby reducing the active damping performances substantially.

The second approach is based on a transverse force control close to the suspension point using classical IFF. The numerical simulations of the latter control strategy are realized with the FE state space model using Matlab. Due to the collocated actuator-sensor pair configuration, the open loop transfer function is characterized by strictly alternating poles and zeros, which allows to design an unconditionally stable vibration control using IFF. This specific pole-zero pattern has been validated experimentally in the lab, along with the linear observability of the VMs. The fact that the collocated pair is placed near the suspension point makes the distances between the corresponding poles and zeros very small, resulting in a low active damping potential. This issue was also predicted from the projection of the FE dynamic equations on the modal basis. For the same reasons as for the vertical mount, the active damping performances are significantly reduced on the real plant due to the limited feedback gain.



## Future work

The use of piezoelectric stack actuators and sensors in GW detectors is questionable, mainly due to the heat generation caused by mechanical friction losses and dielectric losses that would increase the thermal noise level and thus impair the sensitivity of the GW detector. These thermal effects are not covered by this work, which assumes perfect sensing and actuation devices. Thus, using this type of technologies would require to thermally isolate it from the rest of the system. Moreover, the amplified piezoelectric actuator has its own eigenmode, which would also be reflected in the thermal noise of the suspension according to the Equipartition Theorem. This would require to design a new type of transducer, with adequate materials that are characterised by very low mechanical and electrical losses (*e.g.* fused silica). Also, a solution should be developed to mount the collocated pair in a way that is compatible with the actual suspension design.

As mentioned previously, the experiments that have been performed in this work were conducted on a system at much higher dynamic and kinematic scales than in GW detectors. The damping due to air friction is much higher, and the materials are not the same (metals and polymers instead of ceramics). The influence of these discrepancies on the outcomes of this work should be assessed experimentally, using vacuum conditions and adequate fibre materials and dimensions.

An additional potential research topic would be to design a centralized control scheme that takes into account all DOFs of the quadruple suspension using optimization based control design methods. The nonlinear MIMO Simulink model based on the dynamic equations derived in Section 5.2.1 can be used for this in the case of a parametric control strategy. Furthermore, noise budgeting would allow to assess the sensor and actuator noise requirements, based on the sensitivity requirements of the GW detector.

# Bibliography

- [1] Abbott BP, Abbott R, Abbott Tâ, Abernathy MR, Acernese F, Ackley K, et al. Observation of Gravitational Waves from a Binary Black Hole Merger. *Physical Review Letters*. 2016 Feb;116(6). Available from: <https://link.aps.org/doi/10.1103/PhysRevLett.116.061102>.
- [2] Shapiro B, Mavalvala N, Youcef-Toumi K. Modal damping of a quadruple pendulum for advanced gravitational wave detectors. In: 2012 American Control Conference (ACC). Montreal, QC: IEEE; 2012. p. 1017–1022. Available from: <http://ieeexplore.ieee.org/document/6315185/>.
- [3] Robertson NA, Cagnoli G, Crooks DRM, Elliffe E, Faller JE, Fritschel P, et al. Quadruple suspension design for Advanced LIGO. *Classical and Quantum Gravity*. 2002 Aug;19(15):4043–4058. Available from: <http://stacks.iop.org/0264-9381/19/i=15/a=311?key=crossref.930b3fe5f9700cd586c91009697299e6>.
- [4] Abbott BP, Abernathy Mâ, Acernese F, Ackley K, Adams C, Adams T, et al. GW150914: The Advanced LIGO Detectors in the Era of First Discoveries. *Physical Review Letters*. 2016 Mar;116(13). Available from: <https://link.aps.org/doi/10.1103/PhysRevLett.116.131103>.
- [5] Gossler S. The suspension systems of the interferometric gravitational-wave detector GEO600;.
- [6] Abbott BP, Abbott R, Adhikari R, Ajith P, Allen B, Allen G, et al. LIGO: the Laser Interferometer Gravitational-Wave Observatory. *Reports on Progress in Physics*. 2009 Jul;72(7):076901. Available from: <http://stacks.iop.org/0034-4885/72/i=7/a=076901?key=crossref.669f7c34d7d28503fd7f84b53db6048f>.
- [7] Ling S. Standing Waves and Resonance; 2016. Available from: [https://phys.libretexts.org/Bookshelves/University\\_Physics/Book%3A\\_University\\_Physics\\_\(OpenStax\)/Map%3A\\_University\\_Physics\\_I\\_-\\_Mechanics%2C\\_Sound%2C\\_Oscillations%2C\\_and\\_Waves\\_\(OpenStax\)/16%3A\\_Waves/16.6%3A\\_Standing\\_Waves\\_and\\_Resonance](https://phys.libretexts.org/Bookshelves/University_Physics/Book%3A_University_Physics_(OpenStax)/Map%3A_University_Physics_I_-_Mechanics%2C_Sound%2C_Oscillations%2C_and_Waves_(OpenStax)/16%3A_Waves/16.6%3A_Standing_Waves_and_Resonance).
- [8] Preumont A. Vibration control of active structures: an introduction. 3rd ed. No. v. 179 in *Solid mechanics and its applications*. Berlin: Springer; 2011.
- [9] Lockerbie NA, Tokmakov KV. A Violin-Mode shadow sensor for interferometric gravitational wave detectors. *Measurement Science and Technology*. 2014 Dec;25(12):125110. Available from: <http://stacks.iop.org/0957-0233/25/i=12/a=125110?key=crossref.a9c528cbff82d5938ed881bf076b4725>.
- [10] Dmitriev AV, Mescheriakov SD, Tokmakov KV, Mitrofanov VP. Controllable damping of high-Q violin modes in fused silica suspension fibers. *Classical and Quantum Gravity*. 2010 Jan;27(2):025009. Available from: <http://stacks.iop.org/0264-9381/27/i=2/a=025009?key=crossref.03b72b115b03a21867cdf3ae1374f8b>.

- [11] Nayfeh AH, Mook DT. Nonlinear oscillations. Wiley classics library ed ed. Wiley classics library. New York: Wiley; 1995. OCLC: 257285431.
- [12] Mielczarek J. Gravitational waves from the big bounce. *Journal of Cosmology and Astroparticle Physics*. 2008 Nov;2008(11):011. Available from: <http://stacks.iop.org/1475-7516/2008/i=11/a=011?key=crossref.30fbb80df0494aede24e3c517a15453>.
- [13] Saulson PR. Fundamentals of interferometric gravitational wave detectors. Second edition ed. New Jersey London Singapore Beijing Shanghai Hong Kong Taipei Chennai Tokyo: World Scientific; 2017. OCLC: 986984718.
- [14] Taylor JH, Weisberg JM. A new test of general relativity - Gravitational radiation and the binary pulsar PSR 1913+16. *The Astrophysical Journal*. 1982 Feb;253:908. Available from: <http://adsabs.harvard.edu/doi/10.1086/159690>.
- [15] Abbott BP, Abbott R, Abbott TD, Abraham S, Acernese F, Ackley K, et al. GWTC-1: A Gravitational-Wave Transient Catalog of Compact Binary Mergers Observed by LIGO and Virgo during the First and Second Observing Runs;p. 48.
- [16] Saulson PR. Interferometric gravitational wave detectors. *International Journal of Modern Physics D*. 2018 May;27(07):1840001. Available from: <https://www.worldscientific.com/doi/abs/10.1142/S0218271818400011>.
- [17] Folkner W, Seidel D. Gravitational Wave Missions from LISA to Big Bang Observer. In: *Space 2005*. Long Beach, California: American Institute of Aeronautics and Astronautics; 2005. Available from: <http://arc.aiaa.org/doi/10.2514/6.2005-6711>.
- [18] Giaime J, Saha P, Shoemaker D, Sievers L. A passive vibration isolation stack for LIGO: Design, modeling, and testing. *Review of Scientific Instruments*. 1996 Jan;67(1):208-214. Available from: <http://aip.scitation.org/doi/10.1063/1.1146573>.
- [19] Coughlin M, Mukund N, Harms J, Driggers J, Adhikari R, Mitra S. Towards a first design of a Newtonian-noise cancellation system for Advanced LIGO. *Classical and Quantum Gravity*. 2016 Dec;33(24):244001. Available from: <http://stacks.iop.org/0264-9381/33/i=24/a=244001?key=crossref.baf652916e5ae42a0c3c802b9e246fe3>.
- [20] Cagnoli G, Hough J, DeBra D, Fejer MM, Gustafson E, Rowan S, et al. Damping dilution factor for a pendulum in an interferometric gravitational waves detector. *Physics Letters A*. 2000 Jul;272(1-2):39-45. Available from: <http://linkinghub.elsevier.com/retrieve/pii/S0375960100004114>.
- [21] Gonzalez G. Suspensions thermal noise in the LIGO gravitational wave detector. *Classical and Quantum Gravity*. 2000 Oct;17(21):4409-4435. Available from: <https://doi.org/10.1088%2F0264-9381%2F17%2F21%2F305>.
- [22] Harry GM, Gretarsson AM, Saulson PR, Kittelberger SE, Penn SD, Startin WJ, et al. Thermal noise in interferometric gravitational wave detectors due to dielectric optical coatings. *Classical and Quantum Gravity*. 2002 Feb;19(5):897-917. Available from: <https://doi.org/10.1088%2F0264-9381%2F19%2F5%2F305>.

- [23] Santamore DH, Levin Y. Eliminating Thermal Violin Spikes from LIGO Noise. *Physical Review D*. 2001 Jul;64(4). ArXiv: gr-qc/0101116. Available from: <http://arxiv.org/abs/gr-qc/0101116>.
- [24] Van Veggel AMA. Quasi-monolithic mirror suspensions in ground-based gravitational-wave detectors: an overview and look to the future. *Philosophical Transactions of the Royal Society A: Mathematical, Physical and Engineering Sciences*. 2018 May;376(2120):20170281. Available from: <http://rsta.royalsocietypublishing.org/lookup/doi/10.1098/rsta.2017.0281>.
- [25] Mukherjee S. Removing instrumental artifacts: Suspension violin modes. In: *AIP Conference Proceedings*. vol. 523. Pasadena, California (USA): AIP; 2000. p. 362–368. Available from: <http://aip.scitation.org/doi/abs/10.1063/1.1291880>.
- [26] Allen B, Ottewill A. Multi-taper Spectral Analysis in Gravitational Wave Data Analysis. *General Relativity and Gravitation*. 2000 Mar;32(3):385–398. Available from: <http://link.springer.com/10.1023/A:1001911930363>.
- [27] Strain K. LIGO-T050107-x0: Advanced LIGO global control and ETM suspension violin modes;. Available from: <https://dcc.ligo.org/LIGO-T050107/public>.
- [28] Robertson N. LIGO-T1800161-v1: Simple Model for Analyzing Passive Violin Mode Damping; 2018.
- [29] Gossler S, Cagnoli G, Crooks DRM, Luck H, Rowan S, Smith JR, et al. Damping and tuning of the fibre violin modes in monolithic silica suspensions. *Classical and Quantum Gravity*. 2004 Mar;21(5):S923–S933. Available from: <http://stacks.iop.org/0264-9381/21/i=5/a=082?key=crossref.01ea56816fc323601b6cd574d07a7a4c>.
- [30] Appleby R. *Oscillations and Waves: An Introduction*, by Richard Fitzpatrick: Scope: textbook. Level: undergraduate. *Contemporary Physics*. 2014 Apr;55(2):453–460. Available from: <http://www.tandfonline.com/doi/abs/10.1080/00107514.2014.881923>.
- [31] de Silva CW, editor. *Computer Techniques in Vibration*. 1st ed. CRC Press; 2016. Available from: <https://www.taylorfrancis.com/books/9781420053180>.
- [32] Barton M. LIGO-T070101-x0: Dissipation Dilution;. Available from: <https://dcc.ligo.org/LIGO-T070101/public>.
- [33] Gonzalez G. Resonances, quality factors in LIGO pendulums: a compendium of formulas;p. 6.
- [34] Kovacic I, Brennan MJ. *The Duffing Equation: Nonlinear Oscillators and Their Behaviour*;p. 390.
- [35] Ueda Y. Random phenomena resulting from non-linearity in the system described by duffing's equation. *International Journal of Non-Linear Mechanics*. 1985 Jan;20(5-6):481–491. Available from: <https://linkinghub.elsevier.com/retrieve/pii/0020746285900241>.
- [36] Carrier GF. On the non-linear vibration problem of the elastic string. *Quarterly of Applied Mathematics*. 1945 Jul;3(2):157–165. Available from: <http://www.ams.org/qam/1945-03-02/S0033-569X-1945-12351-4/>.

- [37] Narasimha R. Non-Linear vibration of an elastic string. *Journal of Sound and Vibration*. 1968 Jul;8(1):134–146. Available from: <http://linkinghub.elsevier.com/retrieve/pii/0022460X68902009>.
- [38] Gough C. The nonlinear free vibration of a damped elastic string. *The Journal of the Acoustical Society of America*. 1984 Jun;75(6):1770–1776. Available from: <http://asa.scitation.org/doi/10.1121/1.390977>.
- [39] Legge KA, Fletcher NH. Nonlinear generation of missing modes on a vibrating string. *The Journal of the Acoustical Society of America*. 1984 Jul;76(1):5–12. Available from: <http://asa.scitation.org/doi/10.1121/1.391007>.
- [40] Perov P, Johnson W, Perova-Mello N. The physics of guitar string vibrations. *American Journal of Physics*. 2016 Jan;84(1):38–43. Available from: <http://aapt.scitation.org/doi/10.1119/1.4935088>.
- [41] Lockerbie NA, Carbone L, Shapiro B, Tokmakov KV, Bell A, Strain KA. First results from the Violin-Mode tests on an advanced LIGO suspension at MIT. *Classical and Quantum Gravity*. 2011 Dec;28(24):245001. Available from: <http://stacks.iop.org/0264-9381/28/i=24/a=245001?key=crossref.207c94683f6237e0d2904f5ef8a82265>.
- [42] Raab F. LIGO-T920006-x0: Near-Thermal Excitation of Violin Modes in the Test-Mass Suspension Wires of the 40-meter Prototype Interferometer;. Available from: <https://dcc.ligo.org/LIGO-T920006/public>.
- [43] Horodinca M. A study on actuation power flow produced in an active damping system. *Mechanical Systems and Signal Processing*. 2013 Aug;39(1-2):297–315. Available from: <https://linkinghub.elsevier.com/retrieve/pii/S0888327013001064>.
- [44] Schmidt B, Ross R. Position-sensitive photodetectors made with standard silicon-planar technology. *Sensors and Actuators*. 1983 Jan;4:439–446. Available from: <https://linkinghub.elsevier.com/retrieve/pii/0250687483850550>.
- [45] Fujino Y, Susumpow T. An experimental study on active control of in-plane cable vibration by axial support motion. *Earthquake Engineering & Structural Dynamics*. 1994 Dec;23(12):1283–1297. Available from: <http://doi.wiley.com/10.1002/eqe.4290231202>.
- [46] Bossens F, Preumont A. Active tendon control of cable-stayed bridges: a large-scale demonstration. *Earthquake Engineering & Structural Dynamics*. 2001 Jul;30(7):961–979. Available from: <http://doi.wiley.com/10.1002/eqe.40>.
- [47] Sanchez NE, Nayfeh AH. Prediction of bifurcations in a parametrically excited duffing oscillator. *International Journal of Non-Linear Mechanics*. 1990 Jan;25(2-3):163–176. Available from: <https://linkinghub.elsevier.com/retrieve/pii/002074629090048E>.
- [48] Claeysen F, Letty RL, Barillot F, Sosnicki O. Amplified Piezoelectric Actuators: Static & Dynamic Applications. *Ferroelectrics*. 2007 Jun;351(1):3–14. Available from: <http://www.tandfonline.com/doi/abs/10.1080/00150190701351865>.

- [49] Zheng J, Takahashi S, Yoshikawa S, Uchino K, de Vries JWC. Heat Generation in Multilayer Piezoelectric Actuators. *Journal of the American Ceramic Society*. 1996 Dec;79(12):3193–3198. Available from: <http://doi.wiley.com/10.1111/j.1151-2916.1996.tb08095.x>.
- [50] Pritchard J, Ramesh R, Bowen CR. Time-temperature profiles of multi-layer actuators. *Sensors and Actuators A: Physical*. 2004 Sep;115(1):140–145. Available from: <https://linkinghub.elsevier.com/retrieve/pii/S0924424704002912>.
- [51] Hardtl KH. Electrical and mechanical losses in ferroelectric ceramics. *Ceramics International*. 1982 Oct;8(4):121–127. Available from: <https://linkinghub.elsevier.com/retrieve/pii/0272884282900013>.
- [52] Fujino Y, Warnitchai P, Pacheco BM. Active Stiffness Control of Cable Vibration. *Journal of Applied Mechanics*. 1993;60(4):948. Available from: <http://AppliedMechanics.asmedigitalcollection.asme.org/article.aspx?articleid=1411144>.
- [53] Chen JC. Response of large space structures with stiffness control. *Journal of Spacecraft and Rockets*. 1984 Sep;21(5):463–467. Available from: <https://arc.aiaa.org/doi/10.2514/3.25681>.
- [54] Onoda J, Sanot T, Kamiyama K. Active, Passive, and Semiactive Vibration Suppression by Stiffness Variation. *AIAA Journal*. 1992 Dec;30(12):2922–2929. Available from: <http://arc.aiaa.org/doi/10.2514/3.48978>.
- [55] Traube C, Iii JOS. Center for Computer Research in Music and Acoustics, Stanford University Electrical and Computer Engineering Department, McGill University. 2000;p. 6.
- [56] Amplified Piezo Actuators;. Available from: <https://www.cedrat-technologies.com/en/products/actuators/amplified-piezo-actuators.html>.
- [57] Carla M, Straulino S. Measurements on a guitar string as an example of a physical nonlinear driven oscillator. *American Journal of Physics*. 2017 Aug;85(8):587–595. Available from: <http://aapt.scitation.org/doi/10.1119/1.4991374>.
- [58] Tuffillaro NB. Nonlinear and chaotic string vibrations. *American Journal of Physics*. 1989 May;57(5):408–414. Available from: <http://aapt.scitation.org/doi/10.1119/1.16011>.

## Appendix A

# Mathematical Developments

### A.1 Nonlinear single mode spring model

For a given displacement  $x$  of the mass shown in Figure 2.9, the tension in both springs is given by

$$F_s = 2k \left( \sqrt{\left(\frac{L}{2}\right)^2 + x^2} - \frac{L_0}{2} \right) \quad (\text{A.1})$$

This tension, which is identical in both parts of the fibre, induces a purely horizontal restoring force on the central mass, leading to the following equation of motion

$$\begin{aligned} m\ddot{x} &= -2F_s \sin \beta \\ &= -4k \left( \sqrt{\left(\frac{L}{2}\right)^2 + x^2} - \frac{L_0}{2} \right) \frac{x}{\sqrt{\left(\frac{L}{2}\right)^2 + x^2}} \\ &= -4kx \left( 1 - \frac{L_0}{\sqrt{L^2 + 4x^2}} \right) \\ &= -4k \frac{x}{L} \left( L - \frac{L_0}{\sqrt{1 + \left(\frac{2x}{L}\right)^2}} \right) \end{aligned} \quad (\text{A.2})$$

The last step allows the expansion of  $\frac{1}{\sqrt{1 + \left(\frac{2x}{L}\right)^2}}$  in a binomial series. The expansion of  $\frac{1}{\sqrt{1 + \gamma^2}}$  where  $\gamma = \frac{2x}{L} < 1$  gives

$$\sum_{n=1}^{\infty} (-1)^n \frac{1 \cdot 3 \dots (2n-1)}{2^n n} \gamma^{2n} = 1 - \frac{1}{2}\gamma^2 + \frac{3}{8}\gamma^4 + \dots \quad (\text{A.3})$$

By neglecting terms of order higher than 2, Equation (A.2) becomes

$$m\ddot{x} \approx -4k(L - L_0) \frac{x}{L} \left( 1 + \frac{2L_0}{L - L_0} \left(\frac{x}{L}\right)^2 \right) \quad (\text{A.4})$$

In the latter equation, one can see that the non-linearity effects increase for small values of  $L - L_0$  or in other words, for small static tensions. On the other hand, large vibration amplitudes will effectively increase the dynamic tension, causing a hardening effect. This result corresponds to the one obtained by Tuffillaro *et al.* in [58].

A comparison between the exact restoring force and its approximation for different deflections is shown in Figure A.1. Defining the following quantities

$$\omega_0^2 = 4 \frac{k}{m} \frac{L - L_0}{L} \quad \mathcal{K} = \frac{2L_0}{(L - L_0)L^2} \quad (\text{A.5})$$

Equation (A.4) reduces to

$$\ddot{x} + \omega_0^2 x (1 + \mathcal{K}x^2) = 0 \quad (\text{A.6})$$

To model loss mechanisms such as air resistance or internal friction, one can add some

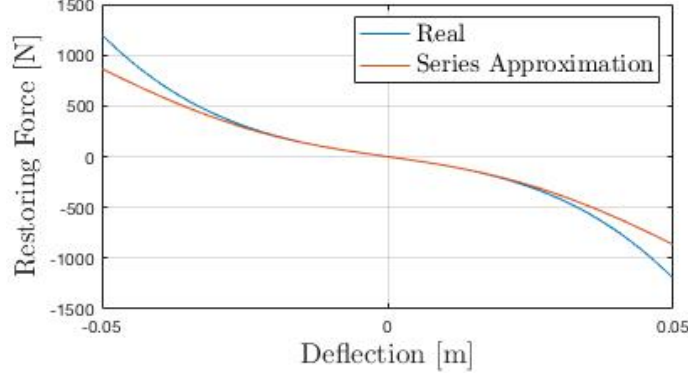


Figure A.1 – The restoring force - deflection characteristic of the spring system in Figure 2.9 for  $k = 10 \frac{kN}{m}$ ,  $L = 0.1m$  and  $L_0 = 0.08m$  given by Equation (A.2) (blue line) and the approximate expression defined by Equation (A.4) (red line).

linear viscous damping  $\lambda$  and, adding a forced harmonic acceleration term  $f(\omega t)$ , the considered nonlinear second order differential equation becomes

$$\ddot{x} + \lambda \dot{x} + \omega_0^2 x (1 + \mathcal{K}x^2) = f(\omega t) \quad (\text{A.7})$$

## A.2 Energy production

The proof for Equation (3.22) in Section 3.4.1 can be written as follows

$$E_{p,u} = \int_0^{\frac{2\pi}{\omega_{d,n}}} \left( -\frac{1}{\rho} \left( \frac{n\pi}{L} \right)^2 F_u q_n \right) \dot{q}_n dt \quad (\text{A.8})$$

combining all the constants in a single one as

$$C_t = \left( \frac{n\pi\omega_{d,n}}{L\rho} \right) A_u |q_n|^2$$

so that

$$E_{p,u} = -C_t \int_0^{\frac{2\pi}{\omega_{d,n}}} [\cos(\omega_{d,n}t) \cos(2\omega_{d,n}t + \phi_u) \sin(\omega_{d,n}t)] dt \quad (\text{A.9})$$

in which

$$\begin{aligned} \cos(\omega_{d,n}t) \cos(2\omega_{d,n}t + \phi_u) &= \cos(\omega_{d,n}t) [\cos(2\omega_{d,n}t) \cos(\phi_u) - \sin(2\omega_{d,n}t) \sin(\phi_u)] \\ &= \cos(\omega_{d,n}t) [(2 \cos^2(\omega_{d,n}t) - 1) \cos(\phi_u) - 2 \sin(\omega_{d,n}t) \cos(\omega_{d,n}t) \sin(\phi_u)] \\ &= 2 \cos^3(\omega_{d,n}t) \cos(\phi_u) - \cos(\omega_{d,n}t) \cos(\phi_u) - 2 \cos^2(\omega_{d,n}t) \sin(\omega_{d,n}t) \sin(\phi_u) \end{aligned} \quad (\text{A.10})$$

Substituting Equation (A.10) in Equation (A.9) yields

$$E_{p,u} = -C_t \frac{\pi}{2\omega_{d,n}} \sin(\phi_u) \quad (\text{A.11})$$

which is what was to be demonstrated.

### A.3 Yaw motion geometric constant

The geometric constant  $G_\phi$  introduced in Equation (5.4) (see Section 5.2.1) can be understood as follows. The yaw motion is described by the following equation of motion:

$$I\ddot{\phi} = C_y + \frac{d_b}{2} \sin(\phi'_e)(F_{y1} + F_{y2}) \quad (\text{A.12})$$

in which  $\phi'_e = \phi_e \frac{d_y}{d_b - d_y}$  and  $F_{y1} = T_1 \sin(\alpha)$  where  $\alpha$  is the angle between the fibre and the vertical axis (parallel to the gravity, see Figure A.2). One can write

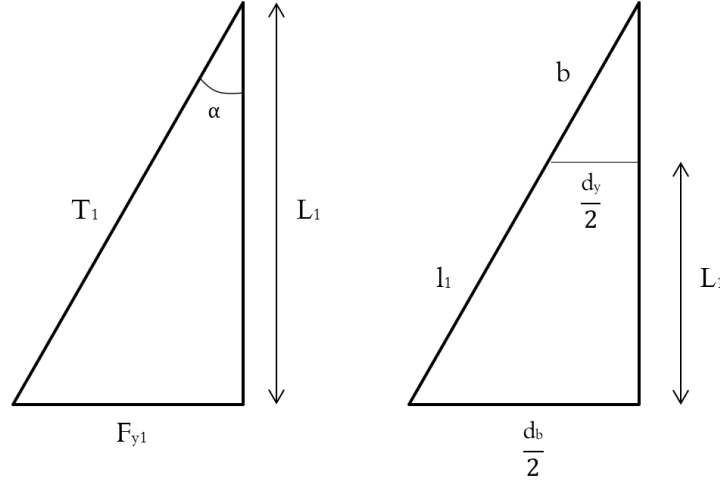


Figure A.2 – The schematic diagram linking the forces on the test mass with geometric constants.

$$\sin(\alpha) = \frac{d_b}{2} \frac{1}{l_1 + b} \quad (\text{A.13})$$

Using the triangle proportionality theorem gives

$$\frac{l_1}{\frac{d_b}{2} - \frac{d_y}{2}} = \frac{b}{\frac{d_y}{2}}$$

so that

$$l_1 + b = \sqrt{\left(\frac{d_b}{2} - \frac{d_y}{2}\right)^2 + L_1^2} \left(1 + \frac{d_y}{d_b - d_y}\right) \quad \text{and} \quad l_1 = \sqrt{\left(\frac{d_b}{2} - \frac{d_y}{2}\right)^2 + L_1^2} \quad (\text{A.14})$$

From this, Equation (A.12) becomes

$$I\ddot{\phi} = C_y + G_\phi(T_1 + T_2)(\phi_e - \phi) \quad (\text{A.15})$$

where

$$G_\phi = \left(\frac{d_b}{2}\right)^2 \cdot \frac{\frac{d_y}{d_b - d_y}}{l + l \frac{d_y}{d_b - d_y}} = \frac{1}{4} \frac{d_b d_y}{l} \quad \text{where } l = \sqrt{\frac{1}{4}(d_b - d_y)^2 + L^2} \quad (\text{A.16})$$

## A.4 Complete suspension model with vibrating fibres

The single suspension loop system described by Equations 5.1, 5.2 and 5.4 will now be completed with an additional isolation stage and with violin mode vibrations. For the lower mass, the base motion previously given by  $x_e$  and  $\phi_e$  will now be replaced by the motion of the upper mass. The definitions of all the quantities used in the next derivations are given in Figure A.3. For each fibre, the transverse force exerted on the mass is approximated

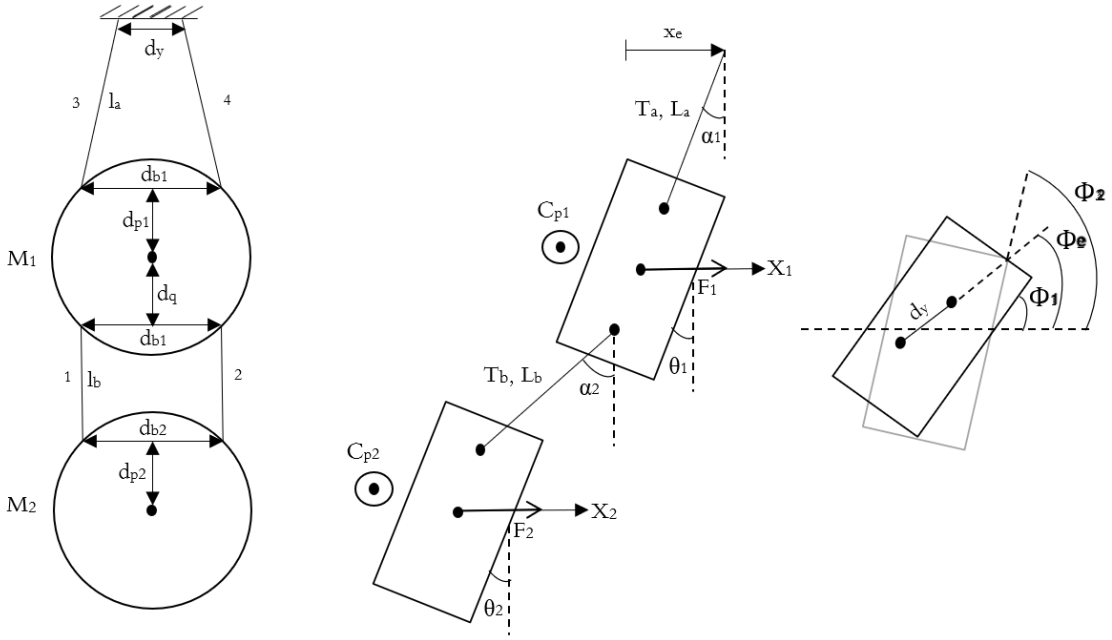


Figure A.3 – The different degrees of freedom for a two-stage isolation system and the definition of the attachment points of the fibres.

by using the instantaneous shape of the fibre near the attachment point and its tension. Indeed, the transverse force exerted by a fibre  $i$  with a tension  $T_i$ , mode shape  $\phi_{n,i}(z)$  and modal amplitude  $q_{n,i}(t)$  at  $z = z^*$  is given by

$$q_{n,i}(t)T_i \left( \frac{d\phi_{n,i}(z)}{dz} \right)_{z=z^*} \quad (\text{A.17})$$

For even mode numbers  $n$ , the forces at the two extremes of the fibre are opposite while for odd mode numbers, they are equal. This can be understood from Equation (2.44). For the following calculations, the transverse forces associated to odd and even mode numbers and  $q_n(t) > 0$  are defined as positive (in the  $x$  direction) at the upper endpoint for all fibres (see Figure A.4). This is important to state as it gives a direction to the positive planar vibration of the different fibres, potentially having different phases and amplitudes. Moreover, the tensions of the different fibres will also include dynamic tension and parametric control, so their instantaneous values will be used. The equations of motion for the lower mass are similar to those derived in Section 5.2.1 but completed with forces and toques using

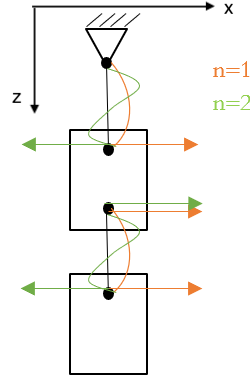


Figure A.4 – The directions of the forces exerted by the VMs at the attachment points for even and odd mode numbers.

Equation (A.17). For the coupled pendulum and pitch DOFs, the motion is described by

$$\begin{aligned} \text{Pendulum: } M_2 \ddot{x}_2 &= F_2 + (T_1 + T_2) \frac{x_1 - x_2 - d_{p2} \Theta_2}{L_b} \\ &+ \frac{n\pi}{L_b} (q_{n,1} T_1 + q_{n,2} T_2) (-1)^{n+1} \end{aligned} \quad (\text{A.18})$$

$$\begin{aligned} \text{Pitch: } I_2 \ddot{\Theta}_2 &= C_{p2} + (T_1 + T_2) \frac{d_{p2}}{L_b} [x_1 - x_2 - (d_{p2} + L_b) \Theta_2 - d_q \Theta_1] \\ &+ \frac{d_{p2} n \pi}{L_b} (q_{n,1} T_1 + q_{n,2} T_2) (-1)^{n+1} \end{aligned} \quad (\text{A.19})$$

For the yaw motion, excitations due to fibre vibrations are a result of a difference in phase and/or amplitude of fibres 1 and 2. Therefore, the yaw torque is a function of the difference between transverse fibre forces, leading to

$$\text{Yaw: } I_2 \ddot{\phi}_2 = C_{y2} + G_{\phi,2} (T_1 + T_2) (\phi_1 - \phi_2) + \frac{d_{b2} n \pi}{2L_b} (q_{n,1} T_1 - q_{n,2} T_2) (-1)^{n+1} \quad (\text{A.20})$$

in which, in a similar way as for Equation (5.5)

$$G_{\phi,2} = \frac{1}{4} \frac{d_{b2} d'_{b1}}{l_b} \quad \text{where } l_b = \sqrt{\frac{1}{4} (d_{b2} - d'_{b1})^2 + L_b^2} \quad (\text{A.21})$$

The motion of the upper mass is coupled to the motion of the lower mass, the suspension base motion and the fibre vibrations, leading to somewhat more complicated equations. Note that only the transverse forces associated to the upper fibres are negative for positive modal amplitudes. The equations of motion for the upper mass become:

$$\begin{aligned} \text{Pendulum: } M_1 \ddot{x}_1 &= F_1 + (T_3 + T_4) \frac{x_e - x_1 - d_{p1} \Theta_1}{L_a} - (T_1 + T_2) \frac{x_1 - x_2 - d_{p2} \Theta_2}{L_b} \\ &+ \frac{n\pi}{L_a} (q_{n,3} T_3 + q_{n,4} T_4) (-1)^{n+1} + \frac{n\pi}{L_b} (q_{n,1} T_1 + q_{n,2} T_2) \end{aligned} \quad (\text{A.22})$$

$$\begin{aligned}
\textbf{Pitch: } I_1 \ddot{\Theta}_1 &= C_{p1} + (T_3 + T_4) \frac{d_{p1}}{L_a} [x_e - x_1 - (d_{p1} + L_a) \Theta_1] \\
&+ (T_1 + T_2) \frac{d_q}{L_b} [x_1 - x_2 - (d_q + L_b) \Theta_1 - d_{p2} \Theta_2] \\
&+ \frac{d_{p1} n \pi}{L_a} (q_{n,3} T_3 + q_{n,4} T_4) (-1)^{n+1} + \frac{d_q n \pi}{L_b} (q_{n,1} T_1 + q_{n,2} T_2) \quad (\text{A.23})
\end{aligned}$$

$$\begin{aligned}
\textbf{Yaw: } I_1 \ddot{\phi}_1 &= C_{y1} + G_{\phi,1} (T_3 + T_4) (\phi_e - \phi_1) + G'_{\phi,1} (T_1 + T_2) (\phi_2 - \phi_1) \\
&+ \frac{d_{b2} n \pi}{2L_b} (q_{n,1} T_1 - q_{n,2} T_2) (-1)^{n+1} \quad (\text{A.24})
\end{aligned}$$

in which

$$G_{\phi,1} = \frac{1}{4} \frac{d_{b1} d_y}{l_a} \quad \text{with} \quad l_a = \sqrt{\frac{1}{4} (d_{b1} - d_y)^2 + L_a^2} \quad (\text{A.25})$$

$$G'_{\phi,1} = G_{\phi,2} \quad (\text{A.26})$$

All the EOM derived here above assume no damping. Nonetheless, the pitch motion for example loses energy due to the friction with the surrounding dilute gas and due to the local bending of the fibres near the attachment points, also generating losses. Actually, the aLIGO quadruple suspensions are designed such that these losses are minimised to reduce thermal noise as explained in Section 1.4, so that disregarding damping effects should be satisfactory for this work. It is also important to mention that due to the presence of four fibres at lower mass, differences in tension in front and back fibres will lead to pitching moments.

One can also see that, because of the varying coefficients appearing in the EOM, the latter system is parametrically excited through the different fibre tensions for all the DOFs. This means that there might be an opportunity for an active damping strategy using the same kind of actuators as in Chapter 3.

## A.5 Potential Multi-DOF Motion Damping

The method that is currently used to actively damp the different DOFs in the quadruple suspension is detailed by Shapiro *et al.* [2]. Considering constant fibre tensions, the system is described linearly by

$$M \ddot{\vec{x}} + K \vec{x} = \vec{P} \quad (\text{A.27})$$

in which  $\vec{x}$  is the state vector describing the kinematics of the different masses,  $M$  is the mass matrix,  $K$  is the stiffness matrix and  $\vec{P}$  is the external force vector. As seen in Section 1.3, the actuation is performed through the reaction chain using Optical Sensor Electro-Magnet (OSEM)s for the three upper stages and an electrostatic drive for the lower mass. Defining  $\Phi$  as the basis of eigenvectors of the system containing the  $N$  mode shapes

$$\Phi = [\phi_1 \ \phi_2 \ \dots \ \phi_N] \quad (\text{A.28})$$

one can then transform Equation (A.27) into a decoupled system of modal states  $\vec{q}$  by projecting the state vector  $\vec{x}$  into the eigenvector basis as follows:

$$\vec{x} = \Phi \vec{q} \quad (\text{A.29})$$

$$M\Phi\ddot{\vec{q}} + K\Phi\vec{q} = \vec{P} \quad (\text{A.30})$$

Left multiplication of the latter equation by  $\Phi^T$  yields

$$M_m\ddot{\vec{q}} + K_m\vec{q} = \vec{P}_m \quad (\text{A.31})$$

where  $M_m$  is the diagonal modal mass matrix and  $K_m$  is the diagonal modal stiffness matrix. The resulting  $N$  equations are decoupled. This modal decomposition allows to control all the modes that are taken into account in the model individually, as shown in Figure A.5. Since only the upper stage motion of the main chain is measured (see Sec-

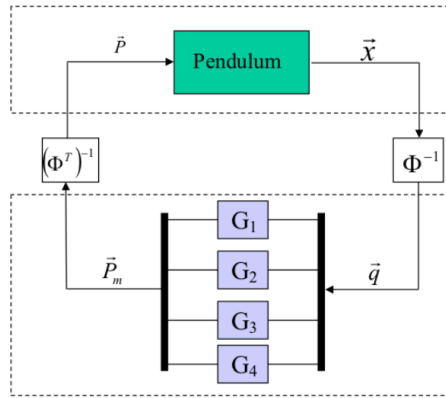


Figure A.5 – Schematic diagram of a modal control loop from [2]. The state  $\vec{x}$  is transformed into modal signals  $\vec{q}$  and passed through the respective control filters. The resulting modal forces  $\vec{P}_m$  are then transformed into real forces  $\vec{P}$  that are applied to the real system.

tion 1.3), the controller requires a good mathematical representation of the pendulum to estimate the state vector  $\vec{x}$ . Thus, in Figure A.5 the state should be thought of as a reconstructed estimated state  $\hat{\vec{x}}$ . The optimal linear feedback control law is determined using a constrained optimisation algorithm based on the standard Linear-Quadratic Regulator (LQR) technique. The word *optimal* is here used to express a minimisation of the state energy taking into account the actuation constraints, depending on the definition of the convex objective function.

Unfortunately, if one thinks of an active damping strategy based the same kind of actuators as in Chapter 3, it is impossible to apply the latter approach mainly due to the nonlinear form of the control terms. Indeed, the control would be performed through the varying coefficients in the different EOM. Consider for example the simultaneous active damping of the yaw motion of the lower mass and its suspension fibres' VMs. Since the natural frequency of the yaw mode is much lower than the VMs frequencies, one can think of superposing both control signals and injecting them into the actuator without causing mutual excitation. It is thus convenient to treat both controls independently. Neglecting vibrations caused by VMs and any external horizontal force, one can rewrite

Equation (A.20) as

$$I_2 \ddot{\phi}_2 = G_{\phi,2}(T_1 + T_2)(\phi_1 - \phi_2) \quad (\text{A.32})$$

in which one can assume that  $T_1 + T_2 \approx M_2g + 2F_u$  if both fibres are actuated with the same control force  $F_u$ . From this, it is possible to follow the same approach as in Section 3.4.1. Assuming a periodic motion  $\phi_1 - \phi_2 = A_\phi \cos(\omega_\phi t)$  and a control force  $F_u = A_u \cos(2\omega_\phi t + \phi_u)$ , it is possible to find the phase and amplitude of  $F_u$  that provides the maximum damping. The energy production for the yaw motion due to  $F_u$  is

$$\begin{aligned} E_{p,u}^\phi &= \int_0^{\frac{2\pi}{\omega_\phi}} \left[ 2G_{\phi,2}F_u(\phi_1 - \phi_2) \frac{d(\phi_1 - \phi_2)}{dt} \right] dt \\ &= -\pi G_{\phi,2} A_u A_\phi^2 \sin(\phi_u) \end{aligned} \quad (\text{A.33})$$

and the equivalent added viscous damping is

$$\xi_{a,n}^\phi = \frac{G_{\phi,2}}{2\omega_\phi^2} A_u \sin(\phi_u) \quad (\text{A.34})$$

which is maximum for  $\phi_u = \frac{\pi}{2}$ . The same idea can be followed for the other modes of the suspension chain.

# Appendix B

## Additional Figures

### B.1 Simulink models

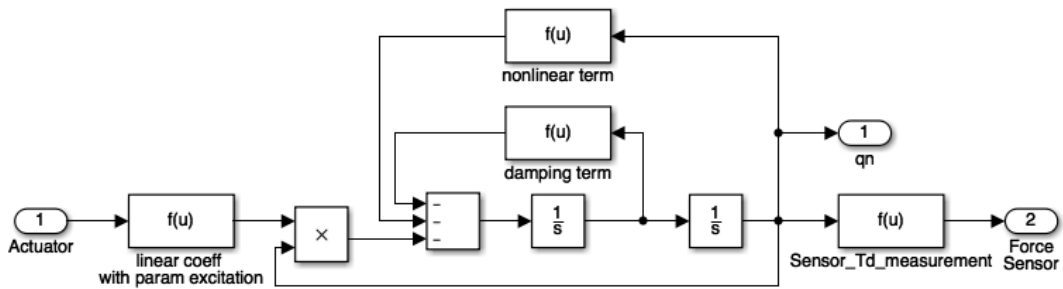


Figure B.1 – The simulink fibre subsystem, taking the actuator force as input and both the dynamic tension and the modal amplitude as outputs.

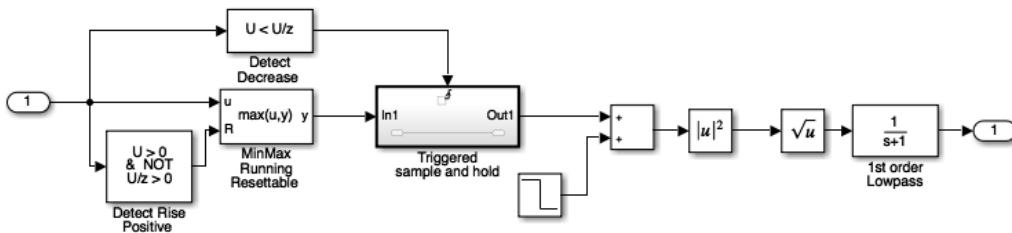


Figure B.2 – The custom made amplitude estimator block diagram.

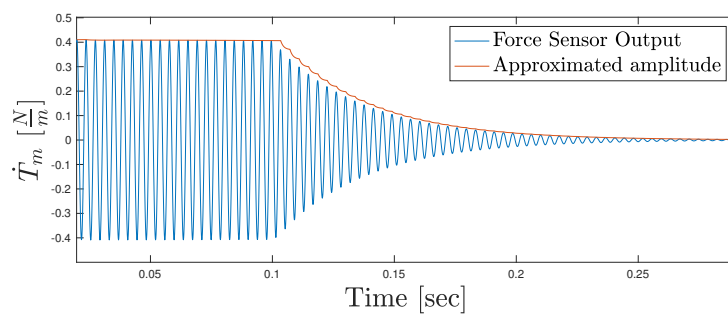


Figure B.3 – The tension amplitude estimator input (blue) and output (red).

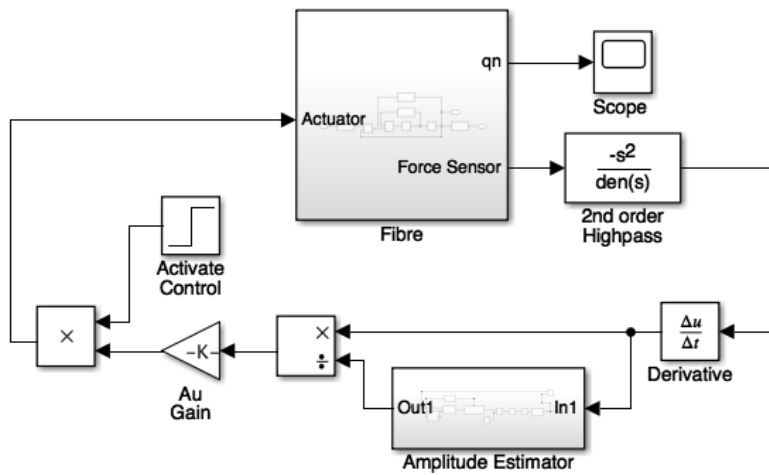


Figure B.4 – The Simulink derivative control block diagram with amplitude estimation.

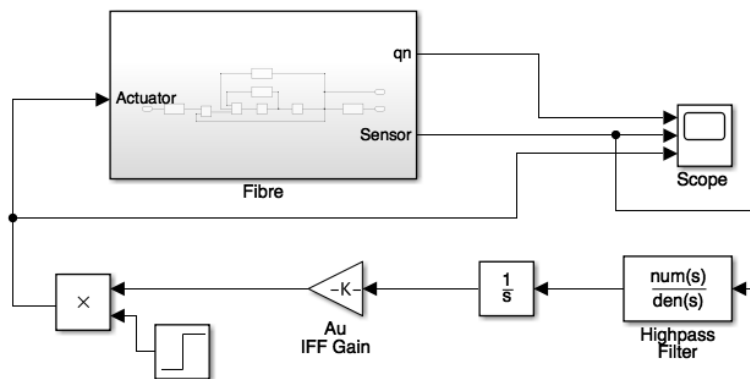


Figure B.5 – The Simulink IFF control block diagram.

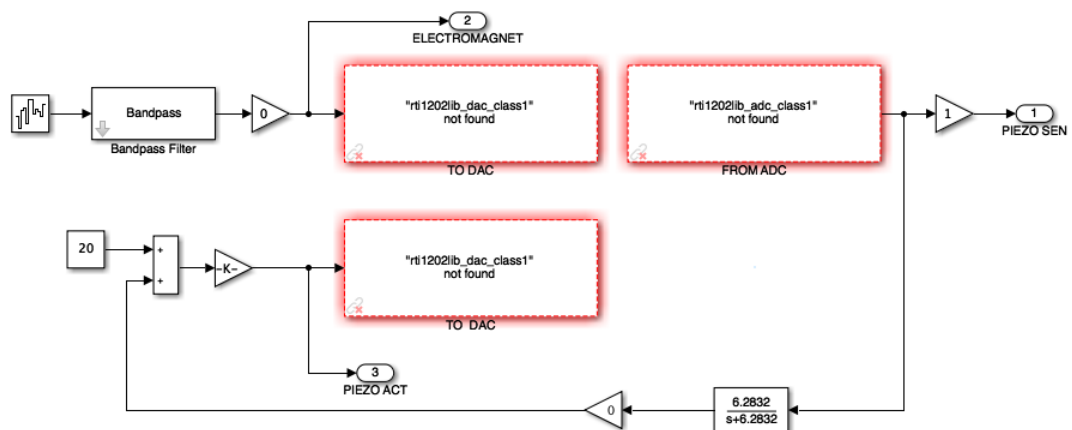


Figure B.6 – Simulink model used with dSpace for electromagnet excitation and IFF control.

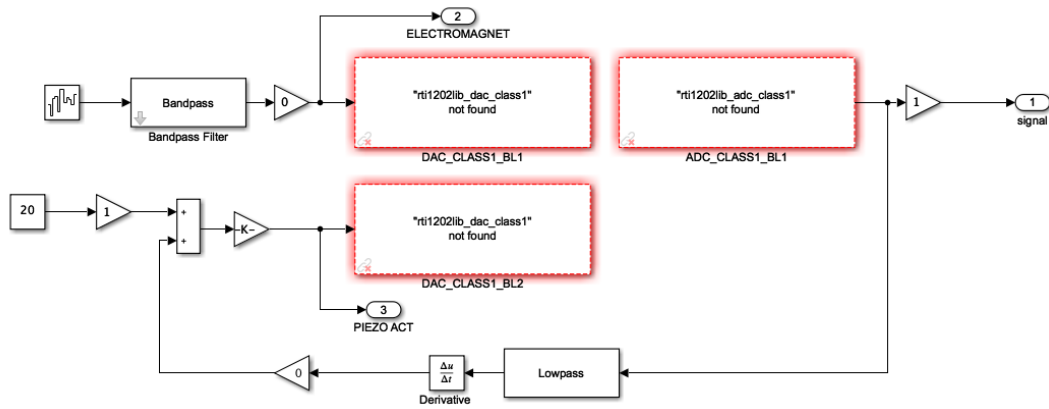


Figure B.7 – Simulink model used with dSpace for electromagnet excitation and derivative feedback control.

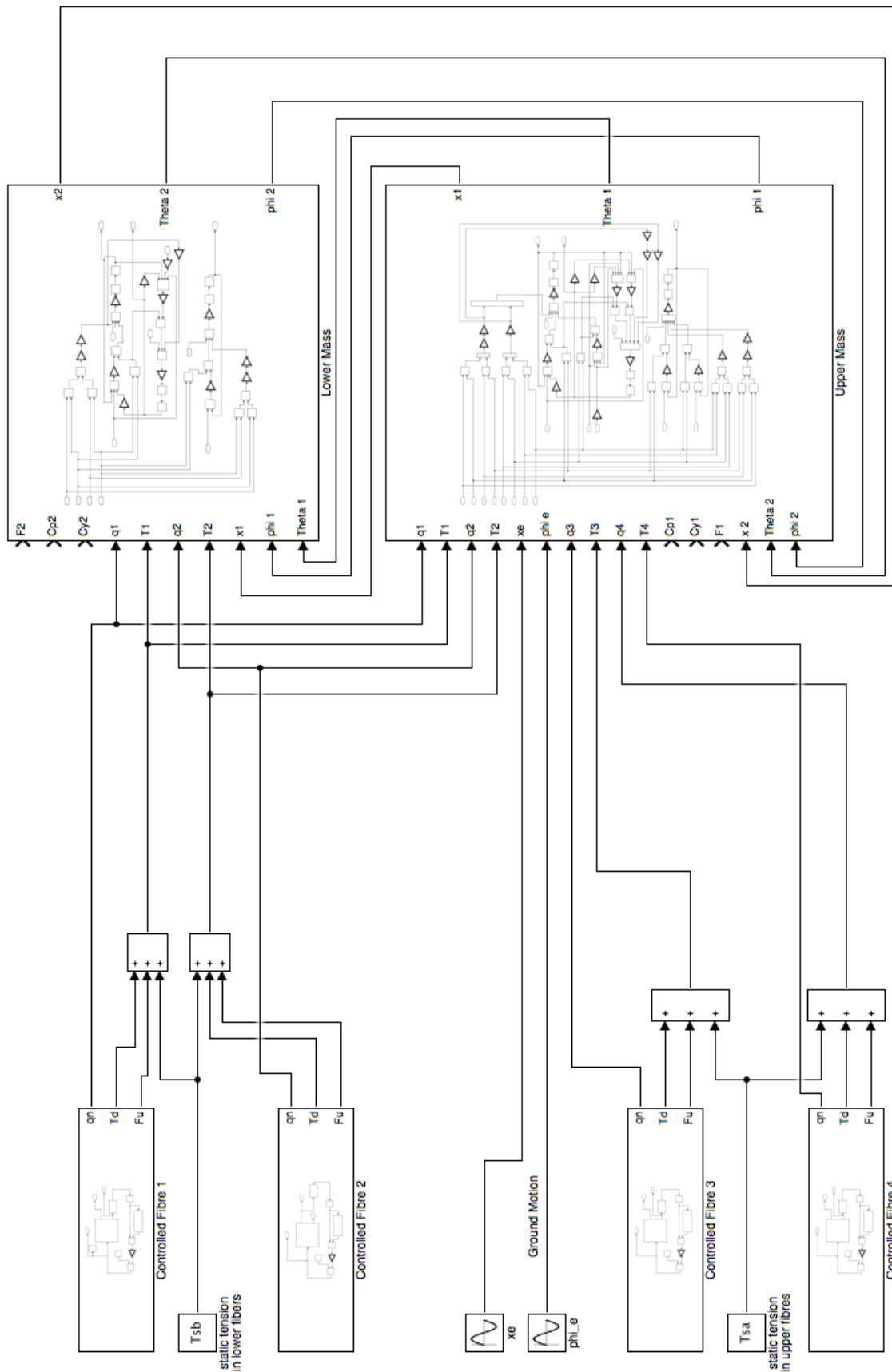


Figure B.8 – The Simulink model of the quadruple suspension, taking into account the dynamic tension and the forces exerted at the fibre boundaries due to VM vibrations. This model also includes the decentralized parametric control of VMs.

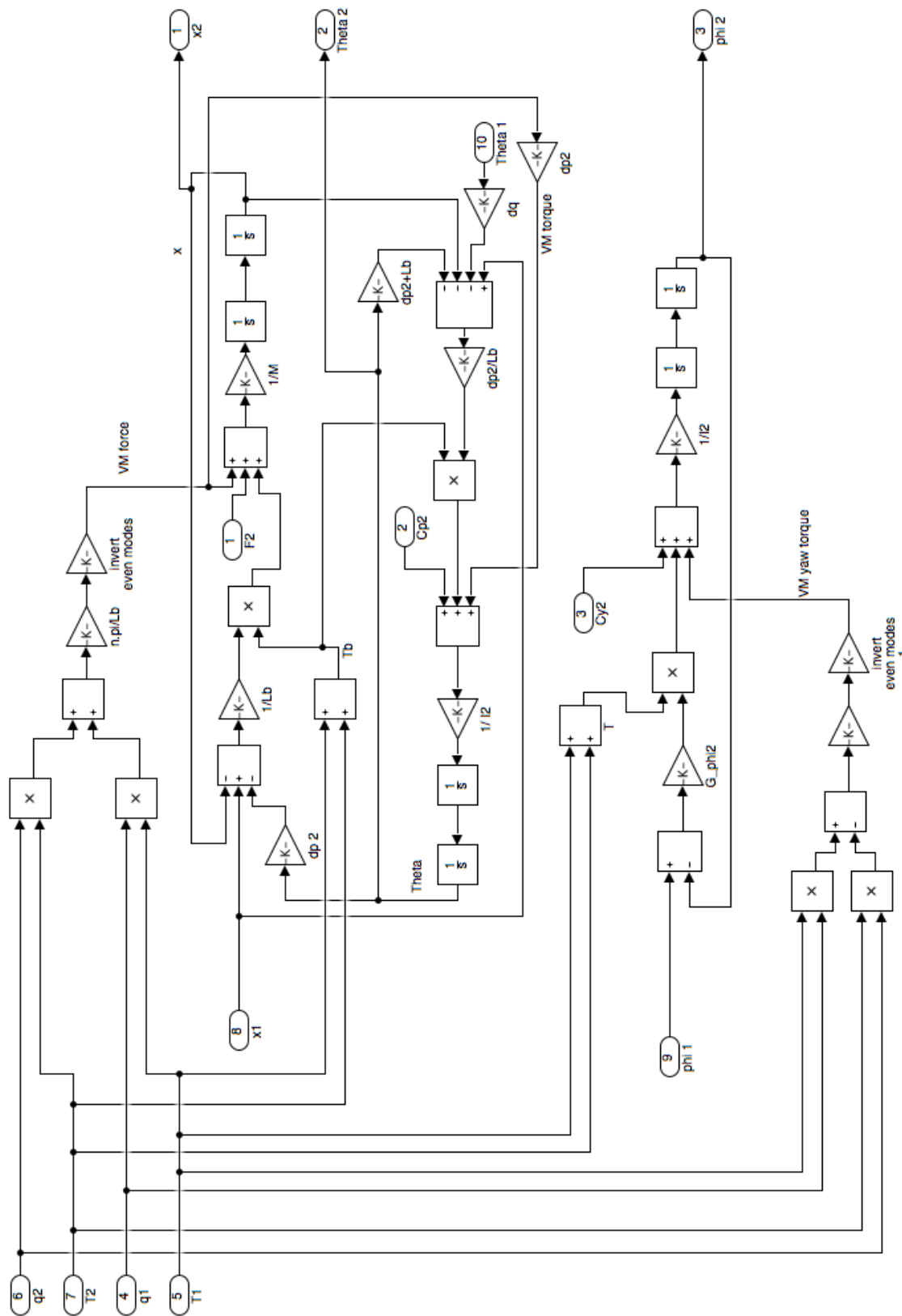


Figure B.9 – The Simulink model of the lower mass in the quadruple suspension shown in Figure B.8.

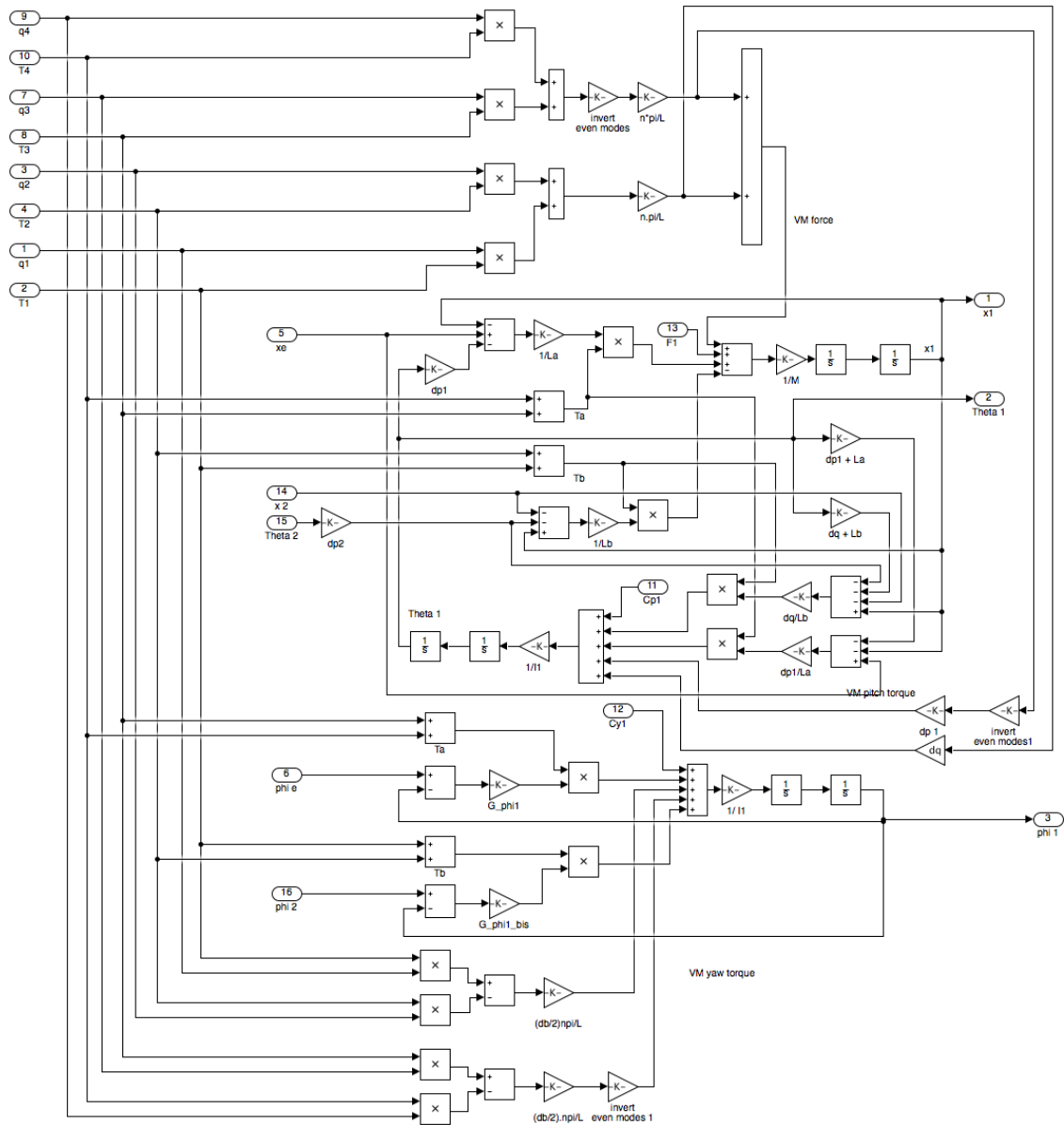


Figure B.10 – The Simulink model of the upper mass in the quadruple suspension shown in Figure B.8.



## B.2 Simulations

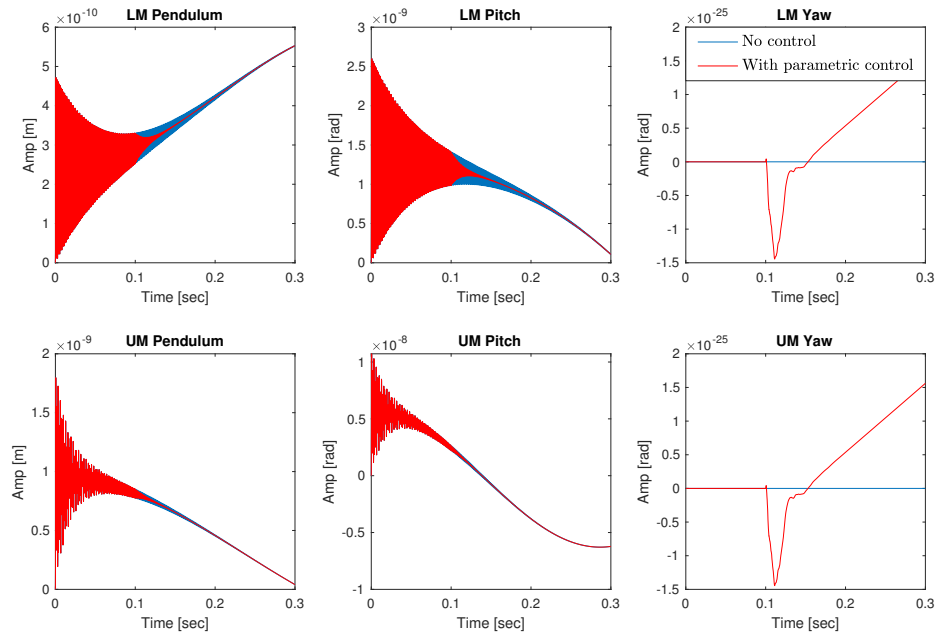
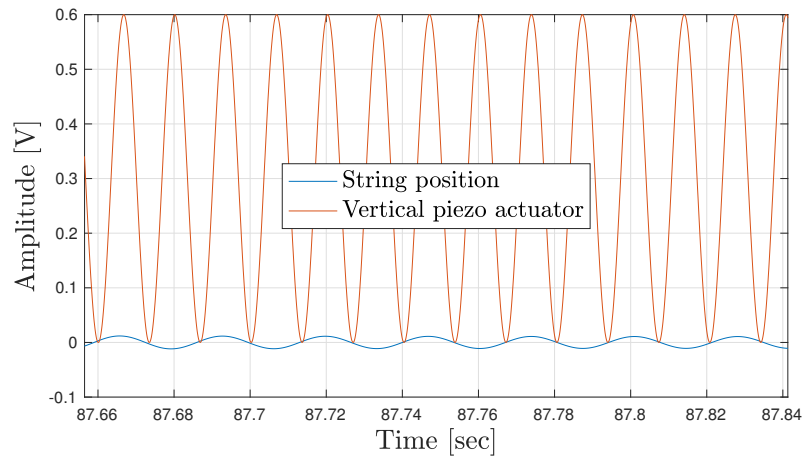
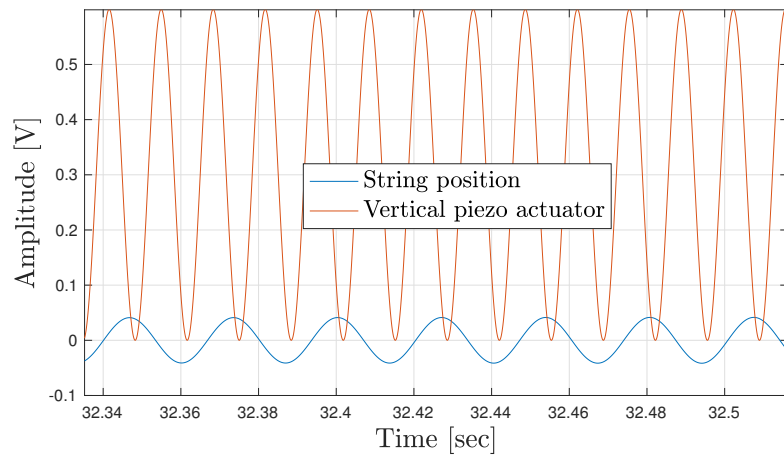


Figure B.11 – The upper mass (UM) and lower mass (LM) pendulum, pitch and yaw evolution with and without decentralized parametric control on each suspension fibre.

### B.3 Measurements



(a)



(b)

Figure B.12 – The recorded string position signal and vertical parametric control signal for a relative phase difference of (a)  $\phi_u = \frac{\pi}{2}$  for a damping effect and (b)  $\phi_u = -\frac{\pi}{2}$  for an amplifying effect.

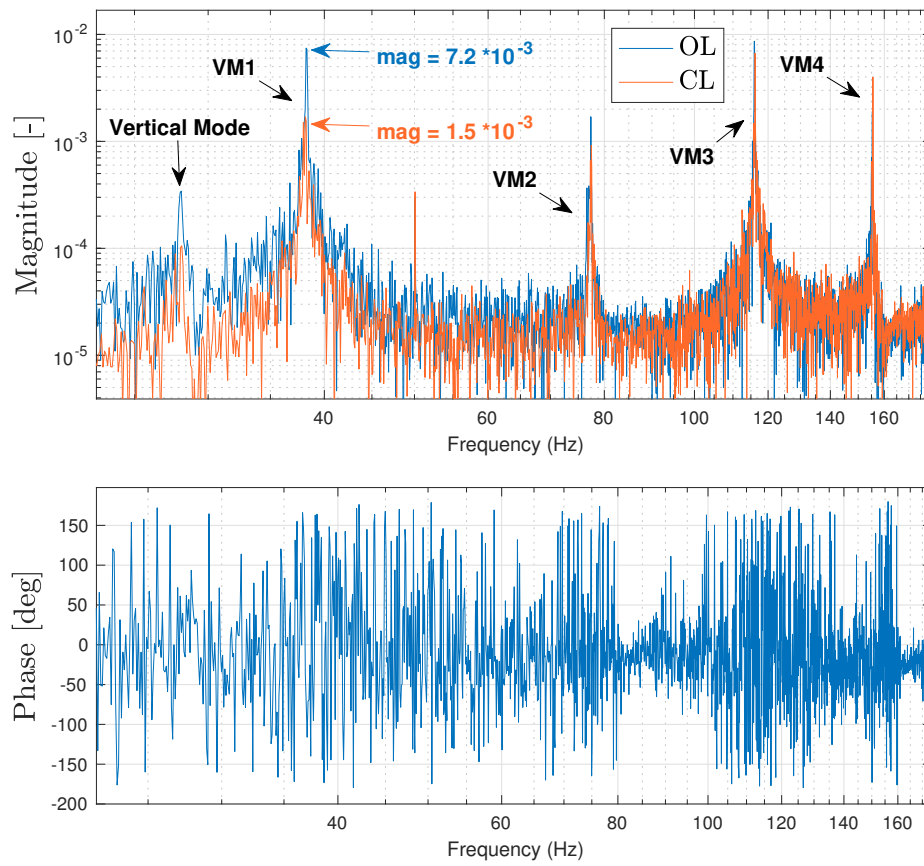


Figure B.13 – The estimated transfer function between the electromagnet signal and the force sensor with and without IFF control.

## Appendix C

# Matlab scripts

### C.1 Fibre parameters Matlab code

```
1 Tsample = 0.0001; % Simulation step size
2 Tsim = 0.3; % Simulation time
3
4 Fu_opt_contr = -50;
5 IFF_gain = 1000000;
6
7 % initial fibre positions [m]
8 q01 = 0.0001;
9 q02 = -0.0001;
10 q03 = 0.0003;
11 q04 = 0.0002;
12
13 % Mirrors:
14 % For advanced LIGO: 34 cm diameter, 20 cm thickness, and 40 kg
    mass
15 M1 = 40; % Upper mass
16 M2 = 40; % Lower mass
17 R1 = 0.16; % Radius
18 H1 = 0.2; % mirror thickness
19 I1 = M1*(3*R1^3+H1^2)/12; % =Iy = Iz (pitch and yaw)
20 R2 = 0.16; % Radius
21 H2 = 0.2; % mirror thickness
22 I2 = M1*(3*R2^3+H2^2)/12; % =Iy = Iz (pitch and yaw)
23
24 % fibres:
25 % For advanced LIGO silica: length 60cm, density = 2200kg/m3 ,
26 %diameter = 0.36mm, young modulus = 70 GPa.
27 g = 9.81; % Gravity
28 Tsa = g*(M1+M2)/2; % static tension in upper fibres [N]
29 Tsb = g*M2/2; % static tension in lower fibres
30 La = 0.60; % effective pendulum length in upper fibres [m]
31 Lb = 0.60; % effective pendulum length in upper fibres
32 A = pi*0.000190^2; % cross section [m^2]
33 E = 70E9; % Young modulus [Pa]
34 rho = 2200*A; % Linear density [kg/m^3]
35 n = 1; % Mode number
36 ksi = 0.00001; % Damping ratio
37
38 % Geometry of attachments (see schematic diagram for definitions)
```

```

39 % (Units: meters)
40 dy = 0.0013;
41 dq = 0.026;
42 db1 = 0.04;
43 db1_bis = 0.04;
44 db2 = 0.04;
45 dp1 = 0.026;
46 dp2 = 0.024;
47
48 % Other geometric constants:
49 la = sqrt((db1/2 - dy/2)^2+La^2); % length of upper fibres [m]
50 lb = sqrt((db2/2 - db1_bis/2)^2+Lb^2); % length of lower fibres [
    m]
51 G_phi1 = (1/4)*db1*dy/la;
52 G_phi2 = (1/4)*db2*db1_bis/lb;
53 G_phi1_bis = G_phi2;
54
55 % Expected eigenfrequencies [Hz]
56 fx1 = sqrt(2*Tsa/La + 2*Tsb/Lb)/(2*pi) % Upper mass Pendulum
57 fx2 = sqrt(g/Lb)/(2*pi) % Lower mass Pendulum
58 fp1 = sqrt((2*Tsa*dp1*(dp1+La)/La + 2*Tsb*dq*(dq+Lb)/Lb)/I1)/(2*
    pi) % Upper mass Pitch
59 fp2 = sqrt((2*Tsb*dp2*(dp2+Lb)/Lb)/I2)/(2*pi) % Lower mass Pitch
60 fy1 = sqrt((2*Tsa*G_phi1 + 2*Tsb*G_phi1_bis)/I1)/(2*pi) % Upper
    mass yaw
61 %fy1 = sqrt((2*Tsa*G_phi1 + 2*Tsb*G_phi1_bis)/I)/(2*pi)
62
63 % Violin Modes
64 wna = sqrt(Tsa/rho)*n*pi/La; % upper fibres
65 fna = wna/(2*pi) % [Hz]
66 wnb = sqrt(Tsb/rho)*n*pi/Lb; % lower fibres
67 fnb = wnb/(2*pi) % [Hz]
68
69 %highpass filter cutoff
70 wca = wna/2;
71 wcb = wnb/2;
72
73
74 %% Launch Simulink Model
75 sim('Total_controlled')
76 t = ScopeData.time;
77 X2 = ScopeData.signals(1);
78 T2 = ScopeData.signals(2);
79 Y2 = ScopeData.signals(3);
80 X1 = ScopeData.signals(4);
81 T1 = ScopeData.signals(5);
82 Y1 = ScopeData.signals(6);

```

```
83
84 figure;
85 subplot(2,3,1)
86 plot(ScopeData.time, X2.values)
87 title('LM Pendulum')
88 xlabel('Time [sec]')
89 ylabel('Amp [m]')
90 subplot(2,3,2)
91 plot(ScopeData.time, T2.values)
92 title('LM Pitch')
93 xlabel('Time [sec]')
94 ylabel('Amp [rad]')
95 subplot(2,3,3)
96 plot(ScopeData.time, Y2.values)
97 title('LM Yaw')
98 xlabel('Time [sec]')
99 ylabel('Amp [rad]')
100 subplot(2,3,4)
101 plot(ScopeData.time, X1.values)
102 title('UM Pendulum')
103 xlabel('Time [sec]')
104 ylabel('Amp [m]')
105 subplot(2,3,5)
106 plot(ScopeData.time, T1.values)
107 title('UM Pitch')
108 xlabel('Time [sec]')
109 ylabel('Amp [rad]')
110 subplot(2,3,6)
111 plot(ScopeData.time, Y2.values)
112 title('UM Yaw')
113 xlabel('Time [sec]')
114 ylabel('Amp [rad]')
115
116 Fu_opt_contr = 0;
117
118 sim('Total_controlled')
119
120 t = ScopeData.time;
121 X2 = ScopeData.signals(1);
122 T2 = ScopeData.signals(2);
123 Y2 = ScopeData.signals(3);
124 X1 = ScopeData.signals(4);
125 T1 = ScopeData.signals(5);
126 Y1 = ScopeData.signals(6);
127
128 figure;
129 subplot(2,3,1)
```

```

130 plot(ScopeData.time, X2.values)
131 title('LM Pendulum')
132 xlabel('Time [sec]')
133 ylabel('Amp [m]')
134 subplot(2,3,2)
135 plot(ScopeData.time, T2.values)
136 title('LM Pitch')
137 xlabel('Time [sec]')
138 ylabel('Amp [rad]')
139 subplot(2,3,3)
140 plot(ScopeData.time, Y2.values)
141 title('LM Yaw')
142 xlabel('Time [sec]')
143 ylabel('Amp [rad]')
144 subplot(2,3,4)
145 plot(ScopeData.time, X1.values)
146 title('UM Pendulum')
147 xlabel('Time [sec]')
148 ylabel('Amp [m]')
149 subplot(2,3,5)
150 plot(ScopeData.time, T1.values)
151 title('UM Pitch')
152 xlabel('Time [sec]')
153 ylabel('Amp [rad]')
154 subplot(2,3,6)
155 plot(ScopeData.time, Y2.values)
156 title('UM Yaw')
157 xlabel('Time [sec]')
158 ylabel('Amp [rad]')

```

## C.2 FE simulations in the time domain

```

1 % Single Fibre FE SS model: Time simulations
2 %-----
3 close all
4 clear all
5 % Parameters
6 L = 0.7; % Effective pendulum fibre length [m]
7 Lp = 0.02; % Collocated pair position
8
9 % Number of lumped masses
10 N = 35; % (the more, the better, but exploding complexity)
11 Np = round(Lp*N/L); % location of piezo
12
13 kp = 1.857*10^6; % Piezo stiffness [N/m]
14 Mtm = 1; % kg
15 T = Mtm*9.81; % Tension N
16 CS = pi*(0.0003^2); % Fibre cross section area [m^2]

```

```

17 rho = 8960*CS; % mass/unit length [kg/m]
18 m = rho*L/N; %Lumped mass
19 k = N*T/L; % Lumped stiffness
20 w0 = sqrt(k/m);
21
22 % FE SS (lumped masses)
23 R = zeros(N); R(Np,Np) = 1; %R(1,1) =1; R(round(N/2),round(N/2))
    =1 ; % External force @ middle
24 K = diag(repmat(2,N,1)); K(1,1) = 1e10; % Stiffness matrix
25 for i = 1:N
26     if(i>1)
27         K(i,i-1) = -1;
28     end
29     if(i<N)
30         K(i,i+1) = -1;
31     end
32 end
33 K = k*K; K(Np,Np) = 2*k + kp ; K(N,N) = k;
34
35 M = m*eye(N);
36 M(N,N) = Mtm;
37
38 A = [zeros(N) -M\K; eye(N) zeros(N)];
39 B = [M\R; zeros(N)];
40 C = zeros(2,2*N); C(1,N+Np)=-kp;C(2,2*N-1)=k;C(2,2*N)=-k;
41 D = zeros(2,N); D(1,Np) = 1;
42
43 model_ss = idss(A,B,C,D,'Ts',0); % state X = [ydot ; y]
44
45 %% Simulation
46
47 % Inject gaussian white noise?
48 %—> https://www.mathworks.com/examples/sysid/mw/ident-
    ex03319182-
49 %     simulate-a-continuous-time-state-space-model
50
51 Ts = 0.0005; % Sample time [sec]
52 Tsim = 10; % Length of simulation [sec]
53 n = Tsim/Ts; % nbr of data points
54
55 % Force input at boundaries
56 force_amp = 0.1;
57 force_Freq_Band = [50,500]*2*Ts; % convert to fraction of Nyquist
    Freq.
58 if force_Freq_Band(2)>1
59     force_Freq_Band(2) = 1;
60 end

```

```

61 u = idinput([n,N], 'RGS', force_Freq_Band, [-force_amp, force_amp]);
    %,[1,1,1]); % 'SINE' or 'rbs'=binary or 'rgs'=white gaussian
62 %u(n/4 +1:n,:) = zeros(n*3/4,N); % Zero input from the middle of
    the period
63 figure
64 plot(u(:,Np))% Only plot channels 1 and N, the relevant ones
65 legend('Force in middle')
66 title('Force input')
67
68 % Sinusoidal force:
69 % wu = 10*2*pi; % freq of input force
70 % t = 0:Tsim/n:Tsim-Tsim/n;
71 % u = sin(wu*t);% + 0.1*randn(size(u));
72 % u = repmat(u,N,1);
73
74
75 %Create iddata object
76 data = iddata([],u,Ts);
77 %figure
78 %plot(u(:,[1,N]))% Only plot channels 1 and N, te relevant ones
79 % data = iddata([],u);
80 % data.ts = 0.1;
81 %opt = simOptions('AddNoise',true);
82
83 % Simulate
84 y = sim(model_ss, data);%, opt);
85
86 figure
87 plot(y)
88 title('Reaction forces at the boundaries')
89
90 %% Plot evolution of position in the middle of the string:
91 % Now the output of the system is the N/2 'th position state —>
    C & D change
92 p = 3; % Number of point positions you want to plot
93 C2 = zeros(p,2*N);
94 for i = 1:p
95     C2(i,N+Np+i) = 1;
96 end
97 D2 = zeros(p,N);
98 model_middle_position = idss(A,B,C2,D2,'Ts',0);
99
100 % Simulate
101 y2 = sim(model_middle_position, data);%, opt);
102
103 figure
104 plot(y2)

```

```

105 title('Position of the middle of the string')
106
107 %% Plot shape of the string at a given time:
108 %%Now the output of the system is the state itself
109
110 t1 = n/4; % Desired start time
111
112 C3 = zeros(N,2*N); C3(:,N+1:2*N) = eye(N);
113
114 D3 = zeros(N,N);
115 model_middle_position = idss(A,B,C3,D3,'Ts',0);
116
117 y3 = sim(model_middle_position,data);%,opt);
118 y3 = y3.OutputData;
119
120 figure
121 hold on
122 for j = 0:3
123     shape = [];
124     for i = 1:N
125         shape = [shape y3(t1+j,i)];
126     end
127     plot([1:N]*L/N,shape)
128 end
129 xlabel('Position [m]','interpreter','latex','fontsize',17)
130 ylabel('Deflection [m]','interpreter','latex','fontsize',17)
131 legend('t_1$','t_2$','t_3$','t_4$','interpreter','latex','
        fontsize',15)
132
133 title('Shape of the wire at consecutive timesteps')
134
135 ff = sqrt(T/rho)/((0.4/5)*2*pi);
136
137 %% Power spectral density of input forces
138 x = u(:,[1]);
139 Fs = 1/Ts;
140 t = 0:1/Fs:1-1/Fs;
141 N2 = length(x);
142 xdft = fft(x);
143 xdft = xdft(1:N2/2+1);
144 psdx = (1/(Fs*N2)) * abs(xdft).^2;
145 psdx(2:end-1) = 2*psdx(2:end-1);
146 freq = 0:Fs/length(x):Fs/2;
147
148 figure
149 plot(freq,10*log10(psdx))
150 grid on

```

```

151 %title('Periodogram Of Input Forces Using FFT')
152 xlabel('Frequency [Hz]', 'interpreter', 'latex', 'fontsize', 17)
153 ylabel('Power/Frequency [ $\frac{\text{dB}}{\text{Hz}}$ ]', 'interpreter', 'latex',
        , 'fontsize', 17)
154
155 %% Power spectral density of bead position
156 x = y3(:,N/2);
157 Fs = 1/Ts;
158 t = 0:1/Fs:1-1/Fs;
159 N2 = length(x);
160 xdft = fft(x);
161 xdft = xdft(1:N2/2+1);
162 psdx = (1/(Fs*N2)) * abs(xdft).^2;
163 psdx(2:end-1) = 2*psdx(2:end-1);
164 freq = 0:Fs/length(x):Fs/2;
165
166 figure
167 plot(freq,10*log10(psdx))
168 grid on
169 %title('Periodogram Of a bead position (in the middle) Using FFT
        ')
170 xlabel('Frequency [Hz]', 'interpreter', 'latex', 'fontsize', 17)
171 ylabel('Power/Frequency [ $\frac{\text{dB}}{\text{Hz}}$ ]', 'interpreter', 'latex',
        , 'fontsize', 17)
172
173 %% Expected resonance peaks
174 Exp_Freq = [1:6]*sqrt(T/rho)/(2*L)

```

### C.3 Integral Force Feedback design

```

1 % Single Fibre FE SS model: Control design
2 %-----
3 close all
4 clear all
5
6 % Parameters
7 L = 0.7; % Effective pendulum fibre length [m]
8 Lp = 0.02; % Collocated pair position
9
10 % Number of lumped masses
11 N = 35; % (the more, the better, but exploding complexity)
12 Np = round(Lp*N/L); % location of piezo
13
14 kp = 1.857*10^6; % Piezo stiffness [N/m]
15 Mtm = 1.456; % kg
16 T = Mtm*9.81; % Tension N
17 CS = pi*(0.000215^2); % Fibre cross section area [m^2]
18 rho = 9280*CS; % mass/unit length [kg/m]

```

```

19 VM1 = 1/(2*L)*sqrt(T/rho)
20 m = rho*L/N; %Lumped mass
21 k = N*T/L; % Lumped stiffness
22 w0 = sqrt(k/m);
23
24 % FE SS (lumped masses)
25 R = eye(N); %R(1,1) =1; R(round(N/2),round(N/2)) =1 ; % External
    force @ middle
26 K = diag(repmat(2,N,1)); K(1,1) = k; % Stiffness matrix
27 for i = 1:N
28     if(i>1)
29         K(i,i-1) = -1;
30     end
31     if(i<N)
32         K(i,i+1) = -1;
33     end
34 end
35 K = k*K; K(Np,Np) = 2*k + kp ; K(N,N) = k;
36
37 M = m*eye(N);
38 M(N,N) = Mtm;
39
40 A = [zeros(N) -M\K; eye(N) zeros(N)];
41 B = [M\R; zeros(N)];
42 C = zeros(2,2*N); C(1,N+Np)=-kp;C(2,2*N-1)=k;C(2,2*N)=-k;
43 D = zeros(2,N); D(1,Np) = 1;
44
45 sys = ss(A,B,C,D); % state X = [ydot ; y]
46
47 % Open Loop TF SEN/ACT
48 load('opts.mat')
49 opts.PhaseWrapping = 'on';
50 figure; bodeplot(sys(1,Np)*k,'r',opts)
51
52 % Apply IFF control
53 FB_gain = -1000000;
54
55 Integrator_TF = tf([1],[1 0]);
56 IFF_compensator = FB_gain*zpk(Integrator_TF);
57
58 CL = feedback(sys,IFF_compensator,Np,1);
59
60 % Closed Loop TF SEN/ACT
61 hold on; bodeplot(k*CL(1,Np),'k—',opts);
62 legend('OL','CL','interpreter','latex','fontsize',15);
63 title('')
64 ylabel('Phase','interpreter','latex','fontsize',17)

```

```

65 ylabel('Magnitude','interpreter','latex','fontsize',17)
66 xlabel('Frequency','interpreter','latex','fontsize',17)
67
68 %% Root locus for IFF:
69 figure; rlocus(sys(1,Np)*Integrator_TF, linspace(1,600000,30)) ; %
        ,linspace(1,2000000,200000)
70 xlim([-50,3]); ylim([460,478])
71 grid on

```

## C.4 Model including transmissibility

```

1 % Single Fibre FE SS model, including suspension motion
2 %-----
3 close all
4 clear all
5
6 % Parameters
7 L = 0.7; % Effective pendulum fibre length [m]
8 Lp = 0.02; % Collocated pair position
9
10 % Number of lumped masses
11 N = 35; % (the more, the better, but exploding complexity)
12 Np = round(Lp*N/L); % location of piezo
13
14 kp = 1.857*10^6; % Piezo stiffness [N/m]
15 Mtm = 1.456; % kg
16 T = Mtm*9.81; % Tension N
17 CS = pi*(0.000215^2); % Fibre cross section area [m^2]
18 rho = 9280*CS; % mass/unit length [kg/m]
19 VMl = 1/(2*L)*sqrt(T/rho)
20 m = rho*L/N; % Lumped mass
21 k = N*T/L; % Lumped stiffness
22 w0 = sqrt(k/m);
23
24 % FE SS (lumped masses)
25 R = eye(N); %R(1,1) =1; R(round(N/2),round(N/2)) =1 ; % External
        force @ middle
26 K = diag(repmat(2,N,1)); % Stiffness matrix
27 for i = 1:N
28     if(i>1)
29         K(i,i-1) = -1;
30     end
31     if(i<N)
32         K(i,i+1) = -1;
33     end
34 end
35 K = k*K; K(Np,Np) = 2*k + kp ; K(N,N) = k;
36

```

```

37 M = m*eye(N) ;
38 M(N,N) = Mtm;
39
40 A = [zeros(N) -M\K; eye(N) zeros(N) ] ;
41 B = [M\R; zeros(N) ] ; B = [B zeros(2*N,1) ] ; B(1,N+1) =k/m;
42 C = zeros(3,2*N) ; C(1,N+Np)=-kp;C(2,2*N-1)=k;C(2,2*N)=-k; C(3,end
    ) = 1;
43 D = zeros(3,N+1); D(1,Np) = 1;
44
45 sys = ss(A,B,C,D); % state X = [ydot ; y]
46
47 % Open Loop TF SEN/ACT
48 load('opts.mat')
49 opts.PhaseWrapping = 'on';
50 figure; bodeplot(sys(1,Np),'r',opts)
51
52 %% Apply IFF control
53 FB_gain = 1000000;
54
55 Integrator_TF = tf([1],[1 0]);
56 IFF_compensator = FB_gain*zpk(Integrator_TF);
57
58 CL = feedback(sys,IFF_compensator,Np,1);
59
60 % Closed Loop TF SEN/ACT
61 hold on; bodeplot(CL(1,Np),'k',opts) ;
62 legend('OL','CL','interpreter','latex','fontsize',15);
63 title('')
64 ylabel('Phase','interpreter','latex','fontsize',17)
65 ylabel('Magnitude','interpreter','latex','fontsize',17)
66 xlabel('Frequency','interpreter','latex','fontsize',17)
67
68 a = sys*IFF_compensator;
69 figure; bodeplot(a(1,Np),'k',opts) ;
70 legend('OL','CL','interpreter','latex','fontsize',15);
71 title('')
72 ylabel('Phase','interpreter','latex','fontsize',17)
73 ylabel('Magnitude','interpreter','latex','fontsize',17)
74 xlabel('Frequency','interpreter','latex','fontsize',17)
75
76 figure; bodeplot(db2mag(69.3)*sys(end,end),'r',opts)
77 hold on; bodeplot(CL(end,end),'k',opts)
78 ylabel('Magnitude','interpreter','latex','fontsize',17)
79 ylabel('Phase','interpreter','latex','fontsize',17)
80 xlabel('Frequency','interpreter','latex','fontsize',17)

```